

# Maximising the scientific outcome of planetary missions with ESA's Spacecraft Plasma Interaction Software

## Final report

*Co-sponsored research*

*Open Discovery Ideas Channel*

*M.K.G. Holmberg (1), C.M. Jackman (1), M.G.G.T. Tylor (2), D. van Winden (3), O. Witasse (2), J.-E. Wahlund (4,5), S. Barabash (6), H. Adamski (7), C. Imhof (8), B. Michotte de Welle (9), H.L.F. Huybrighs (1), N. Altobelli (10), F. Cipriani (2), G. Déprez (2), F. Johansson (2)*

*Affiliations: (1) School of Cosmic Physics, DIAS Dunsink Observatory, Dublin Institute for Advanced Studies, Dublin 15, Ireland (2) ESTEC, European Space Agency, Noordwijk,*

Publishing Date: May 19, 2025

Contract Number: 4000137683/22/NL/GLC/my

Implemented as ESA Partnership Agreement

### **ESA Discovery & Preparation**

*From breakthrough ideas to mission feasibility. Discovery & Preparation is laying the groundwork for the future of space in Europe*

Learn more on [www.esa.int/discovery](https://www.esa.int/discovery)

Deliverables published on <https://nebula.esa.int>

*The Netherlands, (3) Netherlands Institute for Radio Astronomy (ASTRON), Dwingeloo, the Netherlands (4) Swedish Institute of Space Physics, Uppsala, Sweden (5) Department of Physics and Astronomy, Uppsala University, Uppsala, Sweden (6) Swedish Institute of Space Physics, Kiruna, Sweden (7) Department of Physics & Astronomy, UCLA, Los Angeles, USA (8) Airbus Defence and Space GmbH, Immenstaad, Germany (9) LPP, CNRS, Ecole polytechnique, Sorbonne Universite, Institut Polytechnique de Paris, Palaiseau, France (10) ESAC, European Space Agency, Madrid, Spain*

**Activity summary:**

In-situ particle and field measurements are vital for planetary exploration, yet they are difficult to validate due to limited overlapping data. This project explores novel uses of the ESA funded Spacecraft Plasma Interaction Software (SPIS) to analyse and validate such measurements, focusing on early data from the Jupiter Icy Moons Explorer (Juice) mission. This report includes a SPIS simulation guide, an example simulation of the interaction between Juice and the solar wind, and a guide on how to use SPIS to simulate actual particle analyser perturbations caused by spacecraft - environment interactions.



Chapter 1. Introduction to spacecraft plasma interaction	4
1.1 Background	4
1.2 Related publications	5
Chapter 2. Introduction to SPIS simulations	6
2.1 The Spacecraft Plasma Interaction Software (SPIS)	6
2.2 Download and install	6
2.3 Simulation set-up	8
2.4 Building the spacecraft 3D model	8
2.5 The computational mesh	15
2.6 Starting the SPIS simulation	17
2.7 The material library	20
2.8 The circuitry	22
2.9 The environment	24
Chapter 3. Spacecraft - environment interaction	30
3.1 The Juice mission	30
3.2 The spacecraft model	31
3.3 The solar wind at 1 AU	33
3.4 The simulation results: Interaction in the solar wind	35
3.5 Discussion	40
Chapter 4. In-situ particle measurements perturbations	42
4.1 The JDC instrument	42
4.2 The magnetosheath of Earth	47
4.3 The effect of spacecraft charging	48
4.4 Simulating the particle detector	49
4.5 Setting up a simulation with particle tracking	51
4.6 Processing of the simulation output	54
4.7 Simulation results	57
4.8 Discussion	62
Chapter 5. Summary of conclusions	64

References	65
Appendix	69
Appendix A	69
Appendix B	72

# **Chapter 1. Introduction to spacecraft plasma interaction**

## **1.1 Background**

In-situ particle and field measurements are a fundamental part of planetary exploration. However, due to the nature of such missions, the data can rarely be validated by comparisons with overlapping data sets from other instruments. Instead, computer simulations provide an important way to both analyse and validate in-situ measurements.

The ESA funded Spacecraft Plasma Interaction Software (SPIS) is commonly used to assess the risk of electrostatic discharges on ESA missions. For this research project we propose novel applications of SPIS: to use SPIS as a tool to better understand the effects of perturbations caused by spacecraft - environment interactions and improve calibration and data analysis routines. We will focus the study on the first measurements from the Jupiter Icy Moons Explorer (Juice) mission. However, the methods presented in this report can be adapted to any planetary mission with similar instrumentation. This research project will include: developing and applying models of the solar wind at 1 AU and the magnetosheath of Earth as inputs for SPIS simulations of the interaction between Juice and its surrounding environment; and using the simulation results to study perturbations in the Juice measurements. The project will be an important step in preparing Juice to fulfil its scientific objectives, in particular to accurately characterise the plasma and field environments of Jupiter's magnetosphere and moons. The new analysis method developed within this project could significantly contribute to improvements of analyses of space plasma and field data, not only for the JUICE mission but for any future planetary missions carrying the relevant instrumentation.

The work of analysing spacecraft measurements is a time consuming and complex task that includes extensive knowledge of everything from the physics governing the studied system to detailed knowledge of the spacecraft and the instrument. In addition, instrument teams are almost always in need of more funding due to the tough schedules and budgets of most space missions. The funding for developing the first analysis codes typically covers an adapted version of the analysis codes from the heritage of the instrument. This provides an approximative data product that will be continuously updated, often long after the beginning of the mission. Perturbations in the measurements originating from other instruments, the spacecraft itself, and its interaction with the surrounding environment are phenomena that are typically not well understood and that are studied and corrected for over the whole extent of the mission (see for example Holmberg et al. 2017, Johansson et al. 2020, and Holmberg et

al. 2021). Occasionally, the data products are still updated decades after the end of the mission (see for example Bagenal et al. 2017 and Futaana et al. 2018). Improved analysis techniques and computing capabilities are two explanations for improvements of data analysis codes implemented decades after the first measurements are performed. But the main reasons are the lack of standardised analysis methods, that easily can be adapted to different missions, and reliable validation methods. Within this research project we will address these specific problems.

Given the complexity of running SPIS simulations, this report will include a comprehensive guide on their execution. The guide is presented in Chapter 2.

## **1.2 Related publications**

More details about the work presented in Chapter 3 can be found in the article “Surface charging of the Jupiter Icy Moons Explorer (JUICE) spacecraft in the solar wind at 1 AU” by Holmberg et al., published in the Journal of Geophysical Research: Space Physics in 2024.

Part of this study was carried out as a master thesis project, with the corresponding results presented in Chapter 4. More details about the work can be found in the master thesis “Juice/JDC ion measurement perturbations caused by spacecraft charging in the solar wind and Earth’s magnetosheath” by van Winden, published in 2024.

## Chapter 2. Introduction to SPIS simulations

### 2.1 The Spacecraft Plasma Interaction Software (SPIS)

SPIS is a software used to model the interaction between an object, typically a spacecraft, and its surrounding space environment. The interaction is primarily driven by absorption or emission of charged particles. However, simulating the dynamics and emission or absorption of each particle would require immense computational resources. To address this, SPIS employs the particle-in-cell (PIC) method, which provides an efficient approximation. Within PIC individual particles are tracked in continuous phase space, while the movements of the distribution, e.g., densities and currents, are computed simultaneously on Eulerian mesh points. A more detailed description of SPIS can be found in Sarrailh et al. (2015).

### 2.2 Download and install

The first step in running SPIS simulations is to register as a member of the Spacecraft Plasma Interactions Network in Europe (SPINE), the official community for all SPIS users. The registration is made on the SPINE registration page: <https://www.spis.org/register/>. Click the button labeled “SPINE Community login form” and on the following page, below the “Sign In” button, select the option to “Register”. Once the registration is approved, SPIS can be downloaded from <https://www.spis.org/get/software/spis/surface/latest/>. This link will open a page similar to the window shown in Figure 1, where the appropriate version of SPIS can be selected based on the operating system.

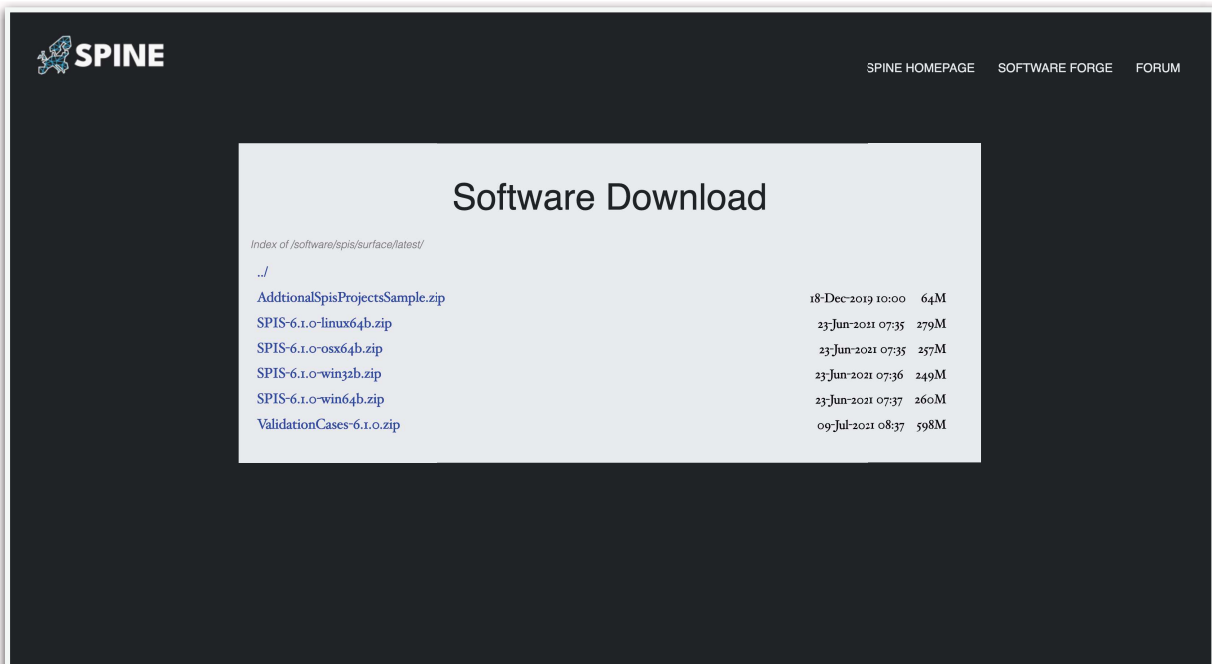


Figure 1 The page where SPIS can be downloaded

If choosing “Download” and entering a username and password, the site redirects to the page shown in Figure 2. By clicking “Download software”, it will redirect again to the page shown in Figure 3. From there, selecting “spis/”, “surface/”, “latest/” will lead to the same page as shown in Figure 1.



Figure 2 The webpage where SPIS can be downloaded, following authentication via a registered user account

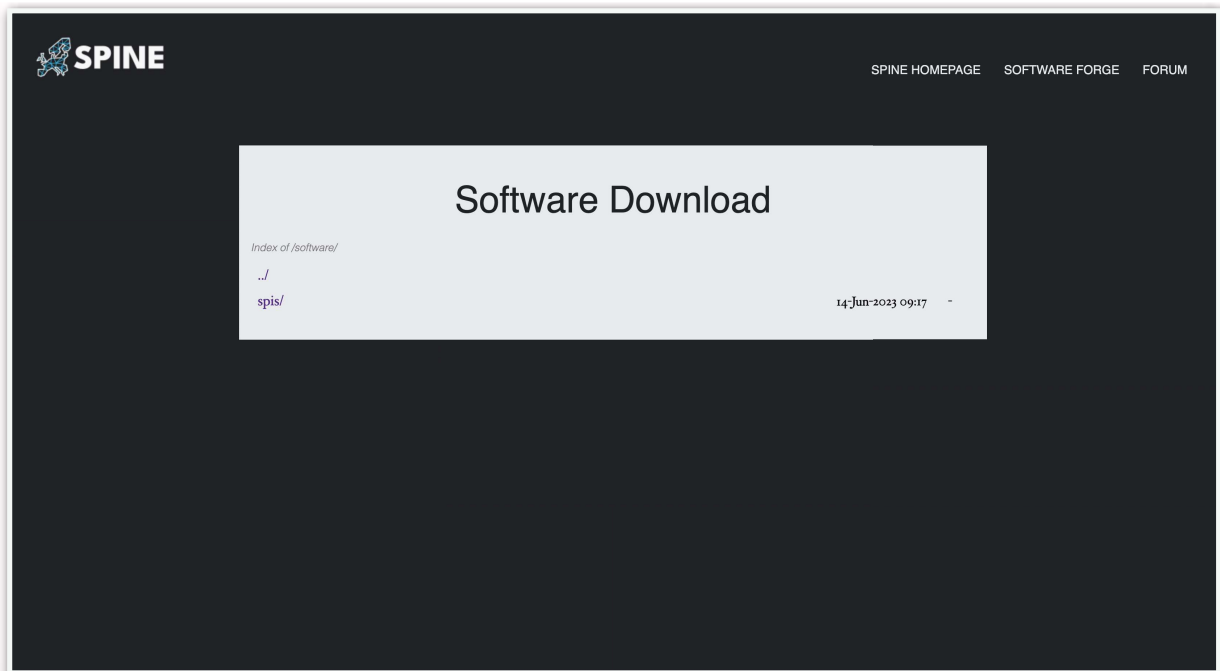


Figure 3 The page that appear after selecting “Download software”

The minimum hardware requirements to properly run SPIS are typically met by any computer manufactured after 2005. However, if SPIS is installed on an external server **make sure that the server has a graphic card with more than 128 Mb of video memory**. If this is missing from the server, the graphical user interface of SPIS cannot be launched, making it impossible to visually track the simulation steps. This will significantly hinder the simulation process, in particular when starting new projects.

After downloading and extracting SPIS, move the “SPIS-6.1.0” folder from the Download folder to the preferred application folder.

To use SPIS, a mesh generator called Gmsh is required. Although Gmsh is a separate software, it is included in the SPIS download package. However, the version of Gmsh included may not be compatible with certain systems, particularly those using a Mac with an M-series chip. In such cases, the macOS (ARM) version of Gmsh should be downloaded directly from the Gmsh website: **<https://gmsh.info>**.

## 2.3 Simulation set-up

In order to run SPIS simulations, the following steps are required:

- 1) Build a spacecraft geometry, covered by chapter 2.4
- 2) Generate a computational mesh, covered by chapter 2.5
- 3) Define the material library of the spacecraft, covered by chapter 2.7
- 4) Define the circuitry of the spacecraft, covered by chapter 2.8
- 5) Define the spacecraft environment, covered by chapter 2.9

All these steps will be covered in order, using a simplified spacecraft geometry, a basic cube, to simulate the surface charging of a spacecraft in the ionosphere of Jupiter's moon Ganymede at an altitude of 400 km, as an example.

## 2.4 Building the spacecraft 3D model

The first step in starting SPIS simulations is to build the spacecraft 3D model and computational mesh. As mentioned earlier, the mesh generator is Gmsh and is included in the SPIS download package. There are three different options for building the spacecraft geometry file, which contains all the information needed to create the computational mesh.

- A) The model can be built in SPIS using the “Edit geometry file” option.
- B) The Gmsh user interface can be used to build the geometry file.
- C) For very simple geometries, the easiest option is often to create a txt file and load it into Gmsh.

For our example we will use option C.

A common problem when running SPIS simulations is that the simulation mesh is not properly defined. It is therefore not recommended to build a complex spacecraft model before moving on to step 2 to 5 of setting up the simulation. Start instead with a very simple spacecraft model, preferably just a square or cylinder with the relevant proportions and run a first simulation using that geometry. This approach helps ensure that the rest of the simulation inputs are in order, before investing time in developing a more detailed spacecraft model. It supports the creation of a robust simulation set up by isolating potential issues related to the simulation mesh from those associated with the other input parameters, defined in step 3 to 5 of the simulation set up process.

When building a geometry in Gmsh start by defining the coordinates of the points that is the foundation of the spacecraft geometry. An example is shown in Figure 4.

We will begin with building a simple cube that represents the spacecraft, as shown in Figure 4. The parameters (l and b) that are defined in the beginning of the file gives the resolution of the mesh at the surface of the spacecraft, here called l, and at the outer boundary of the mesh, here called b.

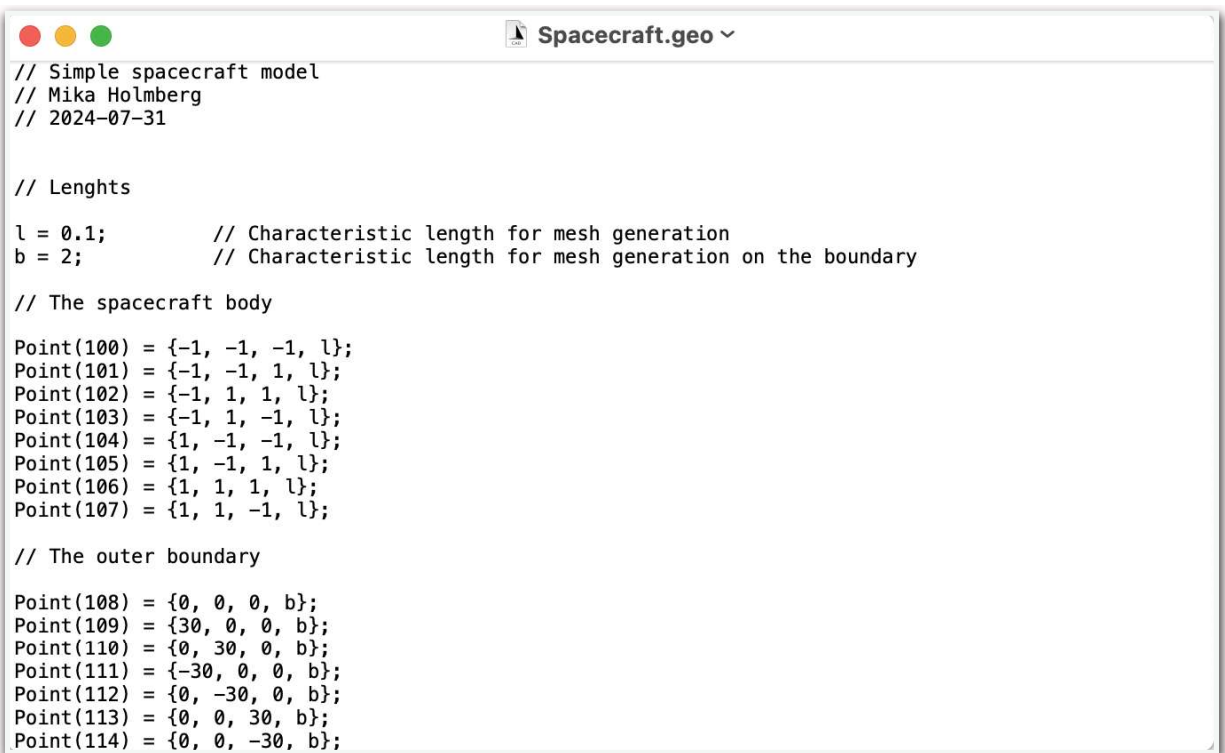


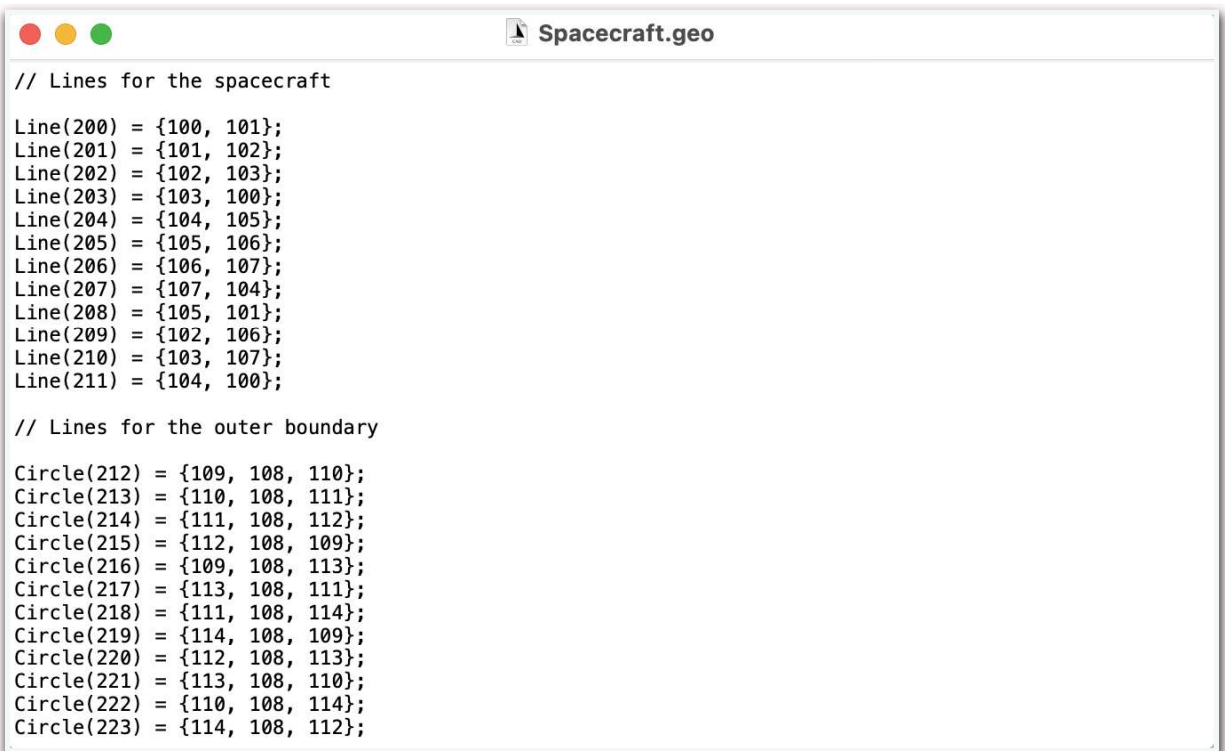
Figure 4 The beginning of the file that defines the spacecraft geometry



The Points give the coordinates for the points that define the geometry and also the mesh resolution at that specific point. For example,  $\text{Point}(100) = \{-1, -1, -1, l\}$ ; states that a point with ID number 100 should be located at  $x = -1$ ,  $y = -1$ ,  $z = -1$  and the mesh connected to this point should have mesh resolution  $l$ , which is given a length of 0.1 m in the lines above. Points 100 to 107 gives the corner points of the sphere. We also have to define the outer boundary of our computational volume, these are given by Points 108 to 114. Please be careful to use a large enough simulation geometry around the spacecraft, if the simulation volume is too small this will provide erroneous results. Large enough means that the computational volume should include any changes to the local environment caused by the presence of the spacecraft, this size will depend on the environment and spacecraft design. In this example we start with a volume with a diameter of 60 m for a cube shaped spacecraft with sides of 2 m.

After defining the points, define lines that connect the points, as shown in Figure 5. Here the three most commonly used options are;

- 1) Line, which is only used for straight lines,
- 2) Circle, which is only used for sections of circles and
- 3) Ellipse, which is used for sections of ellipses.



```
// Lines for the spacecraft
Line(200) = {100, 101};
Line(201) = {101, 102};
Line(202) = {102, 103};
Line(203) = {103, 100};
Line(204) = {104, 105};
Line(205) = {105, 106};
Line(206) = {106, 107};
Line(207) = {107, 104};
Line(208) = {105, 101};
Line(209) = {102, 106};
Line(210) = {103, 107};
Line(211) = {104, 100};

// Lines for the outer boundary
Circle(212) = {109, 108, 110};
Circle(213) = {110, 108, 111};
Circle(214) = {111, 108, 112};
Circle(215) = {112, 108, 109};
Circle(216) = {109, 108, 113};
Circle(217) = {113, 108, 111};
Circle(218) = {111, 108, 114};
Circle(219) = {114, 108, 109};
Circle(220) = {112, 108, 113};
Circle(221) = {113, 108, 110};
Circle(222) = {110, 108, 114};
Circle(223) = {114, 108, 112};
```

Figure 5 The lines that connects the points of the spacecraft geometry

For example,  $\text{Line}(200) = \{100, 101\}$ ; states that a line with ID number 200 should be located between the points with ID numbers 100 and 101. The direction of the line does not matter in this instance, so  $\text{Line}(200) = \{100, 101\}$ ; and  $\text{Line}(200) = \{101, 100\}$ ; will give the same result.

In Gmsh, the circle sections must be smaller than 180 degrees to ensure that the software correctly identifies the corresponding arc. The first point defines the start of the arc, the second defines the center of the circle and the third defines the end of the arc. After defining the lines, each surface must be defined, as shown in Figure 6. It is important to distinguish between surfaces with different materials, since the second step of the simulation set up is to define the materials and their properties. At that stage, each surface material must be defined individually. To define a surface, begin by listing the lines that form the boundary of that surface. For instance,  $\text{Line Loop}(300) = \{200, 201, 202, 203\}$ ; states that the lines with ID numbers 200, 201, 202, and 203 form a closed line loop with ID number 300. This closed line loop defines a plane surface so use  $\text{Plane Surface}(301) = \{300\}$ ; to state that the surface with ID 301 is the surface within the Line Loop with ID 300.

The image shows a screenshot of a text editor window titled "Spacecraft.geo". The window contains Gmsh script code for defining surfaces. The code is organized into two sections: "Defining the surfaces on the satellite" and "Defining the surfaces of the outer boundary". Each section contains multiple "Line Loop" and "Plane Surface" definitions. The "satellite" section defines surfaces 301 through 311, and the "outer boundary" section defines surfaces 312 through 323. Each "Line Loop" is followed by a "Plane Surface" definition that uses the loop's ID.

```
// Defining the surfaces on the satellite
Line Loop(300) = {200, 201, 202, 203};
Plane Surface(301) = {300};
Line Loop(302) = {204, 205, 206, 207};
Plane Surface(303) = {302};
Line Loop(304) = {204, 208, -200, -211};
Plane Surface(305) = {304};
Line Loop(306) = {202, 210, -206, -209};
Plane Surface(307) = {306};
Line Loop(308) = {205, -209, -201, -208};
Plane Surface(309) = {308};
Line Loop(310) = {211, -203, 210, 207};
Plane Surface(311) = {310};

// Defining the surfaces of the outer boundary
Line Loop(312) = {212, -221, -216};
Surface(313) = {312};
Line Loop(314) = {213, -217, 221};
Surface(315) = {314};
Line Loop(316) = {214, 220, 217};
Surface(317) = {316};
Line Loop(318) = {215, 216, -220};
Surface(319) = {318};
Line Loop(320) = {212, 222, 219};
Surface(321) = {320};
Line Loop(322) = {213, 218, -222};
Surface(323) = {322};
```

Figure 6 How to define the surfaces of the spacecraft model

The directions of the enclosed lines that make up a surface are crucial. For example, Line Loop 312 is made up of the line segments 212, 221 and 216, but the directions of the lines are not all the same. Line 212 is defined from Point 109 to 110, Line 221 is

defined from Point 113 to 110, and Line 216 is defined from Point 109 to 113. Hence, by reversing the direction of lines 221 and 216 a closed loop is formed with all segments oriented in the same direction. The order of the points will then be 109, 110, 113 and back to 109. Alternatively, the line loop can be defined in the opposite direction as {-212, 221, 216}, which would achieve the same result. Since it is easy to make mistakes at this step, it is imperative to double check whether the line loops are correctly defined before moving on. This can be done by opening the geometry file in Gmsh. Click on the Gmsh icon in the Application folder and choose “File” and “Open” and choose the geometry file. For the simple geometry that we are using here, this opens a window like the one in Figure 7. If the Gmsh version included in the downloaded SPIS package is being used, Gmsh can be found within the SPIS folder in “dependencies/thirdparty”.

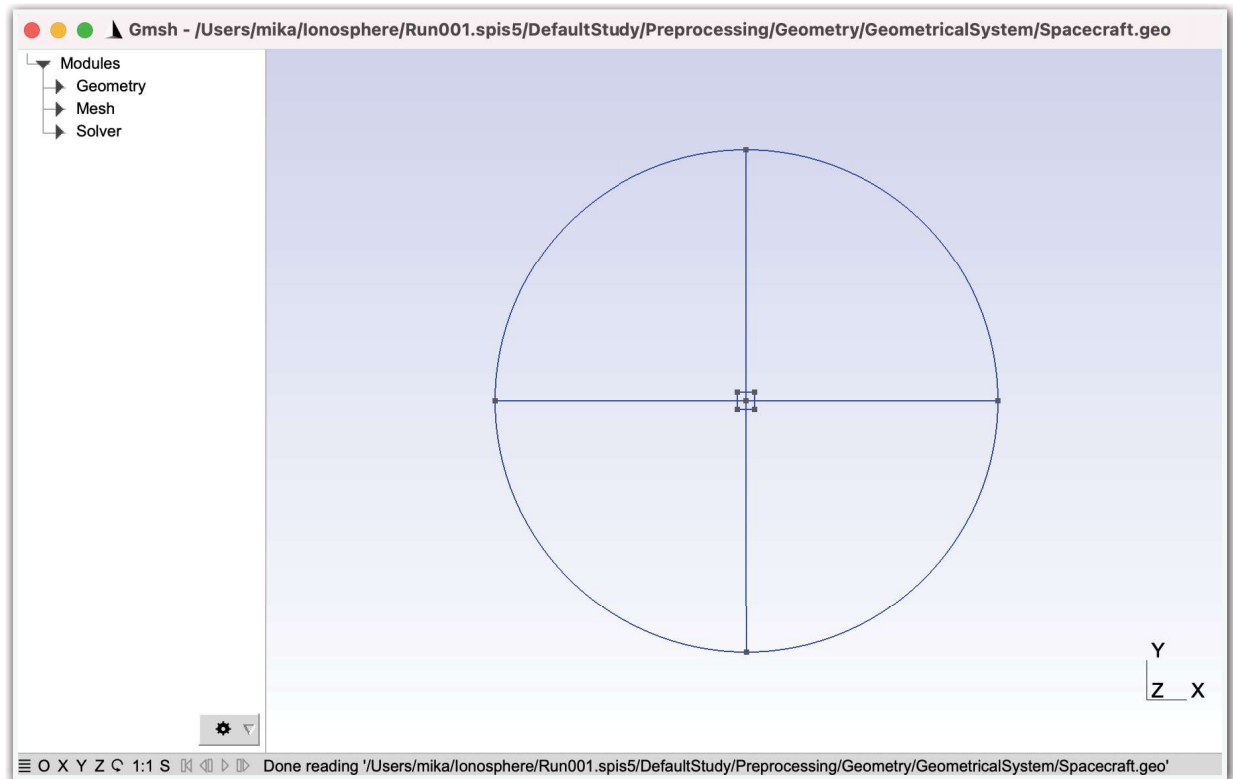


Figure 7 The spacecraft geo file opened in Gmsh

The blue circle shown in Figure 7 is the outer boundary of the computational volume and the small square represents the spacecraft. If one of the line loops has been defined incorrectly, the window would look like in Figure 8. Please note the red error message displayed at the bottom of the window.

The error message shows that something is defined incorrectly. Clicking on the red line reveals the full error message: **Curve loop 312 is wrong, Wrong definition of**

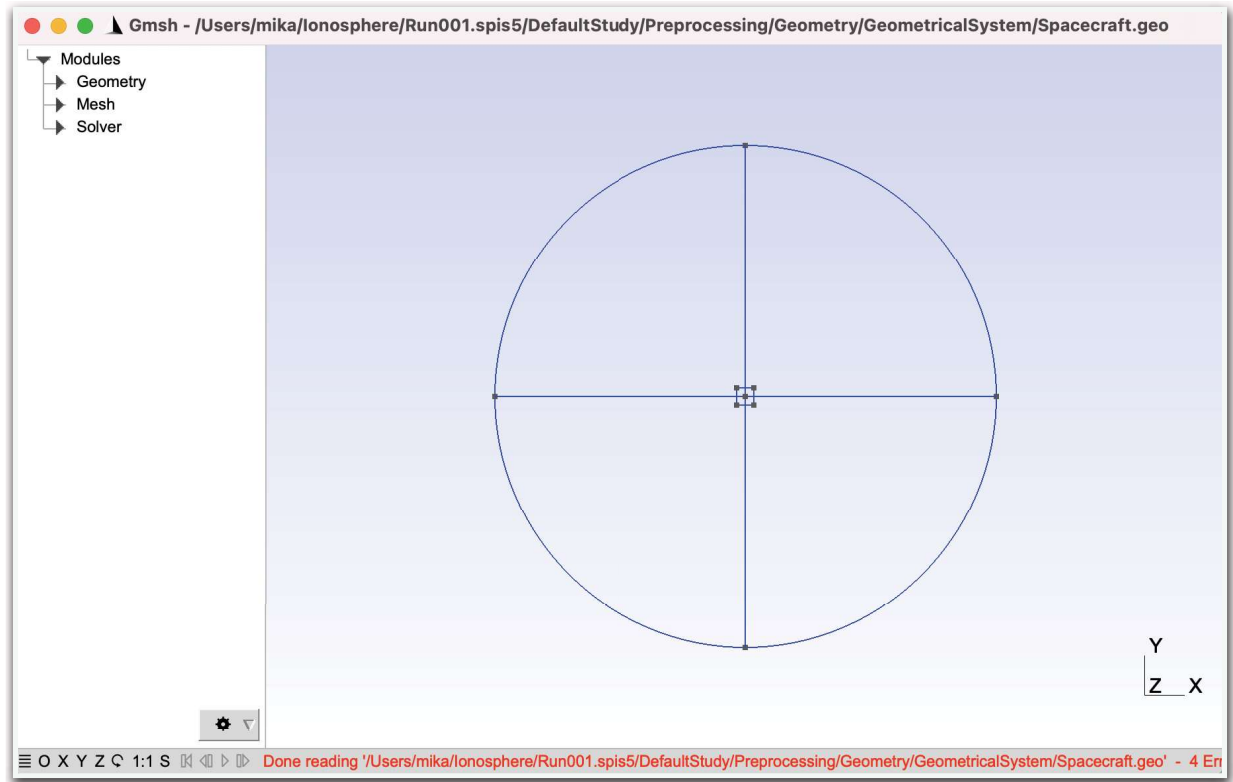


Figure 8 The red text shows the error message of Gmsh

surface 313: 1 borders instead of 3 or 4. Rotating the geometry and zooming in allows for visual inspection to ensure that all the points and lines are properly defined, as can be seen in Figure 9.

To verify that all the surfaces are correctly defined press “Tools”, “Options”, “Geometry” and mark “Surfaces”. This will include grey dashed lines crossing all the defined surfaces, as shown in Figure 10. Enabling the “Volumes” option reveals a yellow sphere at the center of the computational volume. Defining the computational volume begins with creating a Surface Loop, as shown in Figure 11. For example,  $\text{Surface Loop}(400) = \{301, 303, 305, 307, 309, 311\}$ ; states that a surfaces loop with ID number 400 contains all the plane surfaces of the sphere that represents the spacecraft. Surface Loop 401 contains all the surfaces of the outer boundary. To define the computational volume use  $\text{Volume}(500) = \{401, 400\}$ ; where the inner surface loop 400 is subtracted from the outer surface loop 401, resulting in a volume between the spacecraft model and the outer boundary, which is the computational volume. It is important to make sure that all volumes are closed volumes and that no surfaces are missing.

After defining all the points, lines, surfaces and volumes, these entities have to be grouped together into what in Gmsh is called physical surfaces and volumes. An example is shown in Figure 11. The Physical Volume should be the same

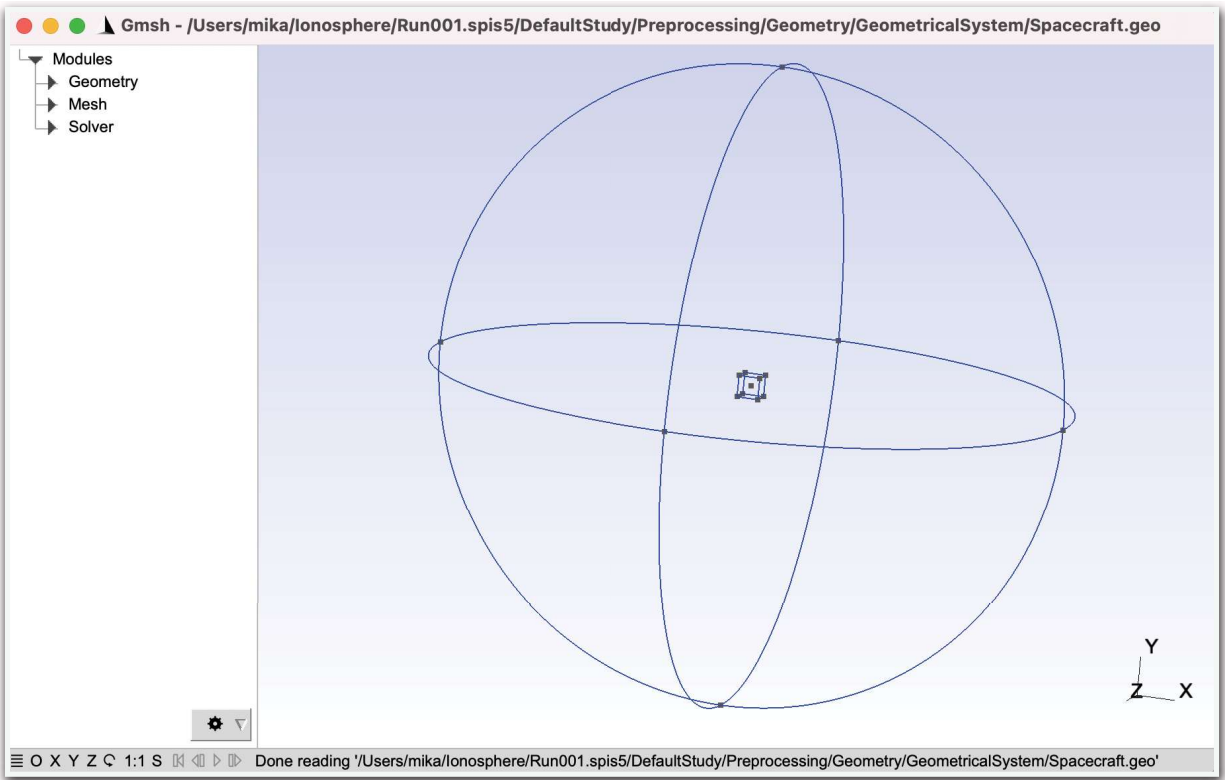


Figure 9 The geometry can be rotated and enlarged

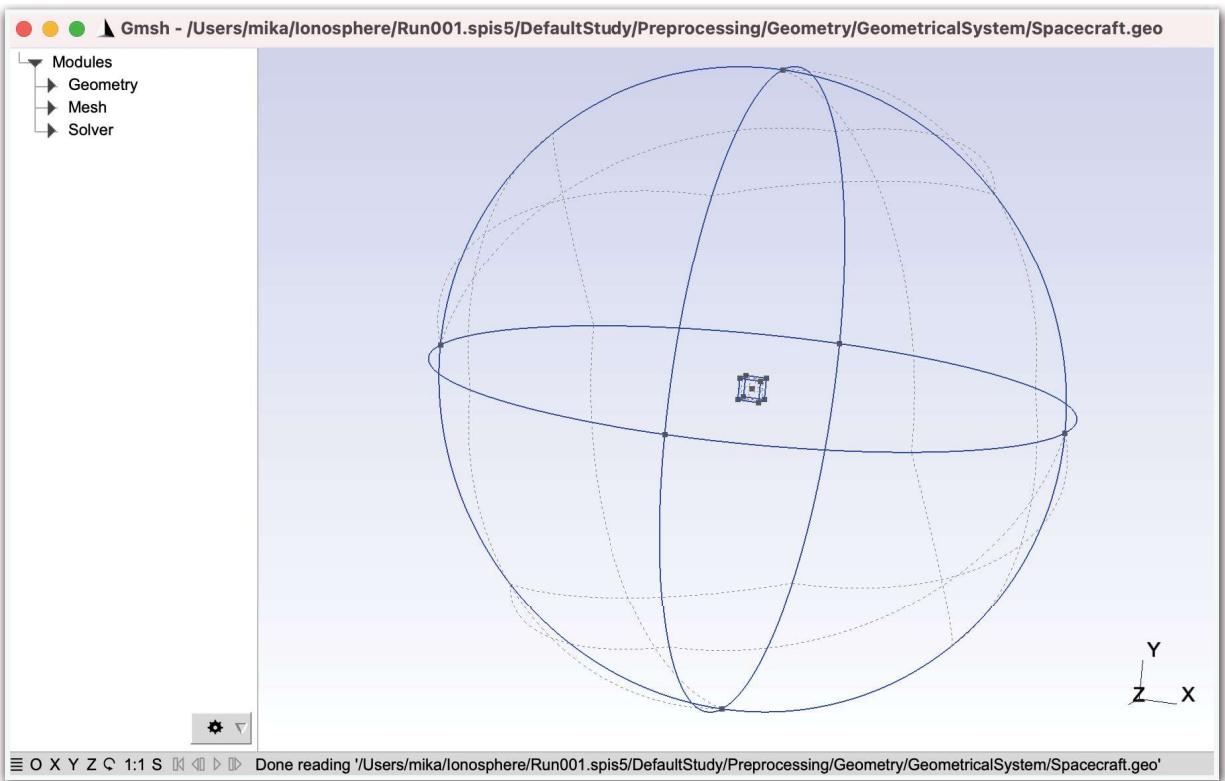


Figure 10 The surfaces are crossed by grey dashed lines

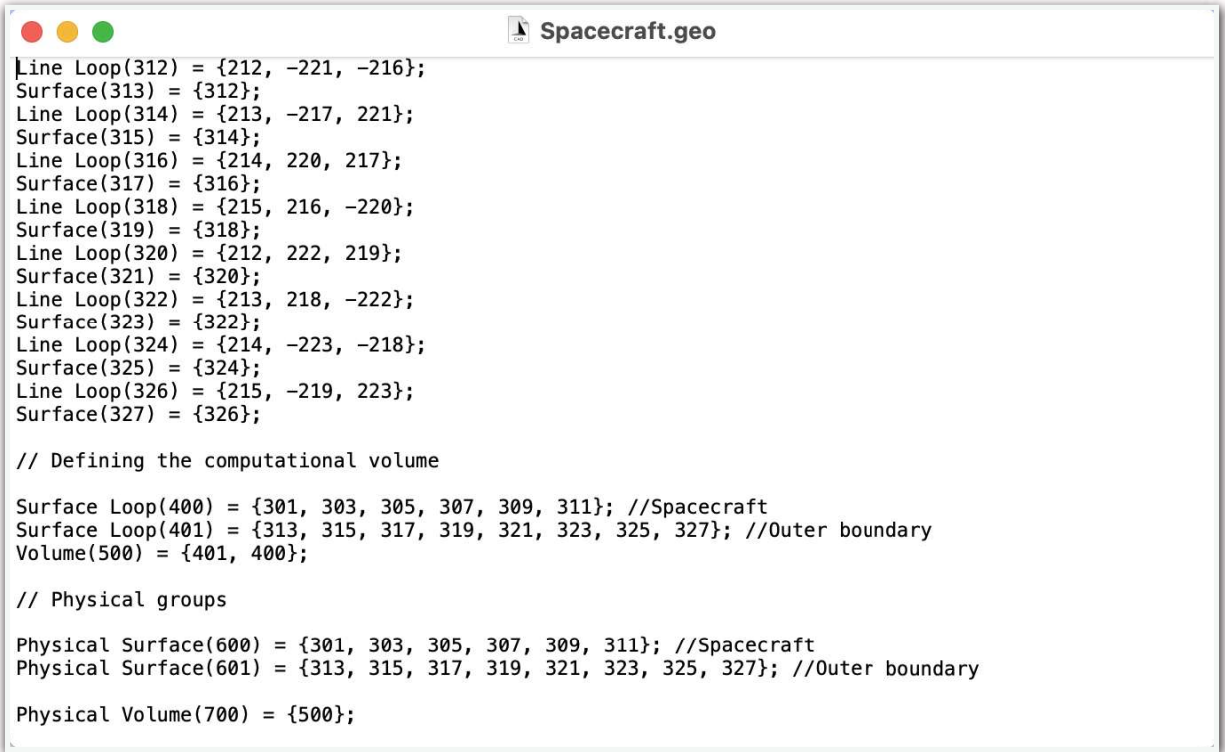


Figure 11 Example of how to define the volumes and the physical groups

computational volume as defined earlier.

## 2.5 The computational mesh

The next step is to build the mesh of the computational volume. This can be done in both Gmsh and SPIS. In Gmsh, use the menu on the left hand side of the window, choose “Mesh” and then “3D”. The mesh should then be visible in the computational volume, as shown in Figure 12.

Mesh generation includes an optimisation process that removes low-quality elements which could otherwise lead to computational issues. There are also methods to optimise the mesh even further, such as the “Optimize 3D” or “Optimize 3D (Netgen)”, these methods also reduce the number of mesh elements. Based on experience, the best outcome is usually from using the “Optimize 3D (Netgen)”. Mesh improvements can be monitored using the “Tools” and “Statistics” window. For example, when creating the mesh shown in Figure 12, the initial mesh contains 249,626 tetrahedral elements. After applying the “Optimize 3D (Netgen)” once, this number is reduced to 216,805.

A useful way to check that the volumes and the mesh is defined correctly is to look at the image of the 3D element faces, as shown in Figure 13. Open “Tools” and “Options”, choose “Mesh” and remove the markers from “2D element edges” and “3D element



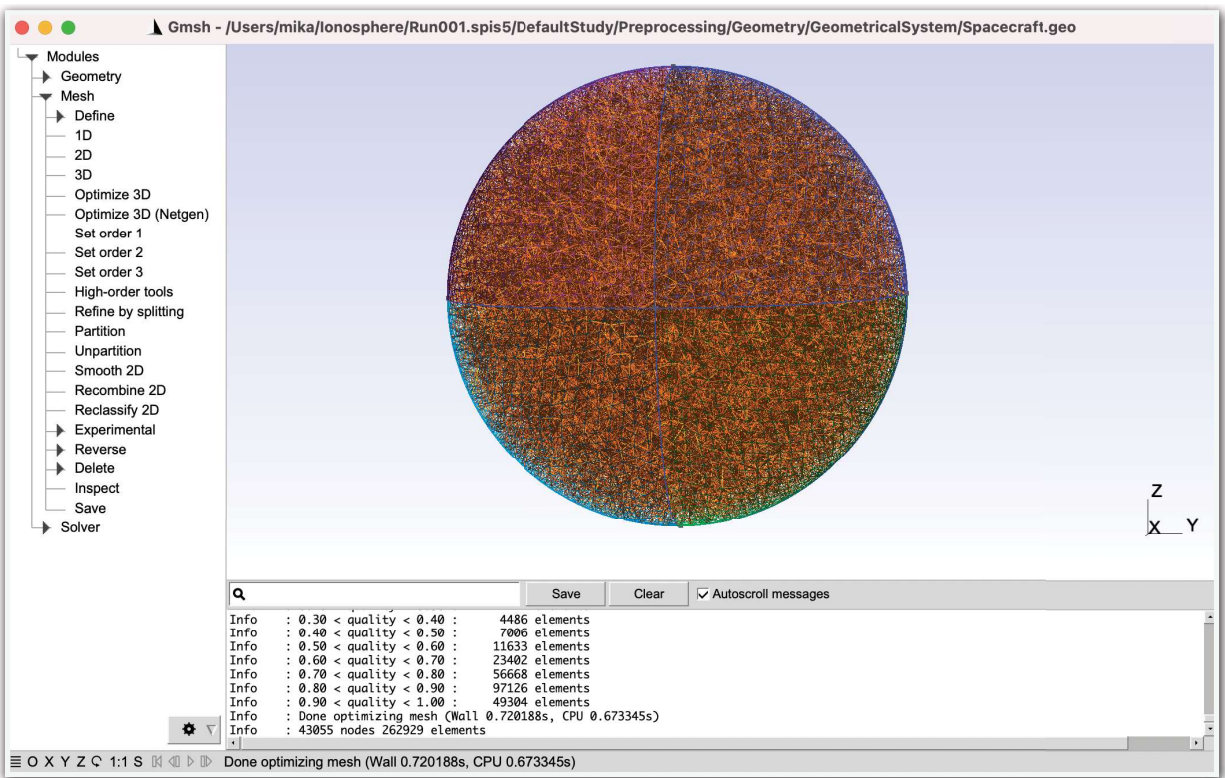


Figure 12 The mesh of the computational volume

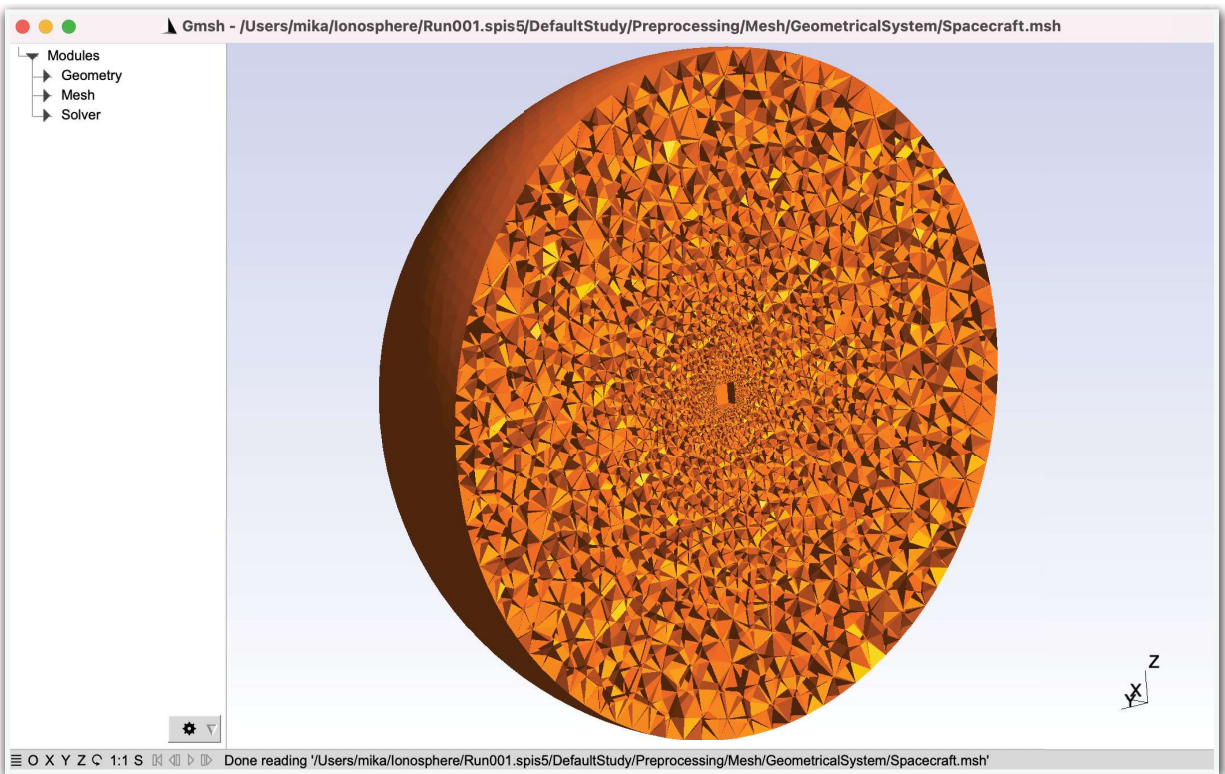


Figure 13 The cross-section of the computational volume

edges” and make “3D element faces” visible. Then open “Tools” and “Clipping”, choose “Mesh”. If using 1 for parameter A in Plane 0, the computational mesh will be cut in half, as shown in Figure 13. Move the object to see the cross-section of the mesh.

Figure 13 shows that no mesh elements are present inside the spacecraft, represented by the central square. If the spacecraft volume were not properly closed, mesh elements would also appear inside the spacecraft. Figure 13 also shows that the mesh elements are finer around the spacecraft, defined to be of the order of 0.1 m, and coarser at the outer boundary of the computational volume, where they are defined to be of the order of 2 m.

Once the mesh is finalised, it must be saved. Use “File”, “Export”, choose the file format “Mesh - Gmsh MSH (\*.msh) and save the file in the preferred folder and with the preferred name, for example Spacecraft.msh. Click “Save”, choose the “Version 2 ASCII” format and click “OK”. The computational mesh is now ready to be used in SPIS simulations.

## 2.6 Starting the SPIS simulation

To start SPIS, open a terminal window, go to the SPIS folder and type “sh Spis.sh” or, in Windows, “Spis.bat”. This should open a window like the one shown in Figure 14. To find the SPIS folder use the command “ls” to display the current directory and use the command “cd” to move to a different folder. For example, typing “ls” shows that

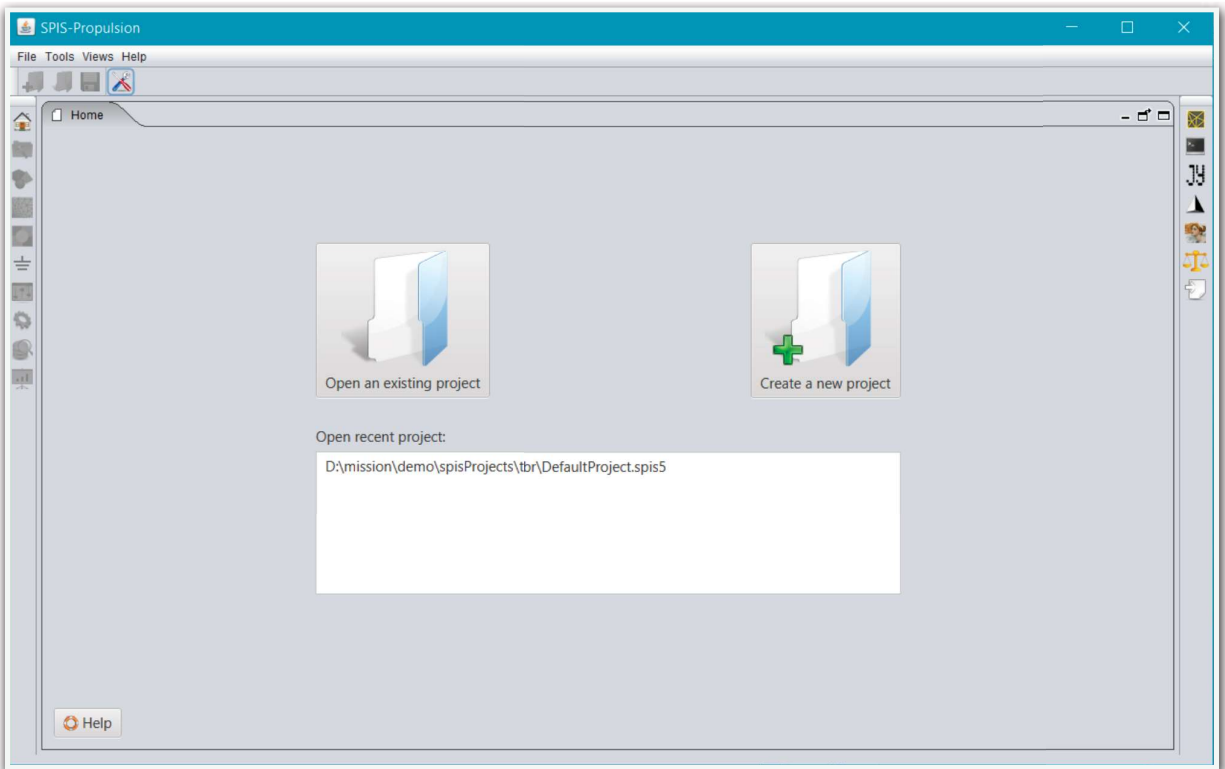
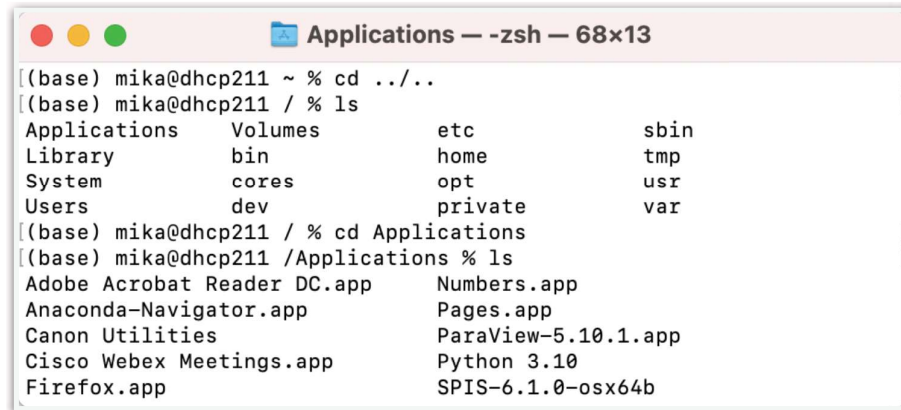


Figure 14 The start page of SPIS



the current location is the “mika” directory. The command “cd ../../” is then used to move two directories up to access the “Applications” folder and the SPIS folder named “SPIS-6.1.0-osx64b”. The example is shown in Figure 15.

A terminal window titled "Applications — -zsh — 68x13" showing a series of commands and their outputs. The user starts in the "~" directory, moves up two levels with "cd ../../", lists the contents of the root directory with "ls", and then moves into the "Applications" directory with "cd Applications". Finally, they list the contents of the "Applications" directory with "ls", which shows various application folders and files, including "SPIS-6.1.0-osx64b".

```
[(base) mika@dhcp211 ~ % cd ../../
[(base) mika@dhcp211 / % ls
Applications      Volumes          etc               sbin
Library           bin              home              tmp
System            cores            opt               usr
Users             dev              private           var
[(base) mika@dhcp211 / % cd Applications
[(base) mika@dhcp211 /Applications % ls
Adobe Acrobat Reader DC.app      Numbers.app
Anaconda-Navigator.app           Pages.app
Canon Utilities                  ParaView-5.10.1.app
Cisco Webex Meetings.app         Python 3.10
Firefox.app                      SPIS-6.1.0-osx64b
```

Figure 15 How to navigate to the SPIS folder

For Mac users, the first attempt to open SPIS typically results in an error message. This is due to the default security settings of Mac, which only allows apps from App Store or from known developers to be opened. To change these settings go to “Security & Privacy” setting in “System Preferences”. This should open a window like the one shown in Figure 16. Make sure that “App Store and identified developers” is selected. Next to the blocked app, choose “Allow Anyway” and try to open SPIS again. This process will likely have to be repeated multiple times before the SPIS start window, like the one shown in Figure 14, will be opened. The main features from the SPIS start window are “Open an existing project”, used to access previously started projects, and “Create a new project”. Select “Create a new project” to begin.

Clicking “Create a new project” opens the window shown in Figure 17, where a name for the new project must be specified. As multiple simulations with similar set-ups are likely to be executed, it is recommended to use a naming convention such as Run001. Including the 00 ensures that the projects are sorted in the correct order and not in, for example, the order Run1, Run100, Run2 etc. Select a “Project parent folder” that reflects the simulated environment or specific conditions, for example “Ionosphere”. Since a large number of simulations are typically conducted during the course of a project, it is advisable to create a Readme document to log all the input parameters for each simulation. This will make it much easier to know what separates the different simulation runs. It is not advisable to try to list this in the name of the project, since this will lead to excessively long names that still fail to capture all the input parameters in the name.

Choose the project name and parent folder, click “Create project and save” and you have now started your first SPIS project. Congratulations! The next window looks like

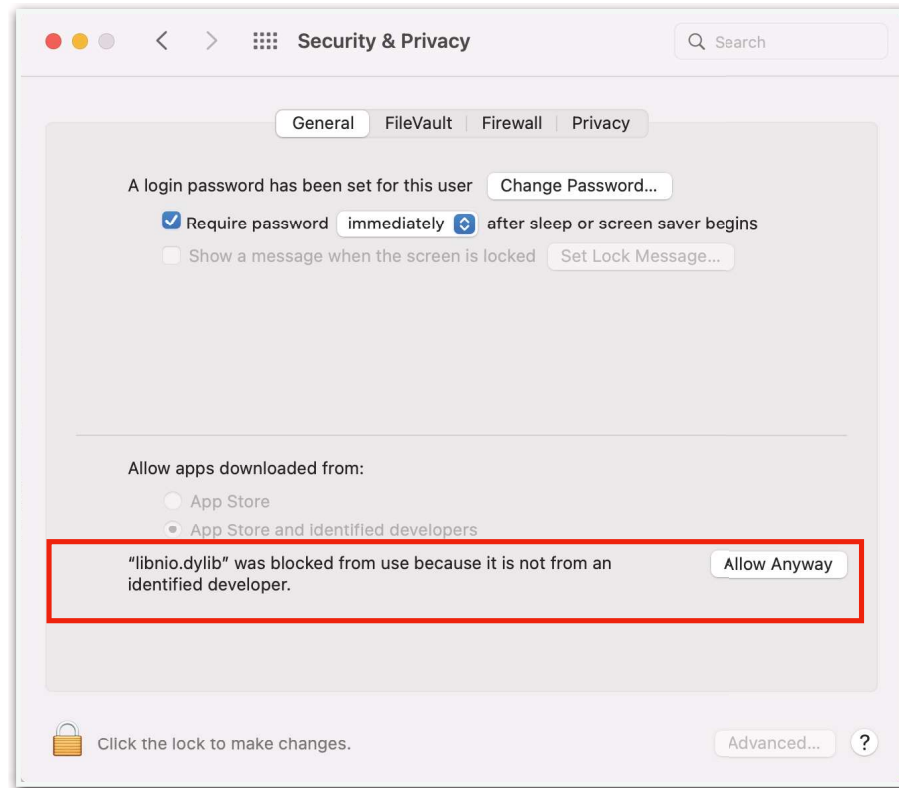


Figure 16 Example of files included in the SPIS download that might have to be manually approved

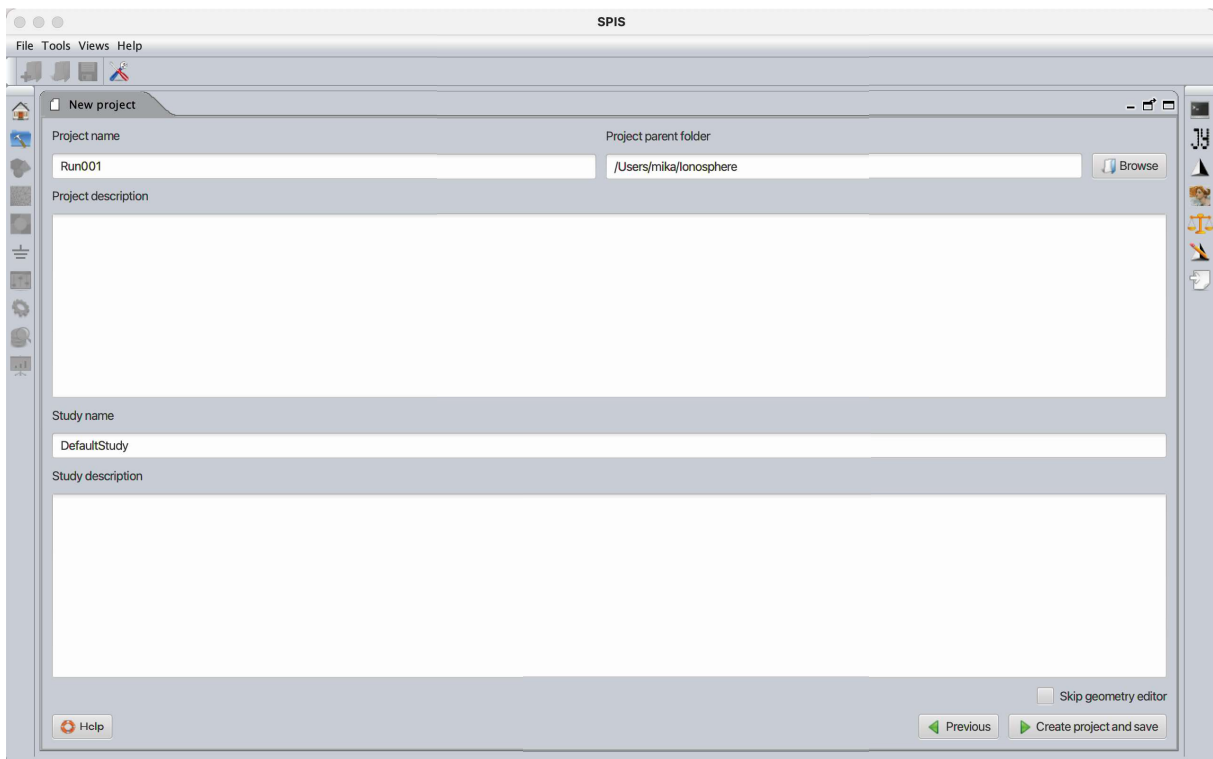


Figure 17 Name your project and place it in the correct folder

the one in Figure 18 and this is the point at which the spacecraft model construction begins.

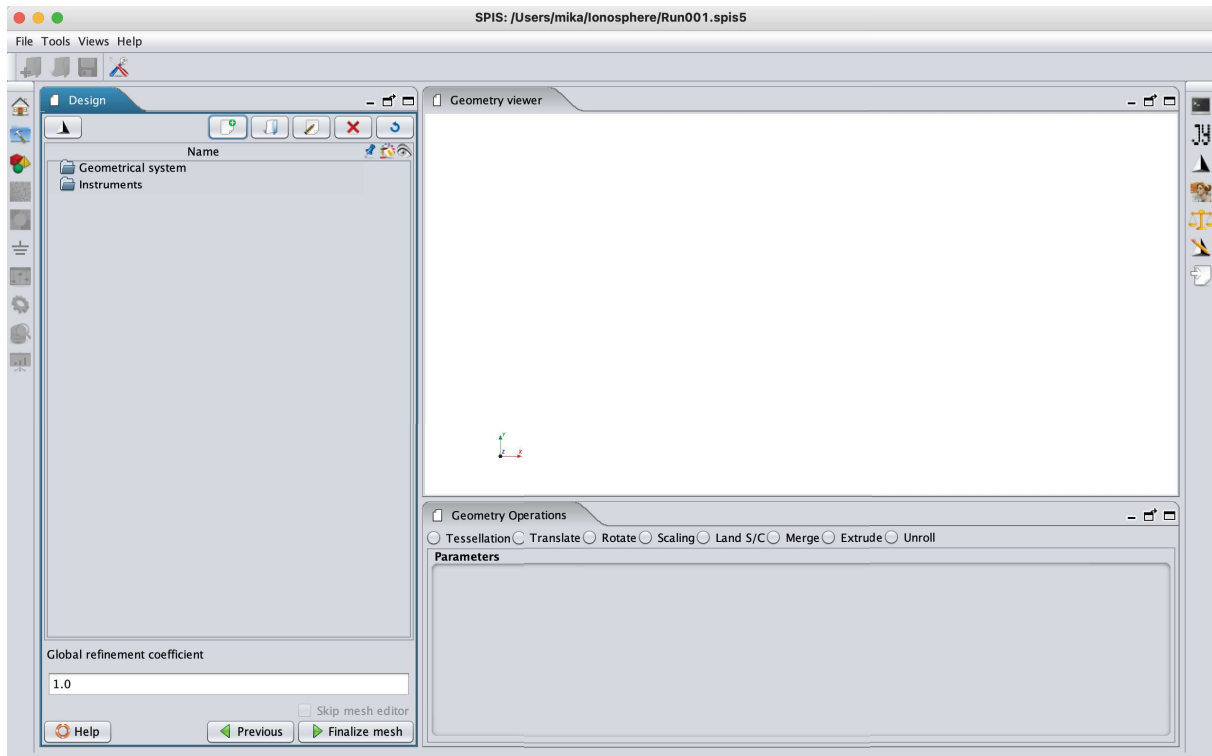


Figure 18 The SPIS spacecraft geometry window

## 2.7 The material library

The next step is to define the properties of the spacecraft materials using the group editor, as shown in Figure 19. In the left menu, all defined physical surfaces and volumes will appear. They are identified with the assigned ID numbers. The first physical surface is the spacecraft with ID number 600. Selecting this surface allows the “Group type” to be set, which should be “Spacecraft surface group”. This group type includes a range of properties, most of them can be left at their default values, but the most important one is the “S/C material”. SPIS already has a material library with many common spacecraft materials, for this example the “Kapton Black (2K) material properties” is selected, which is a common spacecraft surface material.

Select the surface material and click “OK”. The different material properties will then be added to this specific surface as shown in Figure 20. When “Kapton Black (2K) material properties” is selected and expanded, a list of associated properties appears, as shown in Figure 21. These properties can be modified if needed. The definition of

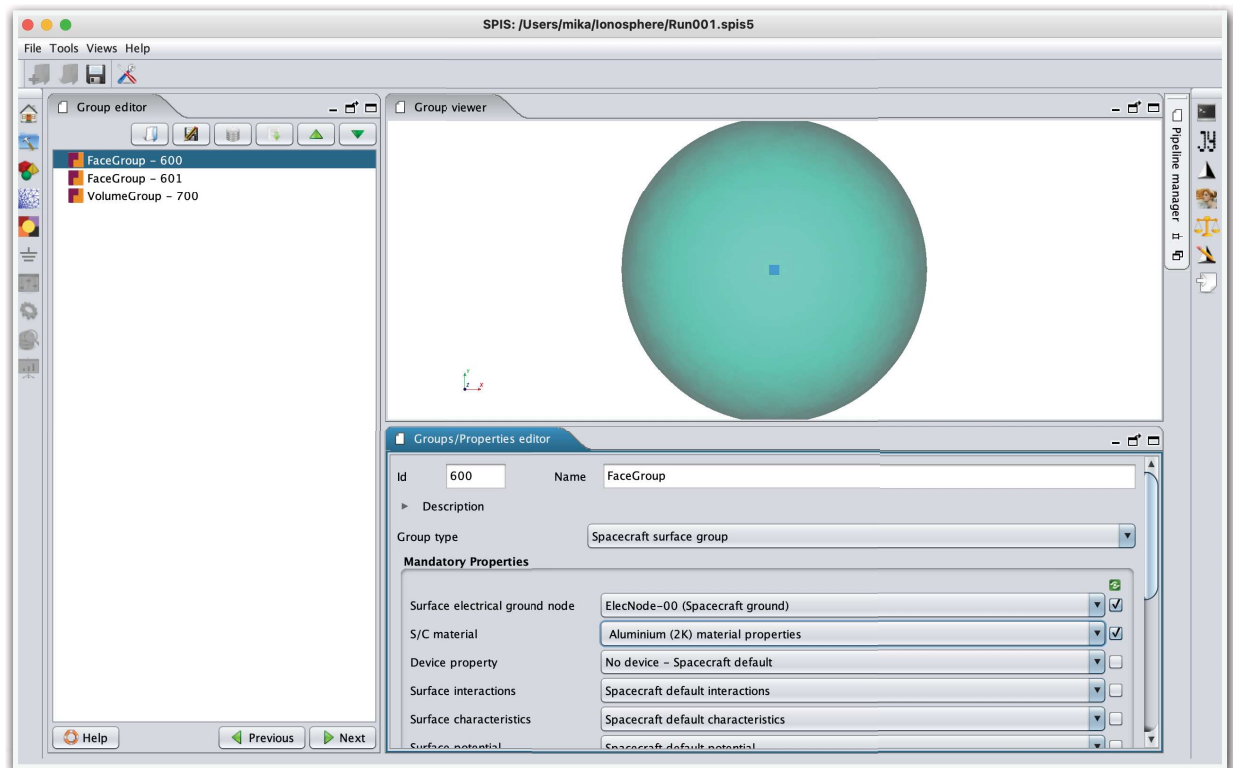


Figure 19 The group editor where the material properties are defined

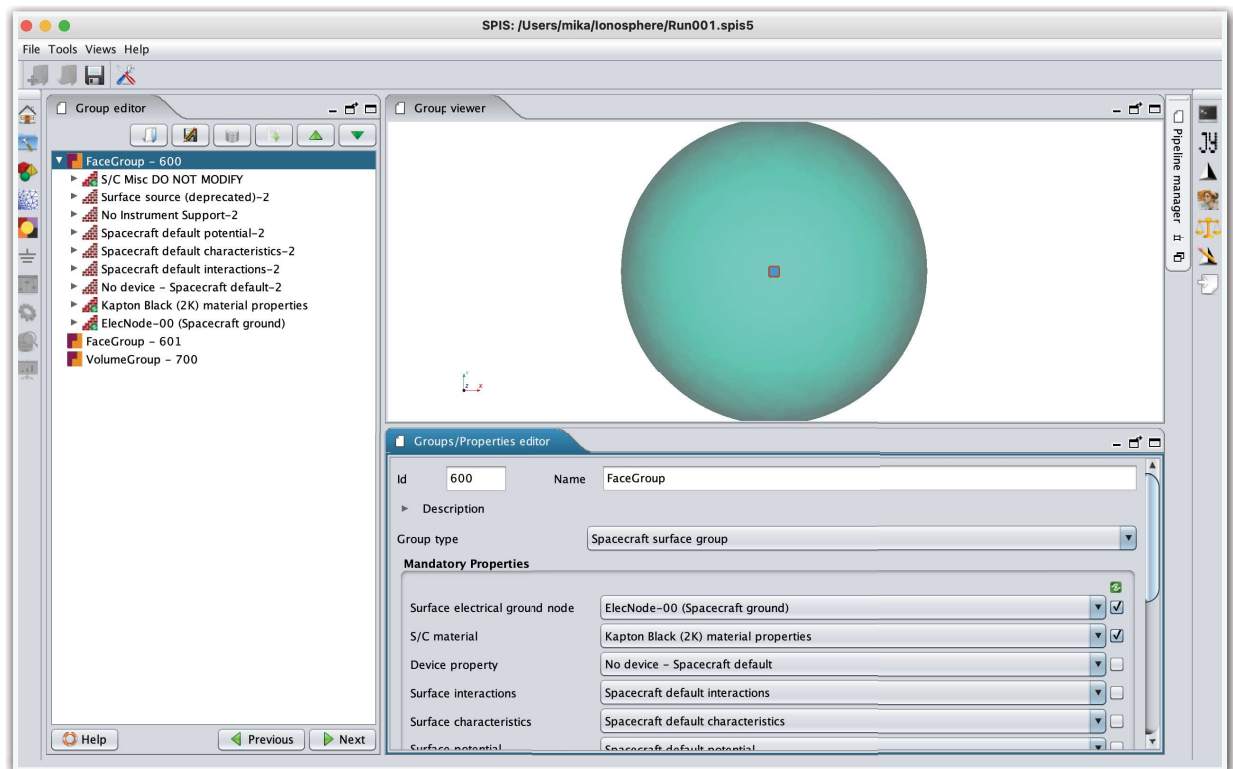


Figure 20 Choose the spacecraft surface material

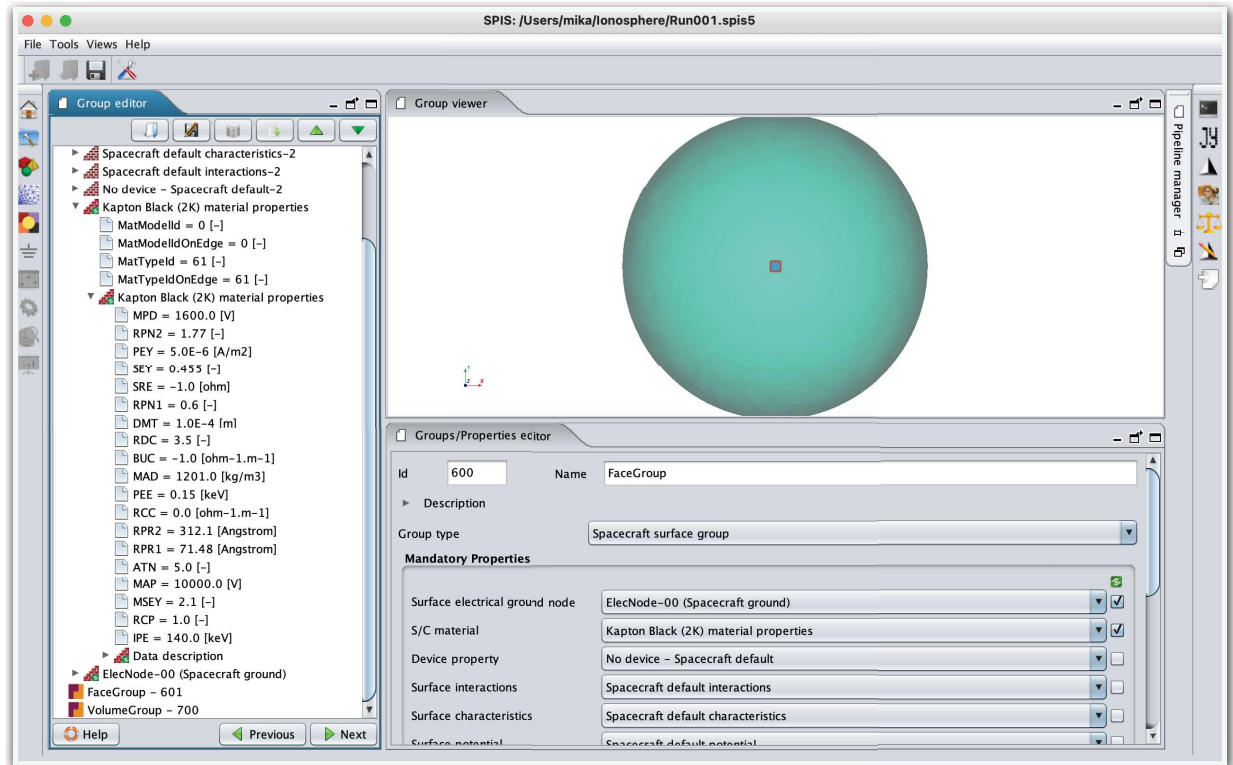


Figure 21 The material properties are listed in the left menu

the different properties are listed in Appendix B. For example, to explore how the spacecraft charging will change with a less conductive version of black kapton, the bulk conductivity parameter called BUC can be adjusted. For black kapton this value is set to -1, which means that it is simulated as a perfect conductor. To test an alternative conductivity value, click on the parameter “BUC” and change the value in the right window, as shown in Figure 22.

The next group is the external boundary with ID 601. Click on “FaceGroup - 601”, choose “External boundary group” and “OK”. Then Click on “VolumeGroup -700”, choose “Computational volume group” and “OK”. The group editor should then look like in Figure 23. Then click “Next”.

## 2.8 The circuitry

The next step is to define the electrical circuit. This is where to specify how the various parts of the spacecraft are electrically connected. The different parts can be connected using resistors (called R), capacitors (C), or voltage generators (V). An example would be

```
V 0 1 -10
R 0 2 1.e6
```

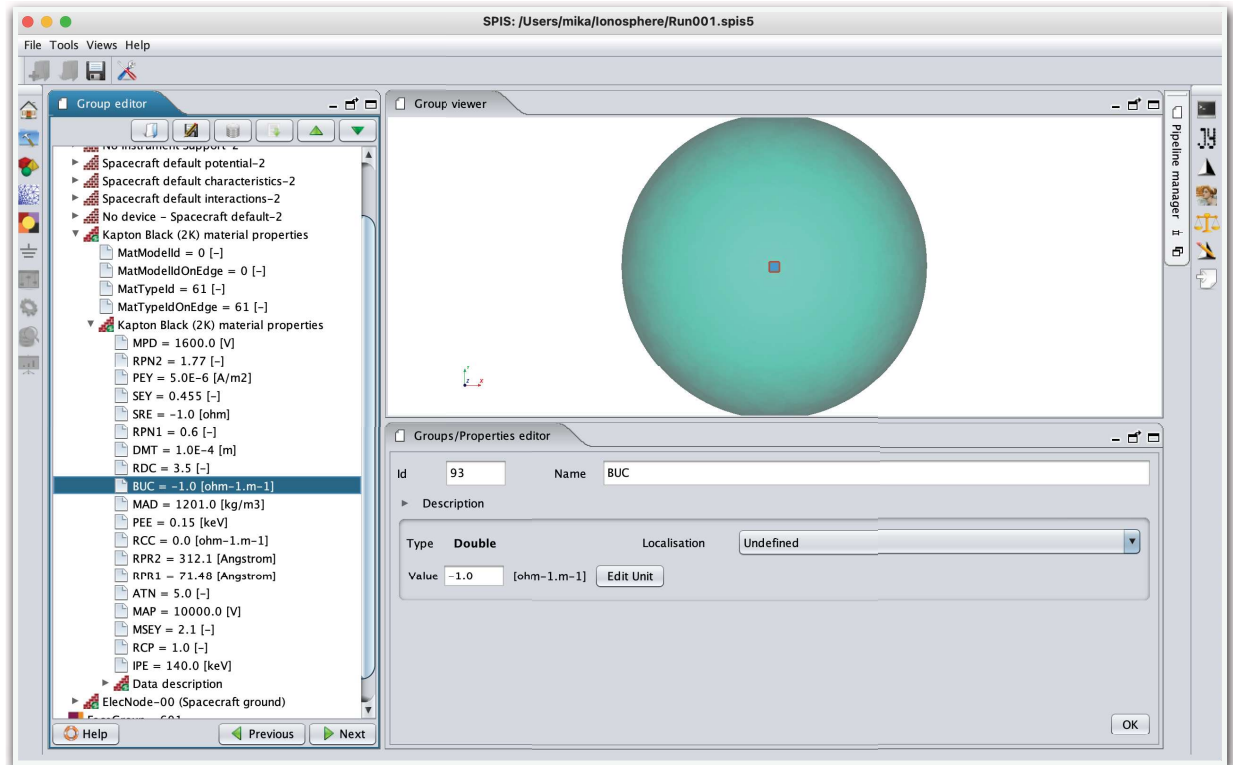


Figure 22 To change a material property

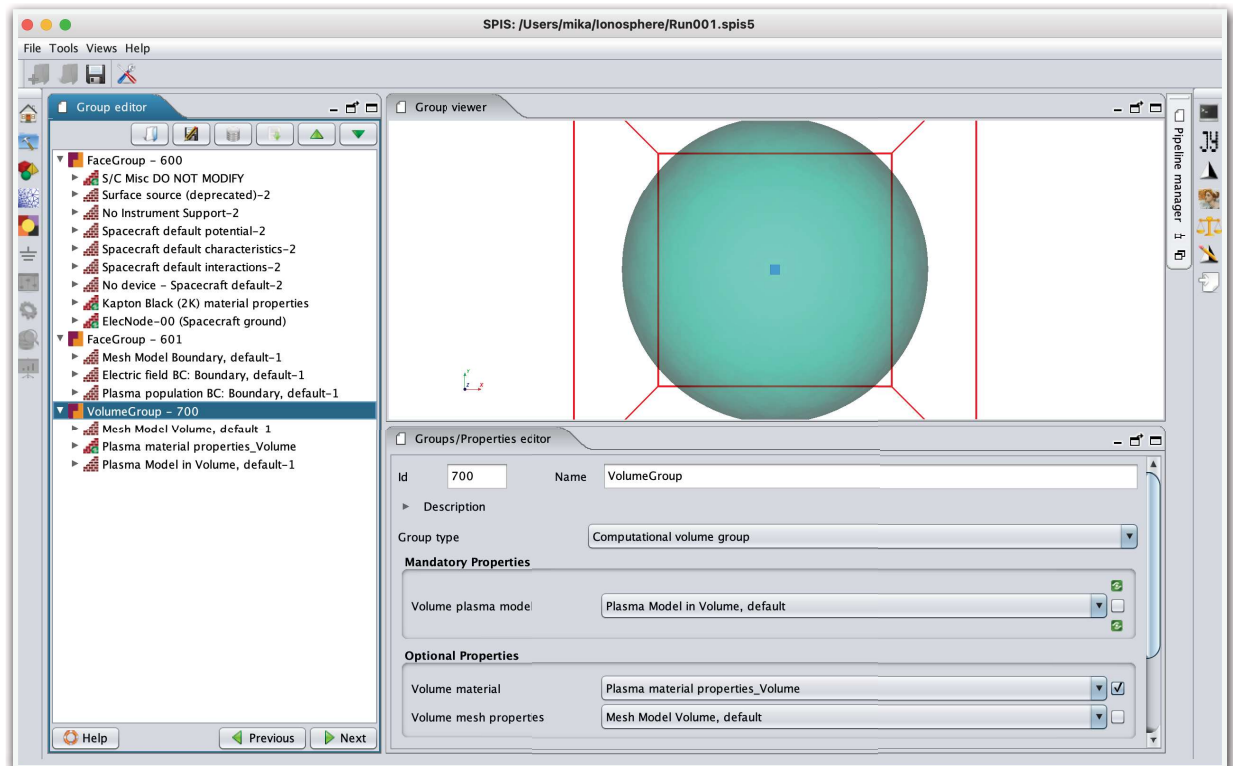


Figure 23 The group editor after all groups have been defined

which mean that a biased voltage of -10 V would be imposed between surface 0 and 1, and a resistor of 1.e6 Ohm is set between surface 0 and 2.

Since we only have one spacecraft surface we can leave this section blank, as shown in Figure 24, and just press “Next”.

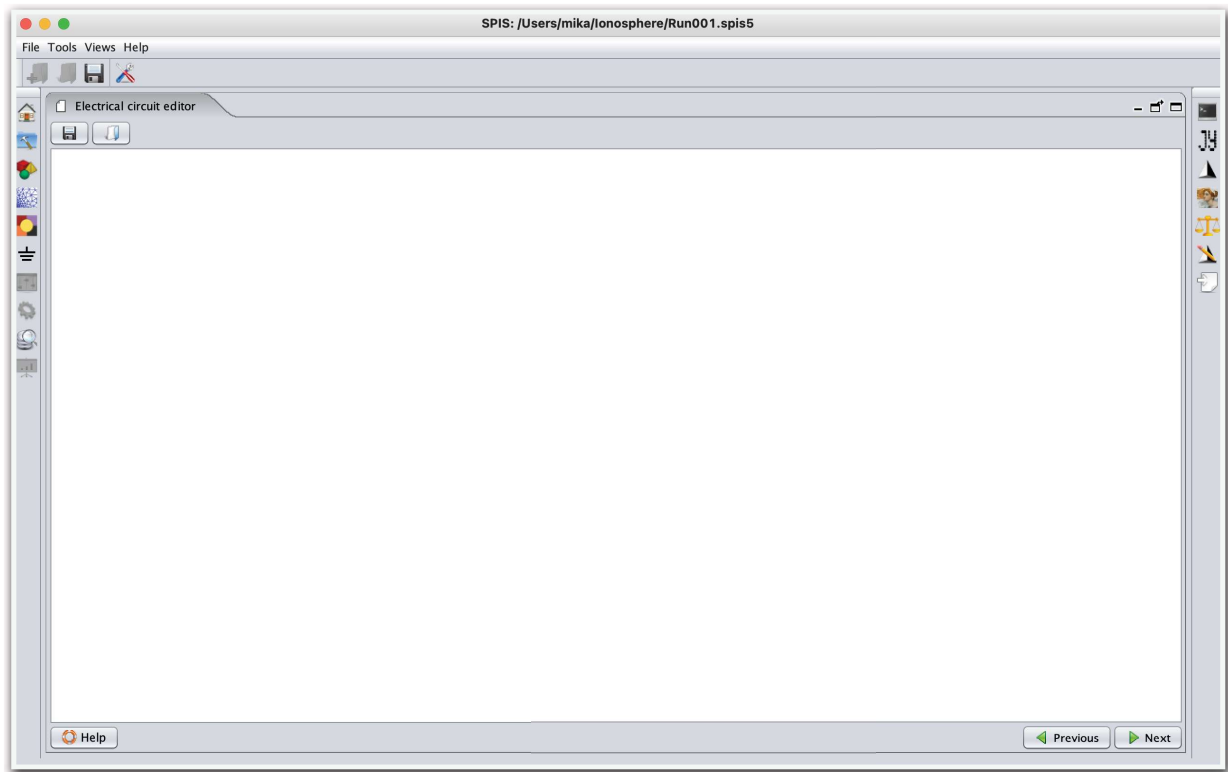


Figure 24 The electric circuit editor

## 2.9 The environment

The final step before starting the simulations is to define the environment in which the spacecraft is located. When issues arise during simulations, they are most often caused by poorly defined spacecraft geometry or mesh, or a badly defined environment. It is therefore especially important to have a solid understanding of the space environment of the spacecraft. Take the time to carefully review and double check all environmental parameters. If you are not an expert yourself, consult an expert to ensure that the parameters accurately represent the environment.

The window used to define the environmental parameters is named “Global parameters” and looks like the window shown in Figure 25.



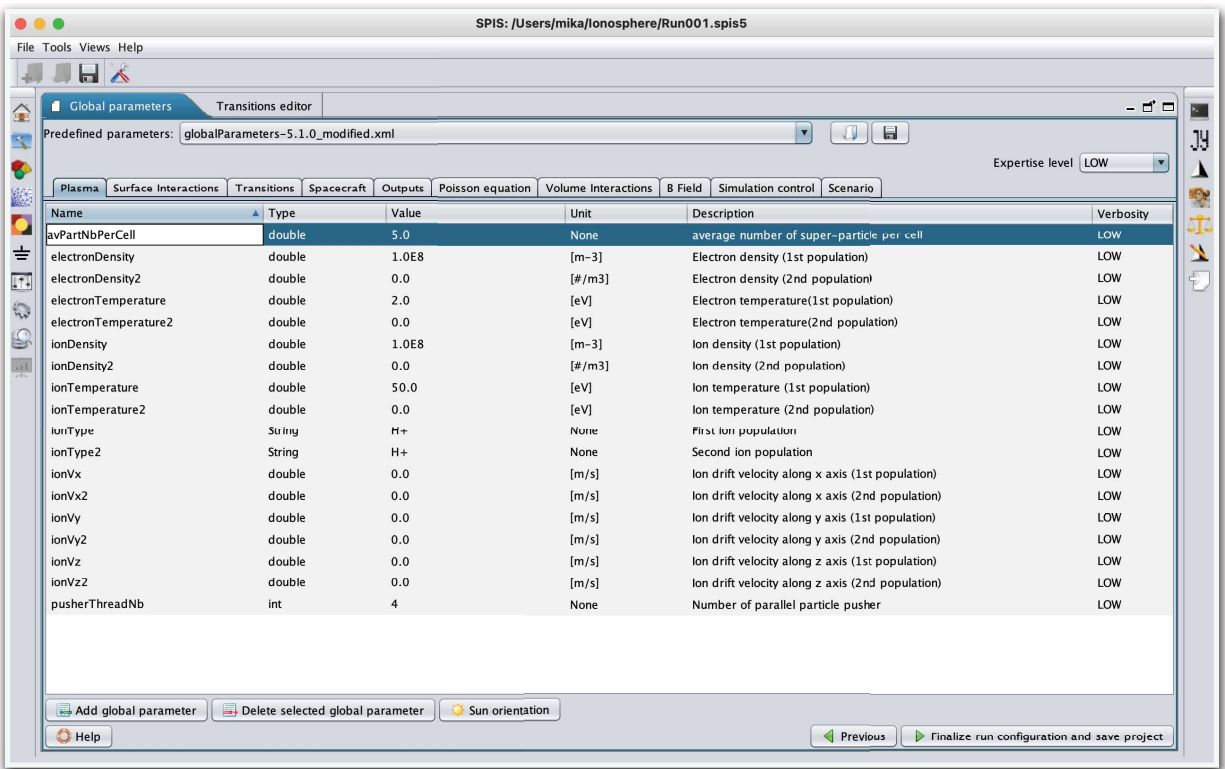


Figure 25 Here you define your spacecraft environment

If more parameters are displayed than those shown in Figure 25, then change the “Expertise level” to “LOW”. These are the initial parameters to be configured. The different options are “Plasma”, “Surface Interaction”, “Transitions” etc. Begin by defining the plasma environment. Set the electron and ion densities, “electronDensity” and “ionDensity”, which is given in m<sup>-3</sup>. By default, two different electron populations and two different ion populations can be defined. For example, let’s use the densities found in the ionosphere of Jupiter’s moon Ganymede at an altitude of around 400 km. Here the electron and ion density is around 100 cm<sup>-3</sup>. It is important to ensure that the environment is neutral, so that the total electron density equals the total ion density. Almost all natural plasma environments are quasineutral, which for the purposes of these simulations, can be treated as fully neutral.

Electron and ion temperatures and velocities can also be specified. For the Ganymede ionosphere typical values include an electron temperature of 2 eV and an ion temperature of 50 eV. The velocity here will mainly be due to the movement of the spacecraft, so set the plasma velocities to 0. The ion species present in the plasma can also be selected, hydrogen H<sup>+</sup> ions are used in this example. In addition, the number of particle pushers called “pusherThreadNb” can be selected, that is the number of available processor cores, and the average number of super-particles per cell called “avPartNbPerCell”, which will determine how noisy the simulations are. A larger number is better, but it is also computationally heavier, so start with a low number,



like 5 and increase it for more detailed simulations once the simulation is running smoothly.

Proceeding to “Surface Interaction” opens a window as shown in Figure 26. Here, the location of the Sun must be set, where the shown example has the Sun at a distance of 1 AU, from the spacecraft, on the positive z axis. For a spacecraft located in Ganymede's ionosphere, the solar flux must be scaled to match conditions at Jupiter's orbit. The average distance between Jupiter and the Sun is 5.2 AU, hence the Sun's location should be scaled to  $1/5.2^2 = 0.037$ . The position of the Sun can be reviewed by selecting “Sun orientation”, this will open up a window like the one shown in Figure 27. Please note that the location of the Sun and the spacecraft in this visualisation is, of course, not to scale.

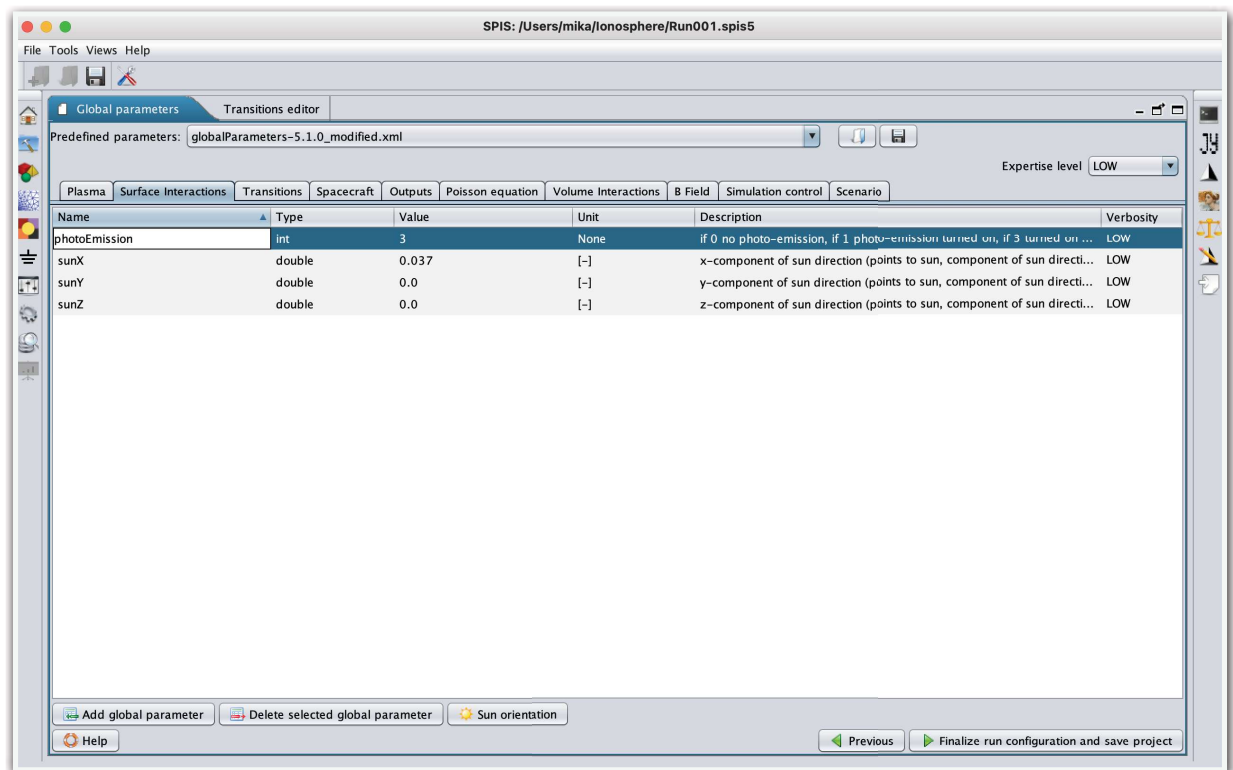


Figure 26 Where surface interactions are defined

Another option in the surface interaction window is the “photoEmission”. This parameter determines whether to include or exclude the emission of photoelectrons from the spacecraft. These are electrons that are emitted from the spacecraft surface due to the interaction with photons from the Sun (or any other photon source). If the spacecraft is in eclipse, this parameters should be set to 0, if the spacecraft is in sunlight the parameters should stay at 3.

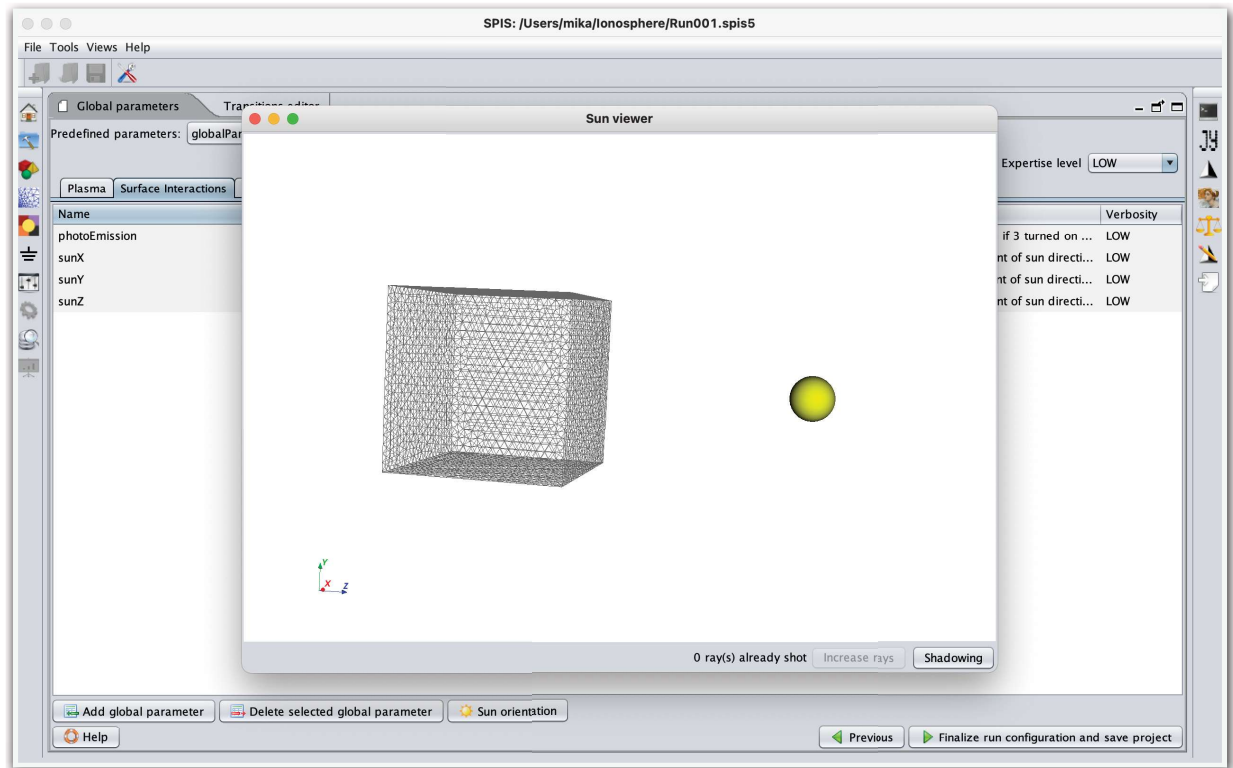


Figure 27 The Sun orientation viewer

For our simple example, default values are used for the following list of parameters, called “Transitions”, “Spacecraft”, “Outputs”, “Poisson equation”, “Volume Interactions”, and “Scenario”. The list after “Volume Interactions” defines the values of the magnetic field that the spacecraft is located in. Clicking on “B Field” will open a window like the one shown in Figure 28. Please be aware that the magnetic field should be given in Tesla. For our example, we use a magnetic field strength of 500 nT in the z direction.

The final step in the set up involves specifying the simulation “duration” and the simulation time step called “simulationDt”. The time step must be shorter than the duration, it is recommended that “simulationDt” is at least  $< \text{duration}/10$ . For our example, we use a “duration” of 1 s and a “simulationDt” of 0.05 s.

After setting the environmental parameters it is time to start the simulation by selecting “Finalize run configuration and save project”. This opens the simulation launch window shown in Figure 29. To start the simulation press “Launch simulation”. When the simulation is running, the time steps should be continuously updated in the “Log console” and some parameters, like “Individual currents on spacecraft”, should be shown in the window above the “Log console”, as shown in Figure 30.

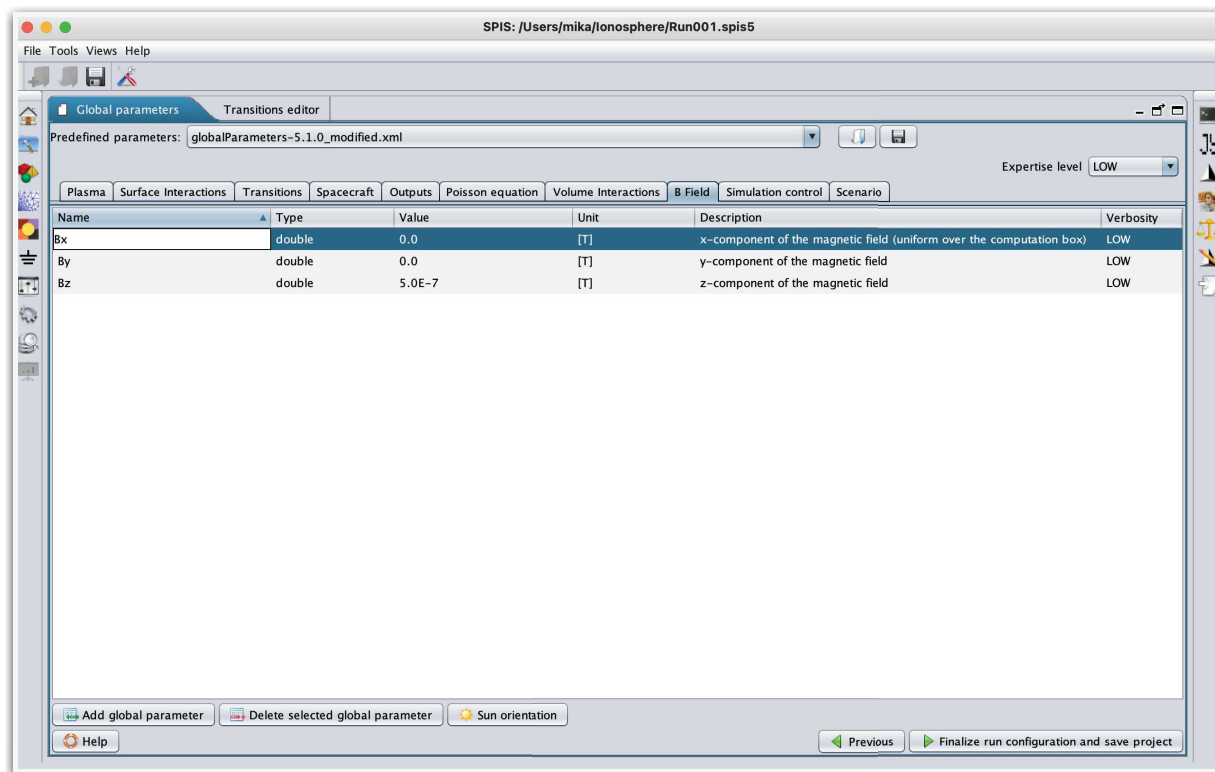


Figure 28 Where to set the magnetic field values

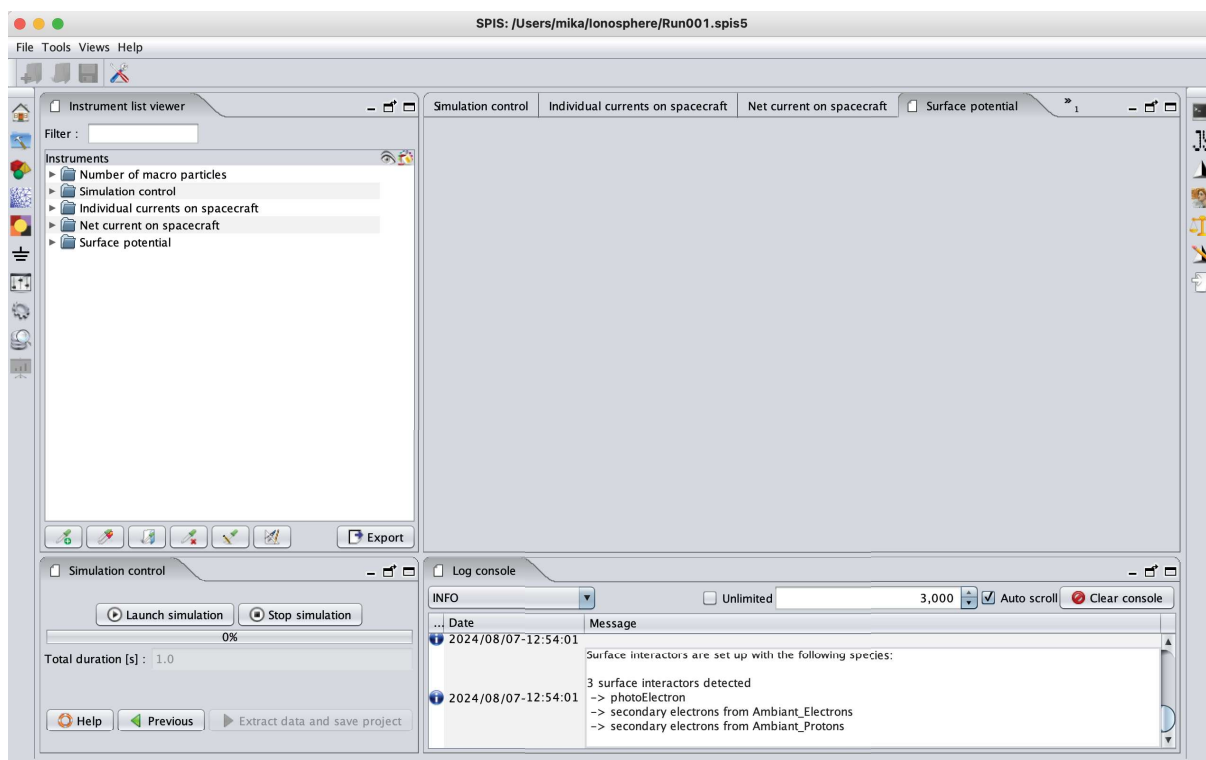


Figure 29 Where to launch the simulation

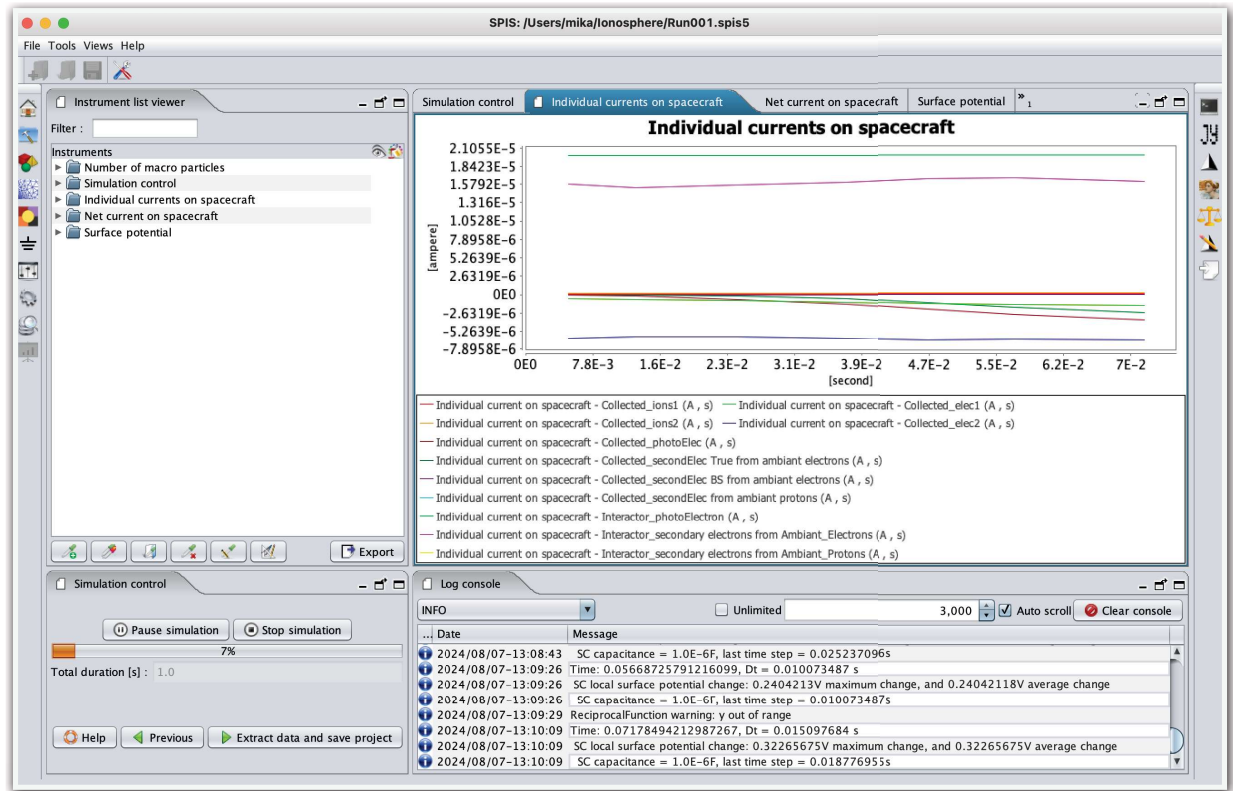


Figure 30 The simulation is running

## **Chapter 3. Spacecraft - environment interaction**

Chapter 2 gives an introduction on how to run SPIS simulations in general terms. However, using SPIS to study the impact of scientific measurements is generally more complex. We will therefore use the Jupiter Icy Moons Explorer (Juice) spacecraft in the solar wind as an example of how SPIS simulations can be used to improve data analyses.

### **3.1 The Juice mission**

The main science objectives of the Juice mission are to study Jupiter and the Jovian system, with a special focus on the habitability of Jupiter's icy moons. Juice is carrying several instruments for in-situ observations of the particle and field environments of the system, including the ionospheres of the icy moons. In order to ensure optimal performance of these instruments, the magnitudes of the spacecraft surface potentials must be low and a differential potential of maximum 1 V is required for certain instruments. In this chapter we will use SPIS simulations to study if these requirements will be fulfilled and if the interaction between the Juice spacecraft and its environment will impact the future Juice particle and field measurements.

Juice was launched on April 14, 2023, embarking on its long journey to Jupiter, where it will arrive in 2031. By 2034, Juice will enter into orbit around Jupiter's moon Ganymede and thereby achieve a historic milestone as the first mission to orbit a moon other than Earth's. Over the course of nine months, Juice will conduct detailed observations of Ganymede's unique environment before the mission concludes with a controlled impact on Ganymede, for planetary protection reasons. The spacecraft is equipped with ten instrument suites designed to explore Jupiter and its surrounding system in unprecedented detail. Among these, the Radio and Plasma Wave Investigation (RPWI) and the Particle Environment Package (PEP) are specifically dedicated to studying charged particles and electromagnetic fields. These instruments will provide crucial insights into the plasma environments throughout the Jovian system. These are also the instrument packages that will be most affected by the charging of the spacecraft, as they measure low-energy charged particles and electromagnetic fields. Additionally, the J-MAG instrument conducts in-situ measurements of the local magnetic field. Its observations are not expected to be affected by the surface charging of Juice in the solar wind environments, which will be studied in this chapter. Our simulations indicate spacecraft currents on the order of 1 mA, generating magnetic fields below the 1 pT noise threshold of J-MAG. As a result, J-MAG measurements are not further addressed in this study.

Juice is also equipped with several other instruments that are unlikely to be affected by spacecraft charging but are relevant to the spacecraft model description. These include:

- **Ganymede Laser Altimeter (GALA)** – designed to study the topography of the icy moons.
- **Optical camera system (JANUS)** – designed for imaging Jupiter's moons, analysing surface morphology and geological processes, and mapping Jupiter's clouds.
- **Moons and Jupiter Imaging Spectrometer (MAJIS)** – tasked with studying Jupiter's atmospheric composition and characterising the surfaces of the icy moons.
- **Radar for Icy Moons Exploration (RIME)** – employed to investigate the subsurface structures of the icy moons.
- **Sub-millimeter Wave Instrument (SWI)** – designed to analyse Jupiter's atmosphere as well as the exospheres and surfaces of the icy moons.
- **UV Imaging Spectrograph (UVS)** – dedicated to studying the exospheres of the icy moons, as well as Jupiter's upper atmosphere and aurorae.
- **Gravity and Geophysics of Jupiter and the Galilean Moons (3GM)** – will be used to explore Ganymede's gravity field, the subsurface oceans of Jupiter's icy moons, and Jupiter's atmosphere.

In addition, Juice will use its telecommunication system to conduct radio science investigations, referred to as the **Planetary Radio Interferometer and Doppler Experiment (PRIDE)**. Together, these instruments will provide a comprehensive examination of Jupiter and its moons, contributing to our understanding of their atmospheres, surfaces, internal structures, and habitability.

We use SPIS version 6.1.0 to simulate the interaction between the Juice spacecraft and the solar wind at 1 AU. This environment was chosen since it's the environment where the first Juice observation will be performed. During the first 4 years of the cruise phase, Juice will be located between 0.7 and 1.8 AU. Given this extended time spent in the solar wind near 1 AU, additional observations will also become available over the course of the cruise phase.

## 3.2 The spacecraft model

In order to perform the SPIS simulations we have built a detailed 3D model of the JUICE spacecraft. The model is presented in Figure 31. Panels a, b, c, and d show the -x, x, z, and -z sides of the spacecraft, respectively. The labelling of the spacecraft's different sides follows the spacecraft coordinate system:

- The **x-axis** points opposite to the high-gain antenna (HGA).
- The **y-axis** aligns with the direction of the solar panels.
- The **z-axis** is defined to complete the right-hand coordinate system.

The origin of the coordinate system is at 1.73 m below the center of the HGA. This coordinate system was defined by the prime contractor during the design phase of the mission and is, at the date of writing, the official Juice spacecraft coordinate system.

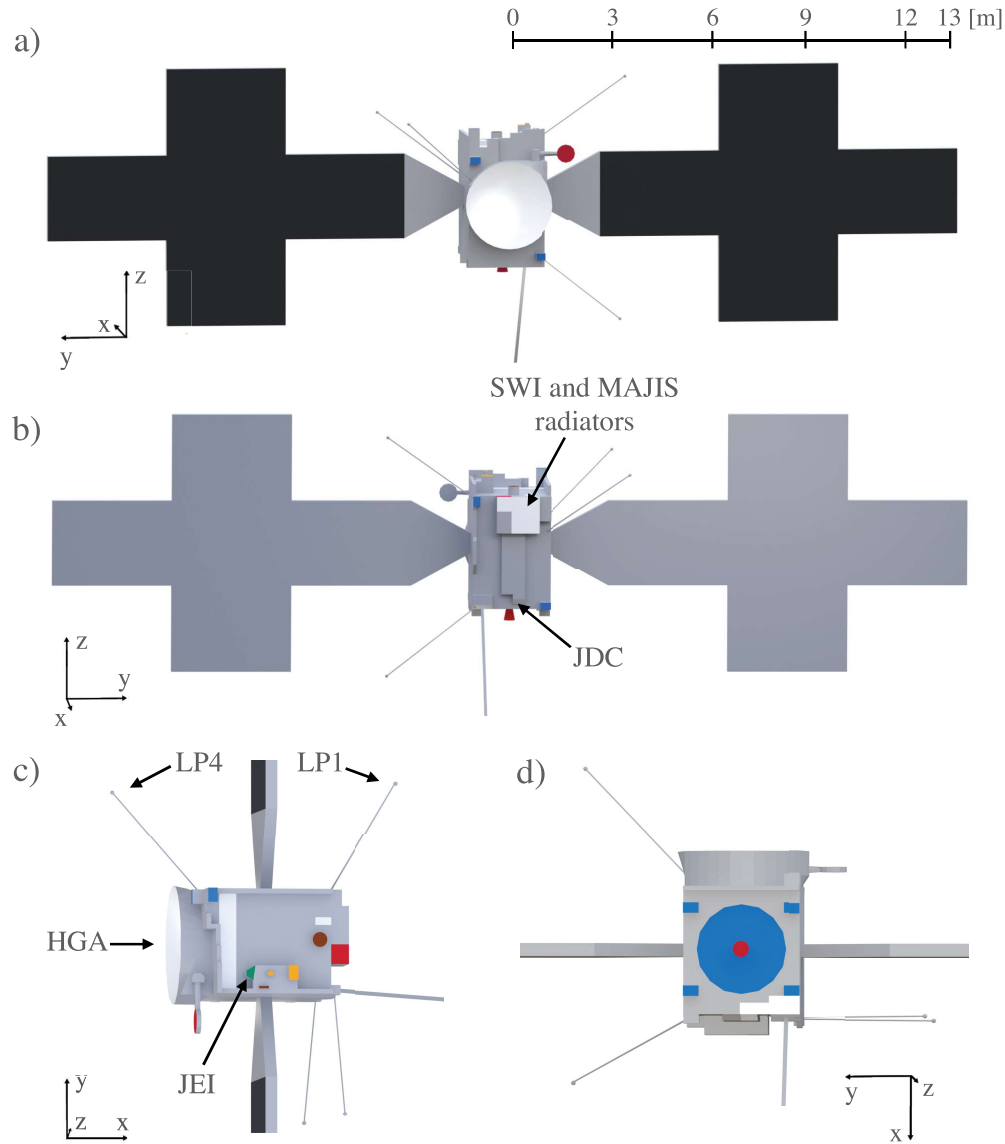


Figure 31 (a) The -x side of the spacecraft model, featuring the high-gain antenna (HGA) (white), the medium-gain antenna (MGA) (red), and the ITO-coated solar panels (black). (b) The x side of the spacecraft, highlighting the SWI and MAJIS radiators (white), thrusters (blue), and the back of the solar panels covered in black Kapton (gray). Arrows indicate the locations of the SWI and MAJIS radiators, as well as the PEP/JDC instrument. (c) The z side of the spacecraft, showing the top vault radiator (white), various PEP instruments (yellow and green), GALA (brown), and SWI (red). Arrows point to the HGA, the PEP/Jovian Electrons and Ions (JEI) instrument, and two RPWI Langmuir probes, LP1 and LP4. (d) The -z side of the spacecraft, showing the MLI around the main engine and thrusters (blue), the bottom vault radiator (white), and the main engine nozzle (red). To optimize simulation times, the RIME antenna is not included in the spacecraft model.

The spacecraft model, shown in Figure 31, includes a spacecraft bus measuring  $2.25 \times 2.50 \times 3.52$  m, a high-gain antenna (HGA) with a radius of 1.27 m, and solar panels extending 7.44 m along the z-axis and 12.07 m along the y-axis of the spacecraft model. This spacecraft model is built in the same way as described in Section 2.4. The model incorporates most of the onboard instruments and radiators. Figure 1c highlights the positions of the RPWI Langmuir probes (LPs), specifically LP1 and LP4, as their locations are relevant for discussing the simulation results later in this Chapter. However, the LPs are not included in the simulations, as their conductive surfaces and minimal surface area relative to the spacecraft would not significantly impact the simulation results, while their inclusion would increase computation time. Additionally, the PEP Jovian Electrons and Ions (JEI) instrument is shown in Figure 1c since it is also referenced in the discussion on the simulation results. For the simulations, the Juice solar panels are treated as equipotential surfaces without any exposed biased elements. The inclusion, exclusion, and modification of various spacecraft components were carefully evaluated to balance simulation accuracy with computational time and memory use. Multiple simulations were conducted with different configurations, such as incorporating or removing smaller spacecraft parts and adjusting surface material properties, to assess their impact on the computational time. This structured approach ensures that the spacecraft model maintains a high degree of accuracy while optimising simulation performance. The colour-coding in Figure 1 corresponds to specific surface materials and spacecraft parts:

- **Gray:** Black Kapton (spacecraft body, UVS, J-MAG, PEP/JDC)
- **Black:** Indium tin oxide (ITO) coating (solar panels)
- **White:** White paint Z93C55 (HGA, radiators)
- **Green:** White paint PSG 120 FD with ITO coating (PEP card rack radiator)
- **Brown:** Electrodag 501 (GALA, PEP/Jovian Neutrals Analyzer – JNA)
- **Blue:** Enbio SolarBlack (MLI around the main engine, thrusters)
- **Yellow:** Gold-equivalent coating (PEP/Neutral gas and Ion Mass spectrometer – NIM, PEP/Jovian Energetic Neutrals and Ions – JENI)
- **Red:** Steel (Medium Gain Antenna – MGA, SWI, main engine nozzle)

The materials of the spacecraft are implemented in the SPIS simulations as described in Section 2.7. The only dielectric material included in the simulations is the white paint Z93C55, which is covering the white surfaces in Figure 31. The material properties used to simulate this paint is listed in Appendix B.

### 3.3 The solar wind at 1 AU

JUICE conducted its first measurements in the solar wind near Earth during the Near Earth Commissioning Phase (NECP), which took place from April 15 to July 15, 2023. These measurements were performed while the spacecraft was positioned between



1,500 and 3,200 Earth radii ( $1 R_E = 6,378 \text{ km}$ ) from our planet. This is far from Earth's magnetosphere, hence the measurements were of the undisturbed solar wind.

To simulate the interaction between the spacecraft and its environment, we need to know the properties of the ambient solar wind. These properties have been obtained from various solar wind studies, which are discussed in the following paragraphs. The environmental parameters used in the simulations are summarised in Table 1. In Table 1, column 1 lists the parameter names, column 2 provides the values used in the simulations, column 3 presents values from different studies, and column 4 cites the corresponding references. When both mean values and ranges are available, the range is provided in parentheses after the mean value.

Solar wind electrons are simulated as two populations: core (cold) and halo (hot) electrons. A third population, strahl electrons, typically constitutes only a small fraction of the core electron density (Štverák et al., 2009) and does not significantly contribute to spacecraft surface charging; therefore, it is excluded from the simulations. The core and halo electron densities ( $n_{e,c}$  and  $n_{e,h}$ ) and temperatures ( $T_{e,c}$  and  $T_{e,h}$ ) are derived from the studies listed in Table 1 column 3. The core electrons are simulated using a Maxwellian distribution, while the halo electrons are simulated using a Kappa distribution. To represent typical solar wind conditions, we use mean values for the ion density ( $n_i$ ), solar wind velocity ( $v_{s,w}$ ), and magnetic field strength ( $|B|$ ), based on the dataset presented in Michotte de Welle et al. (2022). This dataset, hereafter referred to as M1, includes measurements from Cluster, Double Star, Themis, and MMS collected between 2001 and 2021. The magnitude of the mean solar wind velocity ( $|v_{s,w}|$ ) is also obtained from M1. In the spacecraft coordinate system, the solar wind is directed along the x-axis, meaning it hits the front of the spacecraft, shown in Figure 1a. From the M1 dataset, we have also obtained the mean magnitude of the interplanetary magnetic field (IMF),  $|B|$ , which is aligned along the y-axis in the spacecraft coordinate system.

**Table 1**  
Environmental Parameters Describing the Typical Solar Wind

Parameter	Input value	Reference values	References
$n_{e,c}$	$5.4 \text{ cm}^{-3}$		Assuming $n_{e,c} + n_{e,h} = n_i$
$T_{e,c}$	10 eV	10, 12.2, 10, 8.5–10	Gosling (2014), Wilson et al. (2018), Lazar et al. (2020), Pierrard et al. (2020)
$n_{e,h}$	$0.2 \text{ cm}^{-3}$	0.2, 0.2–0.3, 0.2	Maksimovic et al. (2005), Lazar et al. (2020), Pierrard et al. (2020)
$T_{e,h}$	60 eV	60, 60–66	Lazar et al. (2020), Pierrard et al. (2020)
Kappa	5	4.9, 4.5–5, 5–5.7, 5–5.5	Maksimovic et al. (2005), Štverák et al. (2009), Lazar et al. (2020), Pierrard et al. (2020)
$n_i$	$5.6 \text{ cm}^{-3}$	5.6, 6.4 (0.03–72), 6 (0.5–117)	M1, M2, Venzmer and Bothmer (2018)
$T_i$	8 eV	8, 4.3–10.3, 12.7, 9	M2, Gosling (2014), Wilson et al. (2018), Venzmer and Bothmer (2018)
$ v_{sw} $	413 km/s	413, 427, 468, 410 (156–1,189)	M1, M2, Gosling (2014), Venzmer and Bothmer (2018)
Ion species	$H^+$		
$v_{s/c,x}$	–1.0 km/s		From the spacecraft trajectory file Crema 5.0b23.1
$v_{s/c,y}$	–33 km/s		
$v_{s/c,z}$	–0.04 km/s		
$ B $	5.5 nT	5.5, 5.7, 6.2, 6 (0.4–62)	M1, M2, Gosling (2014), Venzmer and Bothmer (2018)

The M1 dataset has been compared with results from Venzmer and Bothmer (2018), who analysed hourly OMNI data from 1963 to 2016 to determine the frequency distribution of proton temperature, as well as solar wind density, velocity, and magnetic field strength. Despite being recorded by different spacecraft, the two datasets show strong agreement. Additionally, the M1 dataset closely aligns with mean values derived from OMNI data spanning 1995 to 2021, referred to as M2 in Table 1. This time period was selected to facilitate a direct comparison between the mean values of M1 and measurements from the ACE and WIND spacecraft.

Laboratory studies of photoelectron emission from commonly used spacecraft materials indicate that photoelectron distributions generally follow a Maxwellian shape, with temperatures ranging from 1.2 to 1.5 eV (Grard, 1973). Based on these findings, we have adopted a Maxwellian photoelectron distribution with a temperature of 1.3 eV. We have employed the PIC method, to simulate both the ion and electron populations.

In this study, we did not account for variations in the solar UV flux and instead used the reference values provided by SPIS. As an initial approach, this is considered sufficient. However, when simulating actual measurements, the influence of solar UV flux variability should be taken into consideration, as it may affect the final surface potentials, particularly in cases where photoelectron currents drive the spacecraft charging.

The environmental parameters listed in column 2 in Table 1 are implemented in the SPIS simulations as described in Section 2.9.

### **3.4 The simulation results: Interaction in the solar wind**

The SPIS simulations provide valuable insights that will be crucial for analysing the future measurements from JUICE. The primary result is the spacecraft's surface charging, illustrated in Figure 32. This figure shows that the spacecraft body and its solar panels (spacecraft ground) will charge up to approximately 6 V, while surfaces covered in dielectric material (the white paint Z93C55) will exhibit varying potentials. The most positively charged surface is the HGA, which will reach a potential of about 8 V. Positioned towards the Sun and exposed to the solar wind, the HGA experiences significant photoelectron emission and ion accumulation, making its charging effects more pronounced compared to other spacecraft components.

The spacecraft model also includes several radiators coated with Z93C55. These radiators, shielded from solar radiation by sun shields or other spacecraft structures, will charge negatively. The most negatively charged surface is the bottom vault radiator, which reaches approximately -36 V. However, the accuracy of the Z93C55 surface potentials should be interpreted with caution, as the material properties of this paint are less well-defined compared to the conductive surfaces of the spacecraft.

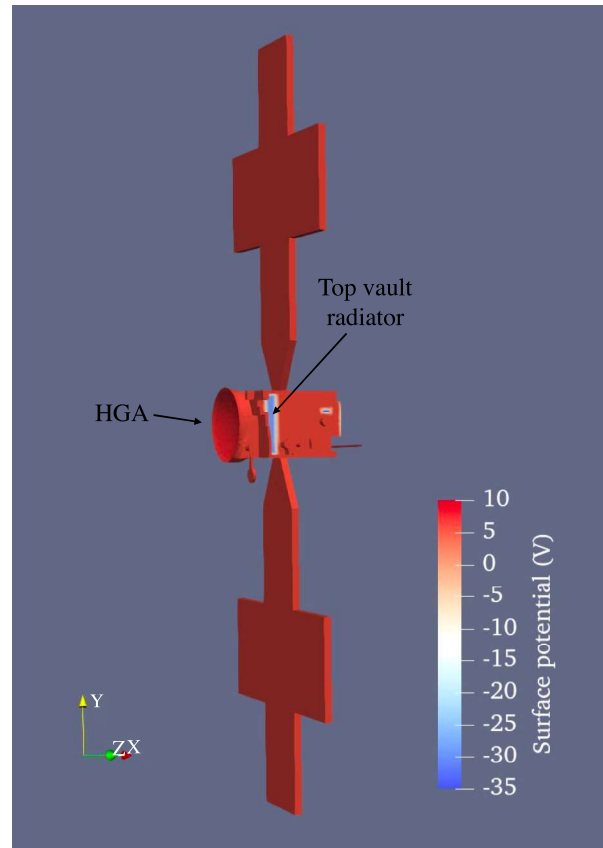


Figure 32 The simulated surface potential of JUICE in the mean solar wind environment. The spacecraft will charge to approximately 6 V and the HGA, a dielectric surface facing directly toward the Sun as it functions as a sunshield, will reach a potential of around 8 V. The radiators, also dielectric surfaces, will charge to potentials ranging between -26 V and -36 V. These variations in potential arise due to the relative positioning of the surfaces with respect to the Sun and solar wind. The arrows indicate the locations of the HGA and the top vault radiator.

The bottom vault radiator, being fully shielded from the Sun, does not emit photoelectrons but continues to accumulate solar wind electrons. Combined with a negligible accumulation of solar wind ions, this leads to a negative surface charge. The same principle applies to the other radiators, which also acquire negative potentials.

If the spacecraft were oriented differently relative to the Sun and solar wind, the surface potentials would be different. However, within approximately 1.3 AU, the HGA must function as a sun shield to maintain the spacecraft at a safe temperature. As a result, the simulated spacecraft orientation will be maintained for most of the

cruise phase while the spacecraft is within 1.3 AU, except for brief periods when spacecraft rolls are necessary, such as for instrument calibrations.

Figure 33 (panels a to c) illustrates the density distribution of different particle populations around the spacecraft along three lines originating from the center of the spacecraft. These lines pass through the positions of two RPWI/Langmuir probes (panels a and b) and the PEP/JEI instrument (panel c). The plots display the densities of photoelectrons (dashed line), ions (dotted line), core electrons (solid line), and halo electrons (dash-dotted line). In panels a and b, the vertical black lines indicate the positions of LP1 (panel a), located on the back of the spacecraft, and LP4 (panel b), positioned on the front (see Figure 31c). The JEI instrument is centred at  $x = 0$  in Figure 33c.

Figure 33 (panels a to c) demonstrate that the spacecraft will be surrounded by a dense photoelectron cloud, with densities significantly exceeding that of the solar wind. This is due to both the spacecraft's close proximity to the Sun during this phase of the mission and the typically low density of the solar wind. Near the sunlit surface on the  $-x$  side of the spacecraft, the photoelectron density can reach over 130 times the solar wind density (not shown). Once emitted, photoelectrons are affected by the local magnetic and electric fields and are typically attracted back to the positively charged spacecraft. As a result, they are also present behind the spacecraft. On the back side (positive  $x$  direction), near the JDC instrument, the photoelectron density is closer to twice the solar wind density. Panels a and b of Figure 33 depict particle densities on the  $y$  side of the spacecraft, while panel c shows densities around the JEI instrument, which is located on the  $z$  side of the spacecraft (see Figure 31c). Despite these instruments not being located on the spacecraft's sunlit surface, photoelectrons remain the dominant, or one of the primary, particle populations at all three instrument locations. This must be considered during data analysis of the observations from these instruments. The densities around LP2 and LP3, located on the  $-y$  side of the spacecraft (see Figure 31), closely resemble those observed for LP1 (panel a) and are therefore not included in Figure 33.

It is important to note that LP measurements will also be influenced by photoelectrons and secondary electrons generated by the probes themselves (see, e.g., Holmberg et al., 2012, 2017; Wang et al., 2015). These effects are not included in the presented simulations, as they fall outside the scope of this initial study. However, based on the results in Figures 33a and 33b, it is reasonable to expect that these contributions will significantly impact the currents measured by the LPs in a typical solar wind environment and must be properly accounted for in the data analysis.

Figure 33d illustrates the potential along lines extending from the center of the spacecraft and passing through LP1 (black, corresponding to the density profile in panel a), LP4 (blue, corresponding to panel b), and the JEI instrument (red, corresponding to panel c). The spacecraft surface is defined at  $x = 0$ . The LPs are

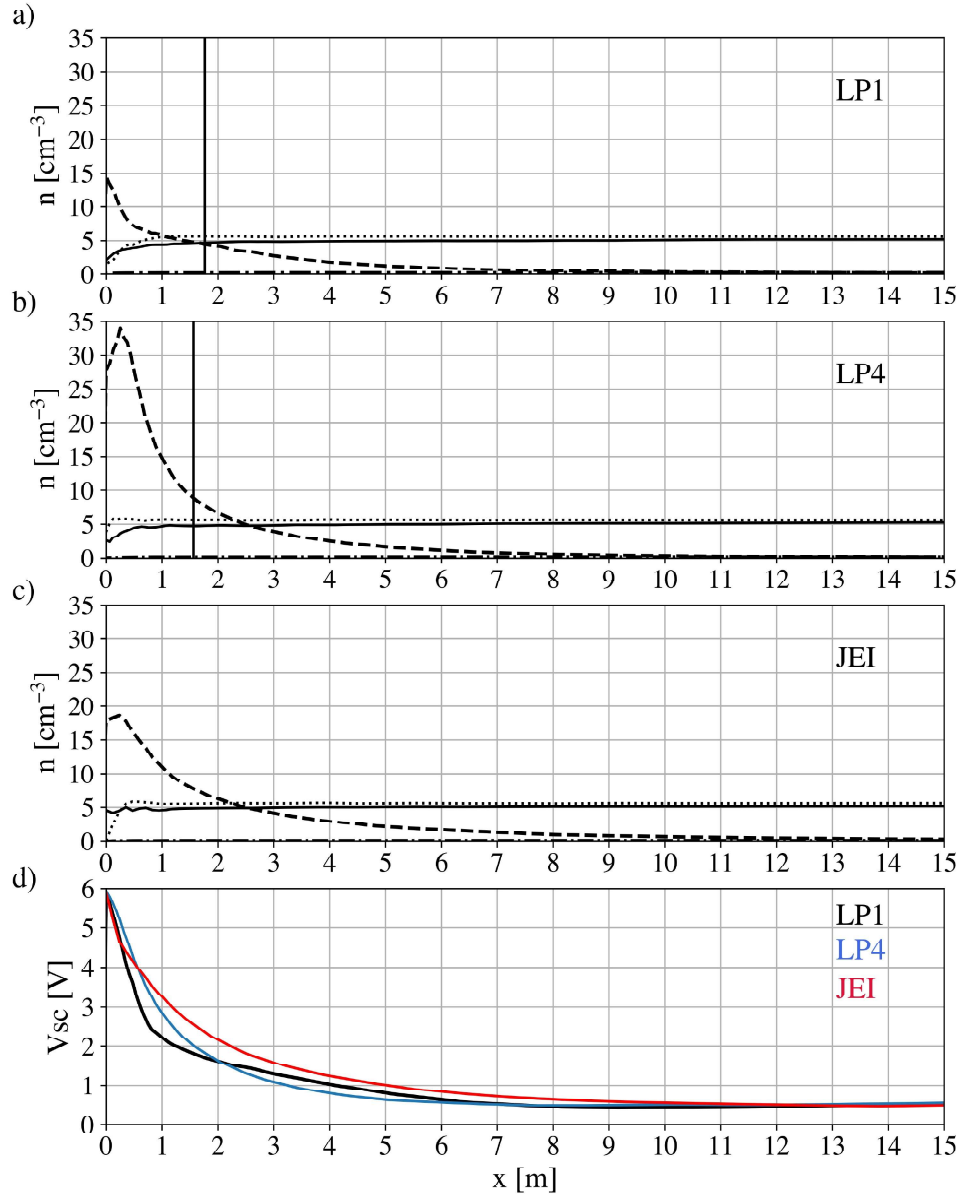


Figure 33 The figure presents particle densities and potentials from the typical solar wind environment simulations. (a) Particle densities along a line extending 15 meters from the spacecraft's surface (set to 0), starting at its center. This line intersects LP1's location (marked by a black vertical line), which is positioned on the opposite side of the HGA (see Figure 31c). The graph displays the densities of photoelectrons (dashed line), ions (dotted line), core electrons (solid line), and halo electrons (dash-dotted line). (b) Particle densities along a similar 15-meter line, this time passing through LP4's location (black vertical line), which is on the same side as the HGA (see Figure 31c). The particle populations shown are the same as in panel (a). (c) Particle densities along a 15-meter line intersecting the PEP/JEI instrument's position at  $x = 0$ , following the same format as panels (a) and (b). (d) Electric potential variations along three 15-meter lines passing through LP1 (black), LP4 (blue), and the JEI instrument (red).

designed to measure electric fields under the assumption of a symmetric potential field around the spacecraft. However, Figure 33d demonstrates that the potential can vary by more than 1 V at the same distance from the surface. This discrepancy must be corrected for to ensure accurate electric field measurements.

The potential asymmetry arises from both the use of materials with varying properties and the asymmetric geometry of the spacecraft. Figure 33d illustrates that the potential along the LP1 line (black) decreases more rapidly than along the LP4 (blue) and JEI (red) lines. This occurs because LP1 is located near the MAJIS and SWI radiators on the back of the spacecraft (see Figure 31b), which are negatively charged and influence the local potential field. Similarly, the potential along the JEI line (red) declines more steeply due to its proximity to the top vault radiator (shown in Figure 32), which is also negatively charged. However, this effect is localised, noticeable only within approximately 0.2 m of the spacecraft surface, as the overall positive potential of the spacecraft suppresses the influence of the potential of the top vault radiator. Beyond this region, the JEI potential decreases more gradually than the LP4 potential due to the asymmetric shape of the spacecraft.

Figure 34a presents a cross-section of the ion density around the spacecraft, highlighting the formation of an ion wake. This depletion of ions occurs because the ions are unable to refill the region behind the spacecraft when the relative velocity between the plasma and the spacecraft exceeds the thermal speed of the ions. The ion density drops to nearly  $0 \text{ cm}^{-3}$  on the x side surface of the spacecraft. As a result, the

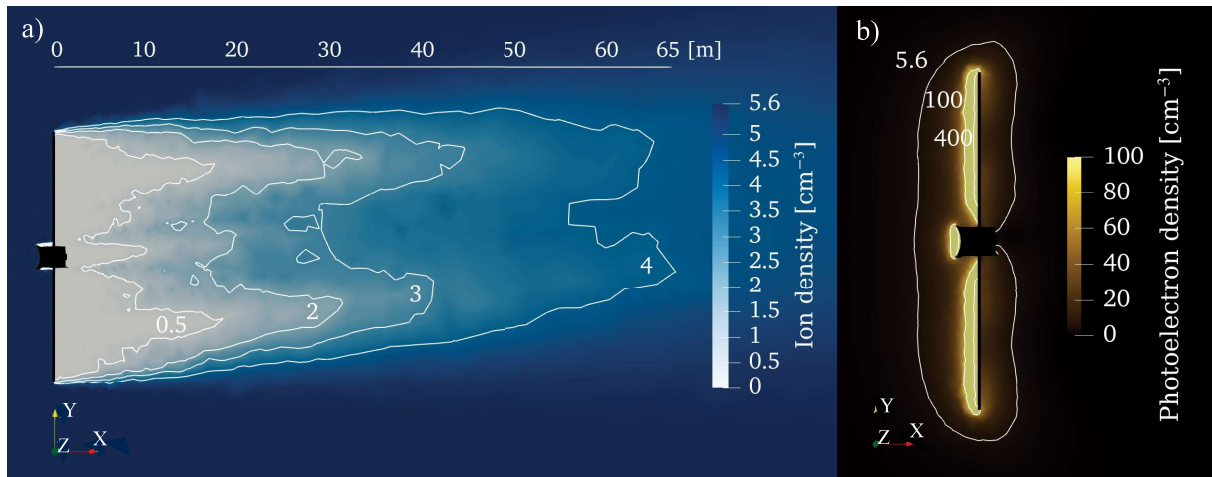


Figure 34 (a) A cross-section of the ion density in the xy plane, cutting through the center of the JUICE spacecraft (shown in black), under typical solar wind conditions. The ion wake is distinctly visible as a region of ion depletion behind the spacecraft. White isolines indicate densities of 0.5, 2, 3, and  $4 \text{ cm}^{-3}$ . The Sun is positioned in the -x direction, with the solar wind flowing along the x axis. (b) The photoelectron density distribution around the JUICE spacecraft in the typical solar wind environment. White isolines mark density levels of  $5.6 \text{ cm}^{-3}$  (corresponding to the solar wind density),  $100 \text{ cm}^{-3}$ , and  $400 \text{ cm}^{-3}$ .

PEP/JDC instrument, which is positioned on the x side (see Figure 31b), will be unable to detect solar wind ions with this spacecraft orientation, which will be the default spacecraft attitude for the portion of the mission when JUICE is within 1.3 AU. Figure 34a illustrates that the ion wake extends far beyond the spacecraft itself. For instance, at 65 meters behind the spacecraft, the ion density is reduced to  $4 \text{ cm}^{-3}$ , compared to the undisturbed solar wind density of  $5.6 \text{ cm}^{-3}$ .

Figure 34b depicts the photoelectron density surrounding the spacecraft, confirming the findings from Figure 33 (panels a to c), which indicate that photoelectrons will be the dominant particle population in the typical solar wind environment. The highest photoelectron density, recorded just above the solar panels, reaches  $760 \text{ cm}^{-3}$ . Since the spacecraft is positively charged and photoelectrons have energies of only a few electron volts, they will remain confined around the spacecraft. This also makes it possible for the photoelectrons to reach the spacecraft surfaces that are in shadow.

### 3.5 Discussion

The findings of this study highlight the necessity of accounting for spacecraft charging when analysing the future cold plasma measurements taken by JUICE. Our focus has been on spacecraft charging in the solar wind at 1 AU, as this is where JUICE's first particle and field observations were recorded. This environment therefore offers the earliest opportunity to compare simulation results with real observations and to begin using simulations as a tool for improving the data analysis. Our results demonstrate that the interaction between the JUICE spacecraft and the surrounding plasma will have a substantial impact on the spacecraft charging and modifies the local particle environment, both by the large production of photoelectrons from the spacecraft and the formation of an ion wake in its vicinity.

For a typical solar wind environment at 1 AU, based on 20 years of solar wind observations, our simulations suggest that JUICE will charge to approximately 6 V, with dielectric surface potentials ranging from -36 V to 8 V. This predicted spacecraft potential aligns closely with the 5 V measured during the first RPWI Langmuir probe sweep conducted in the solar wind during the NECP (Wahlund et al., 2025). This surface potential will affect cold plasma measurements from the JDC and JEI particle analysers by distorting particle trajectories and altering the energy of surrounding particles (Bergman et al., 2020a, 2020b; Bochet et al., 2023). Consequently, these measurements must be corrected to account for spacecraft charging effects. To determine the precise magnitude of these corrections, dedicated SPIS simulations tailored to each instrument and particle population are required.

In a typical solar wind environment, the JUICE spacecraft will be surrounded by a dense cloud of photoelectrons, with peak densities reaching up to  $760 \text{ cm}^{-3}$  near the sunlit surface. At the locations of the four Langmuir probes (LPs), photoelectron densities will range between 5 and  $10 \text{ cm}^{-3}$ , while around the cold plasma instrument



JEI, the density will be approximately  $20 \text{ cm}^{-3}$ . The spacecraft's potential structure exhibits variations of more than 1 V at the same radial distance, a factor that must be considered when conducting electric field measurements. Additionally, an ion wake forms behind the spacecraft, with ion depletion detectable over 65 meters away. When analysing Langmuir probe measurements, it is crucial to account for the wake structure to avoid misinterpreting the ion density reduction as a depletion in the ambient solar wind. However, our simulations indicate that, due to the spacecraft's orientation and the positioning of the Langmuir probes, none of them are located within the ion wake in the studied case. Conversely, the PEP/JDC instrument is consistently positioned within the ion wake, preventing it from measuring solar wind ions unless the spacecraft's attitude changes, for example, during a spacecraft roll.

The findings of this study will play a crucial role in developing methods to correct JUICE's charged particle and field measurements in the solar wind at 1 AU, accounting for the effects of spacecraft-environment interactions. As highlighted throughout this article, spacecraft charging influences these measurements in multiple ways. The next step in refining correction techniques will depend on the specific type of measurement being addressed. However, a general approach involves using SPIS simulations tailored to particular measurement types and space environment conditions. These simulations will provide a detailed understanding of how the spacecraft's interaction with its environment impacts each measurement, forming the foundation for the necessary data corrections.

## Chapter 4. In-situ particle measurements perturbations

This chapter focuses on how to use SPIS to simulate the measurements of a specific instrument, environment and particle type. The method can relatively easily be adapted to different environments and particle types, but is specific for the kind of instruments type used in this case study. This study was performed as a master thesis project by Derek van Winden and presented in the master thesis “Juice/JDC ion measurement perturbations caused by spacecraft charging in the solar wind and Earth’s magnetosheath”.

For this study we will focus on the ion measurements of the Jovian Plasma Dynamics and Composition Analyser (JDC), which is part of the Juice Particle Environment Package (PEP). This project aims to study the distortions of JDC’s particle measurements caused by spacecraft charging that occur while Juice is in Earth’s magnetosheath during the cruise phase. In this way, key distortions can be identified and compared with possible in-situ measurements to better understand how JDC measurements are impacted before Juice arrives in the Jovian system and the science phase starts. Spacecraft charging alters the energy and flow direction of the detected particles, resulting in larger errors for environmental parameters (velocity, plasma temperature, particle number density) that are derived from the measurements. Furthermore, spacecraft charging, especially if the effect is strong, can prevent the detection of low-energy ions and electrons altogether because they are repelled by the spacecraft. This can become a considerable problem when mapping particle populations in the new and unstudied environments that Juice will encounter during its 3.5-year tour of the Jovian system. The main research question of this study is: *How are JDC ion measurements distorted by the charging of Juice in Earth’s magnetosheath?*

### 4.1 The JDC instrument

JDC is a particle analyser that is part of the Juice Particle Environment Package (PEP). JDC can measure energy/charge, mass/charge ratios, and the arrival direction of the particle and has the task of studying the ions and electrons in the Jovian system. The instrument can detect particles in the energy range between 1 eV/q and 35 keV/q with an energy resolution of 12 % (Wittmann 2022). JDC is located on the back of the spacecraft as shown in Figure 31b. A picture of the instrument is shown in Figure 35.

JDC is a top hat spherical analyser, meaning that incoming particles enter the instrument from the side through the deflector (component 1 in Figure 36). If the direction and energy of the particle are compatible with the voltage applied to the deflector electrodes, it is guided into the electrostatic analyser (component 2). There,



Figure 35 A photo of JDC with a coin and ruler for scale. The instrument consists of two cylinders on top of each other, topped by a cone. The handles around the instrument serve to ease transport and are not a part of the instrument. Credit: Philipp Wittmann, IRF Kiruna.

only a particle that has the right energy - corresponding to the voltage difference that is applied across the electrodes - will pass unhindered, otherwise, the particle will hit one of the electrodes. In this way, the electrostatic analyser effectively acts as a filter for particle energies. The next component the particle encounters is the start surface (component 3), a grating in which the particle scatters within one of the channels, thereby creating one or more secondary electrons. These secondary electrons enter an electron multiplier (component 4) where they initiate a cascade of electrons, generating the start signal. Meanwhile, the original particle (potentially with an altered charge) continues onward through the cylindrical reflectron (component 5) until it reaches the stop detector (component 6) which generates the stop signal. Alternatively, if the particle is a low energy positive ion, it is deflected by the electric field and collides with the stop surface at the top of the reflectron. This collision generates at least one secondary electron, which is then accelerated away from the surface by the electric field until it hits the stop detector where it produces a stop signal. Since the distance between the start and stop surfaces is known, the particle's velocity can be calculated from its time of flight (that is the time between the start and

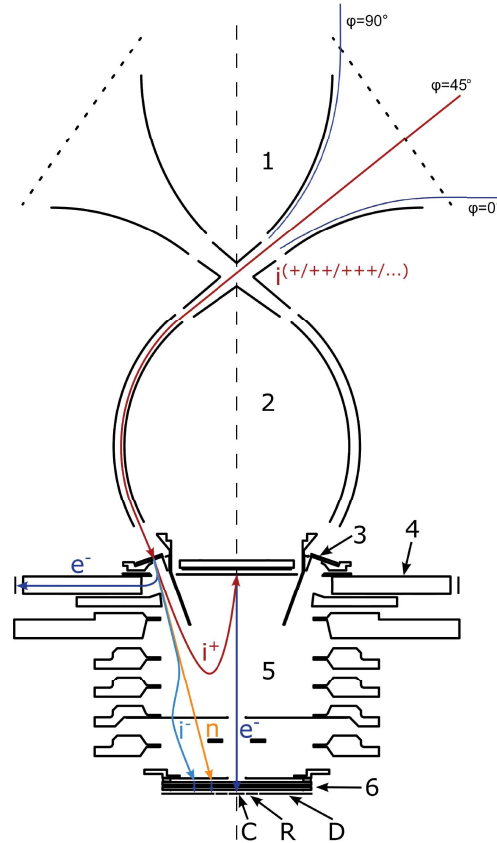


Figure 36 A schematic cross-section of JDC that shows the operation of the particle detector. The components, numbered in the order in which the particle passes them are the deflector (1), electrostatic analyser (2), start surface (3), electron multiplier (4), reflectron (5), and stop detector (6). The trajectories of the detected ion and all other particles involved in a single detection are drawn, and the maximum and minimum acceptance angles of 90 and 0 degrees respectively are also indicated. Adapted from Wittmann (2022).

stop signals). Given that the particle's energy is also known its mass can be determined simultaneously.

The instrument coordinate system, illustrated in Figure 37, is defined with respect to the base of JDC's top cone. In this system, an elevation angle of  $\varphi = 0^\circ$  is defined to be parallel to the base of the cone, and an angle of  $\varphi = 90^\circ$  is parallel with the cone's symmetry axis. The azimuthal coordinate  $\theta$  goes from 0 to  $360^\circ$  with increasing sector number, where a line with an angle of  $\theta = 0^\circ$  crosses the centre of sector 0. The azimuthal field of view of the instrument is divided into 16 sectors, associated with the 16 electron multipliers, and the 12 viewing directions in elevation correspond to the 12 different voltage settings of the deflector. Therefore, the hemispherical field of view of the instrument is divided into  $12 \times 16 = 192$  angular pixels. A pixel corresponds to an

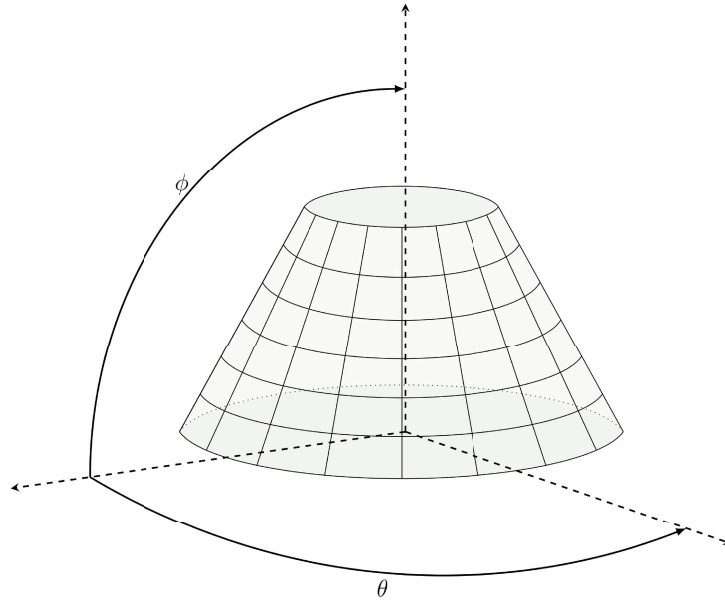


Figure 37 The coordinate system of the instrument is defined with respect to the base of the instrument's conical top. The elevation  $\phi$  rises with increasing elevation number, and the azimuth  $\theta$  increases with increasing sector number.

angular field of view, where each pixel has its range of acceptance angles within which it can detect particles. Therefore the term 'pixel' shouldn't be understood in the context of spatial pixels, as found in screens or the CCD and CMOS arrays used in digital imaging. The instrument's pixels purely arise from the fact that the instrument has 16 electron multipliers and 12 different voltage settings of the deflection system that are applied for each energy. This means that the size and viewing direction of each pixel are dependent on the energy of the particle, where generally the size decreases with increasing energy. For all the elevation levels the angular pixel size is  $19.5^\circ$ , or less, instead of  $22.5^\circ$  because the field of view is partly obstructed by the instrument's internal support structures.

Figure 38 shows an illustration of the full field of view of JDC for a particle energy of 707 eV, used here as a representative example. The angular coverage of each pixel is indicated as a coloured rectangular surface on a unit sphere. Arrows perpendicular to these surfaces indicate the viewing directions of the pixels at their respective (bary) centre. It can also be seen that the azimuthal field of view decreases with increasing azimuth, which, as mentioned earlier, is caused by the internal structure of the instrument. In Table 2 are listed the calibrated viewing directions and sizes of each pixel on JDC as measured before the launch. One should note though, that the azimuthal pixel sizes in the table are given in the instrument coordinate system (with respect to the base of the cone) while in SPIS, acceptance angles are specified with respect to the central viewing direction of each pixel. Therefore the tabulated values

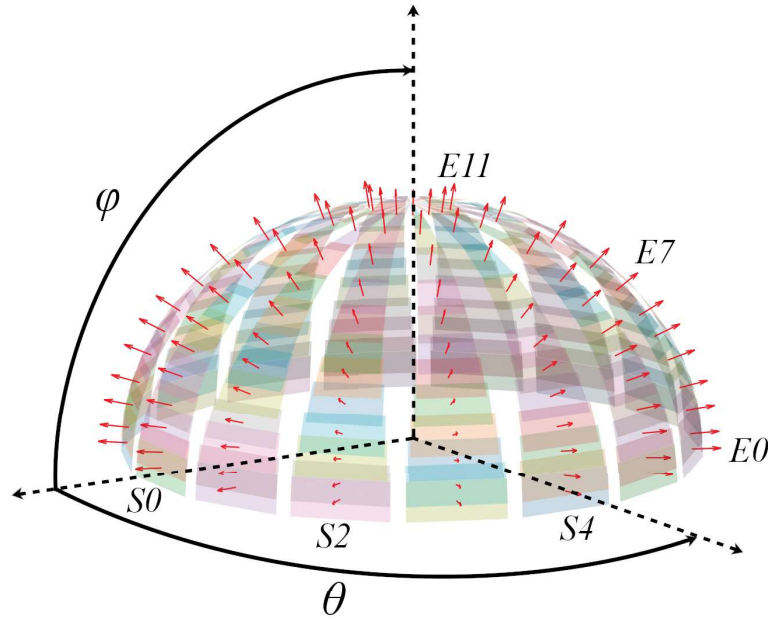


Figure 38 The field of view of all JDC pixels for particle energies of 707 eV. The red arrows indicate the central viewing directions of every pixel. The S stands for sector and E for elevation level.

have to be converted to the local detector basis before they can be used in SPIS. This conversion can be done with the following formula:

$$\Delta\theta_{SPIS} = 2\arctan[\cos(\phi)\tan(\Delta\theta/2)]$$

Table 2. The average calibrated elevation angles and pixel sizes for each elevation level of JDC for a particle energy of 707 eV. All values are given in 2 decimals, but the actual precision is more likely to be lower with 1 decimal instead. The data was supplied by P. Wittmann.

Elevation level	Elevation angle $\phi[^\circ]$	Angular pixel size $\Delta\phi[^\circ]$	Angular pixel size $\Delta\theta[^\circ]$
0	5.74	8.82	19.51
1	9.28	9.14	19.51
2	14.73	8.98	18.45
3	20.05	8.85	17.46
4	26.70	9.16	16.22
5	32.58	8.77	15.07
6	38.09	9.10	14.02
7	45.15	9.12	13.60
8	52.11	9.30	13.17
9	61.32	11.16	12.60
10	72.83	16.72	12.05
11	82.07	15.87	12.05

Because simulating the particle detector is computationally intensive, it is not possible to incorporate all 192 pixels into a single simulation. Instead, only four elevation levels, namely elevations 0, 4, 8, and 11 on each of the 16 sectors were simulated, resulting in 64 simulated pixels for the entire instrument.

## 4.2 The magnetosheath of Earth

During the first Earth swing-by at the start of the cruise phase in 2024, Juice traversed the Earth's magnetosheath as shown in Figure 39. The magnetosheath forms a turbulent transition region between the bow shock and the magnetopause. In the bow shock region, the solar wind ion flow slows down from supersonic to subsonic velocities as it encounters Earth's magnetosphere. During this process, kinetic energy is converted into thermal energy which leads to considerable heating of the ions in the plasma. At the bow shock, the particle density increases sharply while the magnetic field increases more gradually through the magnetosheath up to the magnetopause.

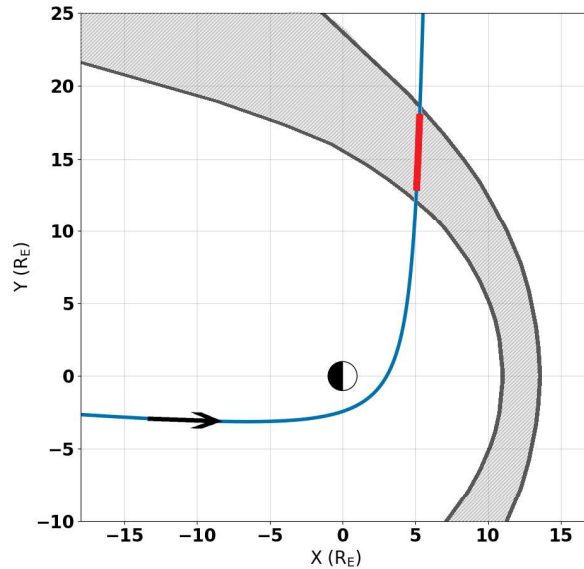


Figure 39 Juice's trajectory during the Earth flyby on August 20 2024, between 00:50 and 03:00 UTC. The trajectory is shown as a blue line, where the period spent in the average extent of the magnetosheath is red coloured. In the left panel, the extent of the magnetosheath is indicated by the grey area. All coordinates are in the GSE coordinate system.

To obtain typical environmental parameters that can be used as input for the magnetosheath charging simulation, results from a magnetohydrodynamic (MHD) simulation from Dimmock & Nykyri (2013) were used. These results are publicly



available on the webpage of the Community Coordinated Modeling Centre (<http://ccmc.gsfc.nasa.gov>). The MHD simulation was set up with typical upstream solar wind conditions that are similar to the ones listed in Table 1. Like in the solar wind, the gyroradii of the particle populations in the magnetosheath are large compared to the dimensions of the Juice spacecraft,  $1.7 \times 10^5$  m and 93 m for ions and electrons respectively, compared to the Juice spacecraft bus of  $2.25 \times 2.50 \times 3.52$  m and solar panels extending 12.07 m along the y-axis of the spacecraft model. Hence, the presence of this magnetic field doesn't affect the spacecraft charging substantially.

For the temperature of the electrons in the magnetosheath, we used data from a statistical study (Wang et al. 2012) containing magnetosheath temperature measurements by three of the THEMIS spacecraft over a duration of four years. Based on the recorded temperatures a value of 30 eV was chosen for the electrons, corresponding to an ion temperature obtained from the MHD simulation of 185 eV. The average values for the plasma parameters in the magnetosheath are given in Table 3.

Table 3. Environmental parameters for the magnetosheath

Parameter	Magnetosheath
$n_e$ [cm <sup>-3</sup> ]	15
$T_e$ [eV]	30
$n_i$ [cm <sup>-3</sup> ]	15
$T_i$ [eV]	185
$V_x$ [km/s]	162
$V_y$ [km/s]	111
$V_z$ [km/s]	11
$ V $ [km/s]	256
$B_x$ [nT]	12
$B_y$ [nT]	-12
$B_z$ [nT]	0.3
$V_{x,s/c}$ [km/s]	0.194
$V_{y,s/c}$ [km/s]	4.337
$V_{z,s/c}$ [km/s]	0.122

### 4.3 The effect of spacecraft charging

To understand how the charging of the spacecraft affects the particle energies, we look at the observed particle energy

$$E_d = E_0 - q\phi_{sc}$$

where  $E_d$  and  $E_0$  are the measured and initial particle energies respectively,  $q$  the charge of the particle, and  $\Phi_{sc}$  is the spacecraft surface potential. According to Liouville's theorem, along an uninterrupted trajectory, that means without collisions, scattering or diffusion, the value of the distribution function in phase space is preserved (Lavraud & Larson 2016). This means that the energy distribution of charged particles upon detection is shifted with respect to their original energy in the unperturbed ambient plasma. Therefore if the distortion of the trajectories resulting from the spacecraft potential is known, Liouville's theorem can be used to obtain the distribution function.

One effect that can't be corrected in this way is the lack of observations of low-energy particles with a charge of the same sign as the spacecraft. Due to the electrostatic repulsion, these particles are not detected by the instrument, which is equivalent to a shift of the distribution function to lower energies. This is problematic for studying low-energy populations. When the spacecraft has a large surface potential, only the most energetic particles are detected. To obtain information about the undetected lower energy part of the spectrum, one would have to assume a certain distribution and fit this to the part of the spectrum that was measured (Lavraud & Larson 2016).

The distortion of the field of view resulting from the charge on the spacecraft is less straightforward to quantify or correct because the change of the particle trajectory depends on its energy, charge, and direction. The rest of this chapter is devoted to characterising the previously discussed perturbations induced in JDC measurements by the charging of the spacecraft in Earth's magnetosheath. In the following sections, the simulation model is introduced, and results from the simulations are shown, followed by a discussion of the obtained results.

## 4.4 Simulating the particle detector

In SPIS, users can assign particle detectors to spacecraft surfaces, which allows us to simulate particle detector measurements and study the distortion of the field of view caused by the charging of the spacecraft. We simulate the particle detector measurements by tracking test particles moving in a frozen electric field from the instrument surface back to the boundary of the simulation volume whilst taking into account the electromagnetic force on the particle throughout the trajectory. The backtracking algorithm in SPIS doesn't consider collisions or other interactions between particles, but that is not a problem for our environments because the magnetosheath plasma is collisionless. In our case, we have  $H^+$  ions as the test particles for the magnetosheath environment.

For the particle tracking, the software employs a Monte Carlo method where each test particle gets initially assigned a random velocity that corresponds to a unit volume in velocity space with dimensions  $[v_x, v_x+dv_x]$ ,  $[v_y, v_y+dv_y]$  and  $[v_z, v_z+dv_z]$ . Since one is usually interested in only a fraction of the entire velocity space (which can be very

large), and it is not known beforehand how coarsely the velocity space should be discretised, SPIS employs an OcTree algorithm. The OcTree algorithm solves this problem by using an adaptive grid that is actively refined in the region of interest. This increases the efficiency of the tracking and improves the quality of the final simulated distribution function that is measured at the instrument.

The OcTree algorithm works as follows: it starts with the entire velocity space and divides it into 8 equally sized elementary volumes, see Figure 40. In the next step, for each of the elementary volumes, several test particles are created with random velocities drawn from that particular velocity space elementary volume via the Monte Carlo method and backtracked from the instrument surface to the simulation volume boundary. At the end of the backtracking when a particle is located on the boundary, its distribution function value is known and since Liouville's theorem states that it should remain constant along its trajectory it directly gives us the distribution function value of the particle trajectory at the instrument surface. This distribution function value indicates how likely it is that a particle follows this specific trajectory. Through this process, each elementary volume in the velocity space is assigned a distribution function value which is the average of the distribution function values of all the backtracked particle trajectories in the elementary volume. Together, the distribution function values of all the elementary volumes yield a velocity distribution that would be measured by the instrument.

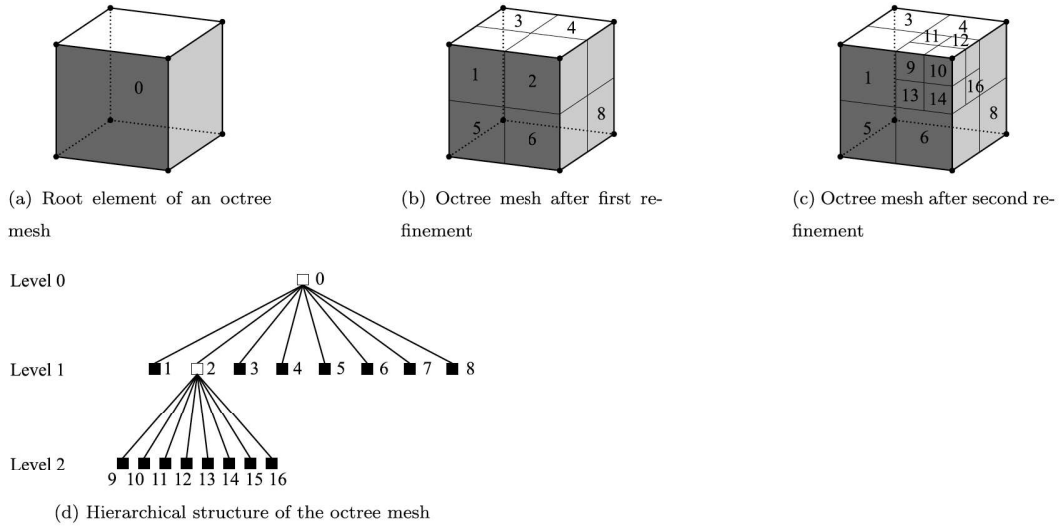


Figure 40 An illustration of the operation of an OcTree algorithm. Shown here are three successive splittings of a volume into smaller elementary volumes (here called meshes). The image was adapted from Zhang et al. (2023).

However, since this distribution function was based on a first subdivision of the velocity space into 8 subvolumes, it is very coarse. Each of the 8 elementary volumes

contains test particle trajectories with a wide range of distribution function values, meaning that the velocity space can be made more detailed. For this reason, after the first splitting, some of the elementary volumes in velocity space are again subdivided if they have a high probability value, or if the test particle trajectories belonging to that elementary volume have broadly varying distribution function values. From this refined grid in velocity space, the Monte Carlo algorithm samples new test particles, and another backtracking is performed which yields new distribution function values for the new elementary volumes. This cycle of refining and backtracking continues until the predefined number of tracking loops is reached, and the final output is returned.

To control the precision of the OcTree algorithm, two parameters can be varied to give the desired result. The first one is “instrument NbOctreeMax” which defines the maximum number of OcTree algorithm refinement cycles. The second adjustable parameter is “instrument NbPartMax”, which is the maximum number of particles that are being backtracked from the instrument surface. The default values for the two parameters are 10,000 and 100,000, but to reduce the noise in the output of our simulations, we increased both values by ten to 100,000 and 1,000,000 respectively.

The output of particle tracking includes among other things the three-dimensional velocity distribution functions at the instrument surface and the simulation volume boundary. From these, the distortion of the instrument's field of view can be determined. Additionally, the tracking also returns the trajectories of test particles with randomly chosen energies, which are very useful for visualising and understanding the actual motion of the ions in the potential field around the spacecraft. Finally, the energy distribution function at the detector and the boundary are also returned, which both can be used to determine how much the particles have been accelerated or repelled by the spacecraft's electrostatic potential.

## **4.5 Setting up a simulation with particle tracking**

The initial steps for setting up a simulation with particle tracking follow the same procedure as a regular simulation, with the exception of certain steps in the ‘Groups’ window and the ‘Instrument list viewer’ window. After importing the simulation mesh, the surface group properties must be imported via the ‘Groups’ window as described in Section 2.7. In this window, surfaces can be selected to act as particle detectors by right-clicking on the group and pressing “Add property from catalog”. In the subsequent dialog, “ActualInstruments.xcat” should be selected, followed by choosing either a “Shared property instance” or a “New property instance” to define a new instrument support. Each instrument support can be assigned an ID number and value, which will later be used when configuring the instrument. Once all relevant instrument surfaces have been assigned an instrument support in the ‘Groups’ window, the setup can proceed through the circuit definition as described in Section 2.8 and global parameter configuration steps, described in Section 2.9.

In the 'Instrument list viewer' menu, instruments can be added by selecting 'Add new instrument' from the left lower corner of the window and, for example, defining a new particle detector. Upon confirmation, a configuration window will appear, where key instrument parameters can be defined, including the coordinate system of the detector, acceptance angles, energy range, and resolution. The `InstrumentSupportId` must correspond to the value assigned to the relevant surface in the 'Groups' window. For instance, if using different sectors as particle detectors, sector 0 may be assigned `InstrumentSupport=1`, sector 1 `InstrumentSupport=2`, and so on. The particle population to be tracked can be specified by entering the name of the desired population type in the `instrumentPop` field (e.g., 'ions1' for simulating ion measurements). As stated above, technical parameters such as "instrument `NbOtreeMax`" and "instrument `NbPartMax`" control the number of backtracking loops and the number of test particles used by the `OcTree` algorithm, respectively. The number of particle trajectories to be visualised and included in the output can be set using the `instrumentTrajNb` parameter. Other useful parameters include:

- `instrumentSamplePeriod`: sets the time interval between measurements of an instrument, usually the same as the simulation duration.
- `instrumentPop`: the name of the particle population that you want to perform backtracking on.
- `instrumentSupportId`: is the id number of the support surface on which the instrument is placed.
- `instrumentEmin`: defines the minimum energy the instrument can detect (for JDC it is 1 eV/q).
- `instrumentEmax`: the maximum energy the instrument can detect (for JDC it is 35 keV/q).
- `instrumentEintervalNbr`: the number of energy levels within the interval between `Emin` and `Emax`.
- `instrumentTrajNb`: the number of plotted particle trajectories in the output

In our simulations, we used an energy range of 0 to 300 eV, with an energy interval number of 300, giving a resolution of 1 eV. The `OcTree` algorithm is used to increase the resolution of the three-dimensional velocity distribution in regions that are of interest and has 2 parameters to adjust the precision of the algorithm:

- `instrument NbOtreeMax`: Defines the maximum number of `OcTree` algorithm refinement cycles.
- `instrument NbPartMax`: Maximum number of particles that are being backtracked from the instrument surface.

For the simulations performed in this report `instrument NbOtreeMax` and `instrument NbPartMax` had values of 100.000 and 1000.0000 respectively, which is 10 times larger than their default value. For more information on how to model particle

detectors and other instruments like Langmuir probes in SPIS, we recommend the SPIS User Manual Annex 2 - Advanced use for scientific applications (Jean-Charles et al. 2013) which explains this in detail.

If instruments from a previous simulation are to be reused, they can be imported using the import instruments button located in the same panel as the 'Add new instrument' option. However, it is often more practical to store the instruments directly within the simulation folder. To do this, copy the instrument files (e.g., `particledetectorX.xml`) to the `Userinstruments` folder that can be found in `Project.spis5/Defaultstudy/Simulations/Run1`. To tell SPIS which instrument files to import and where they are stored, the `'model.xml'` file within the simulation directory must be manually edited. Under `'Userinstruments'`, one has to paste the lines specifying the instrument. These lines are typically generated automatically when an instrument is created via the user interface, but when files are copied manually to the `Userinstruments` folder, the `model.xml` file must be updated manually. An example of these lines for a particle detector modelling the pixel at sector 1 elevation 0 can be seen below. The first particle detector in the `UserInstruments` list must have `instrumentCategoryType="Particle detector id1"`, and the second one `"Particle detector id2"`, and so on. If this is not the case, SPIS may not load the instruments properly at the start of a simulation.

```
<UserInstruments>
<Instrument name="Particle_detector_Sector_1_Elev_0" format="org.spis.instruments.Instrument-0.0.1"
instrumentType="Particle_detector" instrumentCatalogueType="Particle_Detector"
instrumentCategoryType="Particle_detector_id1" creationDate="2023/05/04-11:33:55:277"
lastUpdate="2023/05/04-11:34:39:832" owner="spis" group="spis"
permission="777" isLocal="true">DefaultStudy/Simulations/Run1/UserInstruments/
Particle_detector_Sector_1_Elev_0.xml
</Instrument>
<UserInstruments>
```

When all the instruments have been added to the model file, the simulation is ready to run. Before proceeding, it is advisable to launch the SPIS UI and open the simulation file. The software will open at the running and monitoring step. If the setup has been completed correctly, all particle detectors should appear in the list of instruments. After confirming that the instrument have been properly included, the simulation can be started. As the particle tracking must be executed in batch mode, open the terminal and navigate to the folder containing the SPIS software and enter the following command:

```
./SpisPropulsion.sh -p path-to-my-simulation/mysimulationname.spis5
```

After that the simulation will start, with first the regular charging until the duration time has been reached, and then the tracking starts. Depending on the number of detectors it can take hours for a handful of detectors to multiple days if using 32 detectors.

Things to keep in mind while running particle tracking in SPIS:

1. Don't have a magnetised plasma in the simulation, because the tracking won't be initiated after the simulation ends.
2. Always set the simulation duration longer than 0.1 s, because the particle tracking won't start if the `instrumentSamplePeriod` is smaller than 0.1 s.
3. The particle tracking only works in batch mode, so launching a tracking simulation in the UI will not return any tracking results.
4. If too many particle detectors are included in a simulation, SPIS might run out of memory during the tracking resulting in some detectors not being simulated.

## 4.6 Processing of the simulation output

The output of the SPIS particle tracking contains the 3D velocity distribution functions of the backtracked particles upon detection at the instrument and at the simulation volume boundary. This information can be used to visualise all the original directions of the detected flux at the boundary in a flux map. The method used to process the simulation output is based on the work presented in Bergman et al. (2020a,b).

To do this, the velocity distribution function at the boundary is interpolated on a regular grid of velocity values. The resulting interpolated distribution function  $F(v_r, v_\phi, v_\theta)$  can then be used to integrate the flux on each field of view element in a regular grid of the angular coordinates  $\phi$  and  $\theta$  where it acts as a 'weight' for the probability of the flux direction and energy. This is possible because the velocity components that enter the velocity distribution function have a dependence on the angular coordinates and also the energy via  $v_r = \sqrt{2E/m}$ . To compute the flux with a continuous distribution function, the radial velocity of each test particle is multiplied by the velocity distribution function  $f(v_x, v_y, v_z)$  and integrated over the spherical coordinates, following Bochet et al. 2023.

$$\Phi_{flux} = \iiint \frac{v_r \cdot f(v_r, v_\phi, v_\theta)}{d\Omega} dv_r dv_\phi dv_\theta$$

The quantity inside the integral has to be divided by the solid angle  $d\Omega = \cos(\phi)d\phi d\theta$  giving the computed flux the units of  $m^{-2}s^{-1}sr^{-1}$ . Before plotting, the flux needs to be normalised because it depends heavily on the used simulation settings (Bergman et al. 2020a). This is done by using the highest flux value that was measured on the pixel in the plotted energy interval. Because the velocity distribution function is not continuous but rather an interpolation of the velocity distribution values that were assigned to all the test particles in SPIS, the energies and the field of view are discretised into small elements. The integration of the flux is then performed over each of these elements and combined to form the effective field of view of the pixel. Because of this, the coarseness of the discretisation also determines the final resolution of the flux map. Finally, the result is plotted which is a flux map that shows



for each pixel how much flux originates from each original travelling direction at the boundary. Taking the entire pixel into account, this would be the effective field of view for that pixel, see Figure 41.

When looking at the directions of fluxes received by each individual pixel, it is hard to see the large-scale patterns and distortion of JDC's entire field of view caused by the spacecraft's potential. Instead, it is more convenient to make a distortion map of the whole instrument. A distortion map shows how the centre of the effective field of view of each pixel has shifted compared to the nominal central viewing direction. The distortion on a pixel is defined as the shift in the barycentre (which is something that can be thought of as the 'centre of mass' of the flux) of the field of view of a pixel. Normally this barycentre is located in the centre of the nominal field of view of the pixel as shown in Figure 38, but due to distortion introduced by spacecraft charging, the barycentre may move to different elevations and azimuth angles, as illustrated in Figure 41.

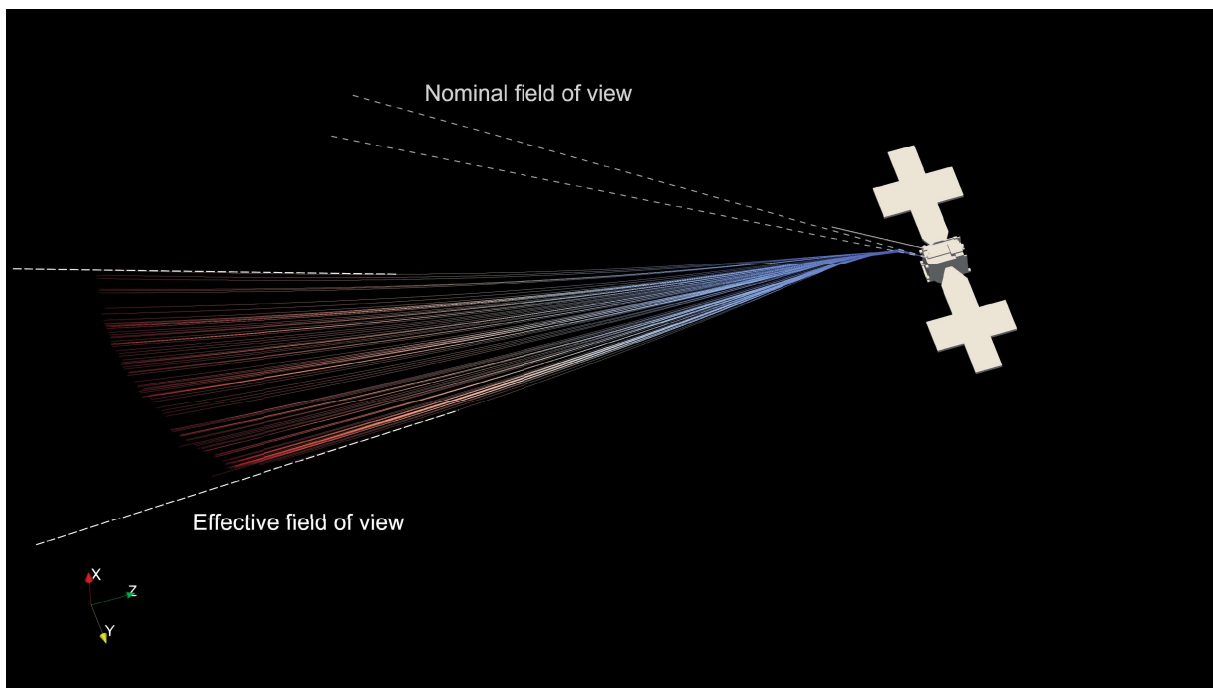


Figure 41 An illustration of the difference between the nominal and effective field of view for a pixel on JDC. In this case, the effective field of view has changed in both size and direction compared to the nominal field of view.

Figure 42 is a drawing that shows the field of view of JDC and the distortion of a pixel's field of view. In the figure,  $r_e$  is the vector that points from the origin (in instrument coordinates) to the barycentre of the effective field of view and  $r_n$  is the vector pointing from the origin towards the nominal centre of the field of view of the

pixel. The distortion vector  $\mathbf{r}_{n,e}$  connects  $\mathbf{r}_n$  with  $\mathbf{r}_e$ . Because a distortion map is two-dimensional, it shows the 2D projection of  $\mathbf{r}_e$  in the plane in which  $\theta$  revolves. The larger the difference between the two, the longer is  $\mathbf{r}_{n,e}$  and the larger the pixel's distortion caused by spacecraft charging.

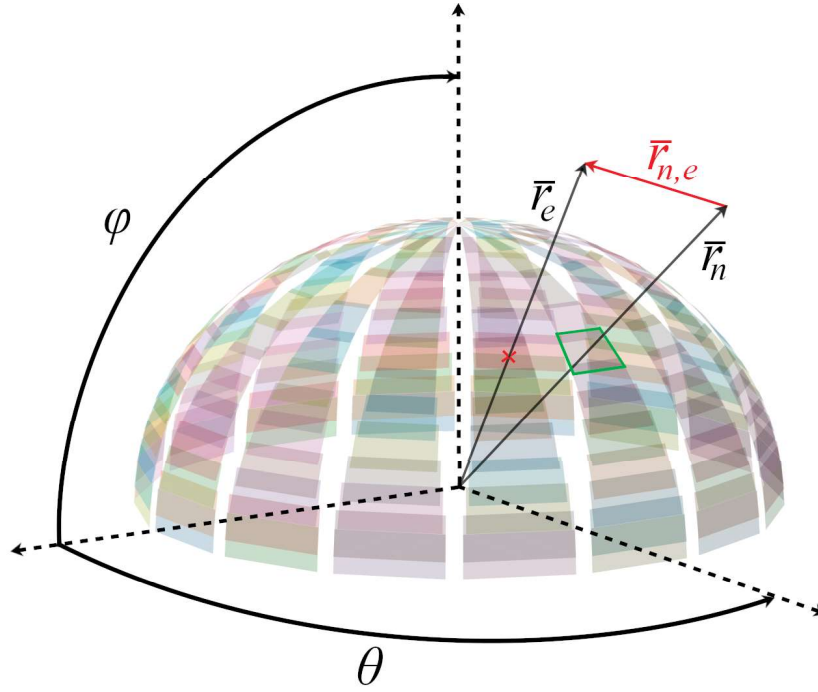


Figure 42 The distortion of a pixel's field of view. The nominal field of view of the pixel is bordered by the green square. The nominal acceptance angle vector  $\mathbf{r}_n$  points to the centre of the nominal field of view and  $\mathbf{r}_e$  is the vector pointing towards the barycentre of the effective field of view that is actually measured. The red arrow connecting the two vectors is the distortion vector  $\mathbf{r}_{n,e}$ . In a distortion map, the distortion vector is projected onto the plane in which  $\theta$  revolves.

To obtain the coordinates of the effective field of view's barycentre, the flux direction on each of the previously mentioned field of view elements is averaged with a weight. In our case, this means that the amount of flux is weighted with the flux direction and averaged using a circular mean. In the instrument coordinate system, the barycentre coordinates are given by

$$\phi_{bary} = atan2\left[\sum_{n=0}^N \sin(\phi_n) \cdot \Phi_{flux}(\phi_n, \theta_n), \sum_{n=0}^N \cos(\phi_n) \cdot \Phi_{flux}(\phi_n, \theta_n)\right]$$

$$\theta_{bary} = \text{atan2} \left[ \sum_{n=0}^N \sin(\theta_n) \cdot \Phi_{flux}(\phi_n, \theta_n), \sum_{n=0}^N \cos(\theta_n) \cdot \Phi_{flux}(\phi_n, \theta_n) \right]$$

where  $\text{atan2}$  is the two-argument arctangent,  $n$  is the discretised field of view element number,  $N$  is the total number of field of view elements,  $\Phi_{flux}(\phi_n, \theta_n)$  is the amount of flux at element  $n$ , and  $\theta_n$  and  $\phi_n$  are the coordinates of element  $n$ . With the coordinates of the barycentre of the effective field of view,  $r_e$  can be calculated and used to find the difference with  $r_n$ . The difference between the two vectors is the distortion vector  $r_{n,e}$ , and can be computed with the following equation

$$\bar{r}_{n,e} = \bar{r}_e - \bar{r}_n = (\phi_{bary,e} - \phi_{bary,n})\hat{\phi} + (\theta_{bary,e} - \theta_{bary,n})\hat{\theta}$$

## 4.7 Simulation results

From the magnetosheath simulation, it was found that the conductive spacecraft surfaces charge up to a potential of 3.7 V, which is less than in the solar wind. This can be explained by the increased electron density and temperature in the magnetosheath compared to the solar wind. The High Gain Antenna is charged up to 6.1 V, and the radiators reach negative potentials below -60 V.

The output of the particle tracking in SPIS can be used to produce flux maps. These maps show the original directions of motion of the detected particles at the simulation volume boundary. An example of a flux map for sector 11 elevation 4 can be seen in Figure 43. The angular size of the pixel corresponding to the nominal field of view is indicated by the green dashed line, and the original particle directions corresponding to the effective field of view are coloured in different shades of red and yellow depending on the amount of flux coming from that direction. The angular coordinate in the flux map is related to azimuth  $\theta$ , while the elevation  $\phi$  is plotted along the radial direction where an angle of  $\phi = 90^\circ$  is at the centre of the flux map and  $\phi = 0^\circ$  is located at the map's edge. Each energy range has two maps, one for the upper hemisphere which is the total nominal field of view of the entire instrument, and the back hemisphere which contains effective viewing directions at negative values of  $\phi$  outside of the nominal field of view.

The flux map in Figure 43 shows that the distortion for energies between 5 and 15 eV is strong, the effective field of view has moved entirely outside the nominal field of view and has also started to spread out over a larger area. The type of distortion seen in this example is caused by the deflection of ions by the spacecraft's main body. Ions come in at high elevation angles, and as they get closer to the positively charged surface they are repelled which bends their trajectory to lower elevation angles. The two other causes of field of view distortion present in the magnetosheath are the attraction from radiator 1 near JDC and deflection by the magnetometer boom. Both

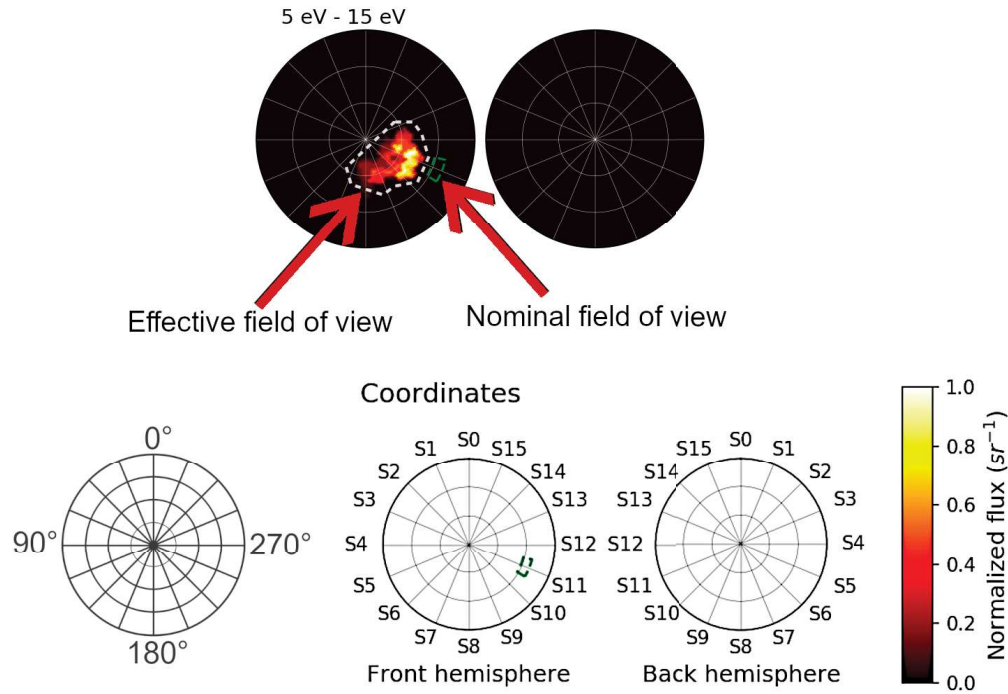


Figure 43 Flux map of sector 11 elevation 4. The pixel size is marked by the dashed green lines, and the area containing the original directions of the detected particles at the boundary is coloured red/orange. Directions of low flux are coloured dark red, with the colour becoming lighter for higher flux until it is white at directions of maximum flux. For each energy range, the flux is normalised with respect to the maximum value of the flux.

of them will be discussed in the sections below. We will regard the distortion as strong when the flux is entirely outside the nominal field of view and is coming from a large range of directions as is the case for the energy range 5-15 eV in Figure 43. Because the particle tracking is computationally intensive, it is not feasible to simulate all twelve elevations in each sector. Instead, we simulate 4 evenly spaced elevations, 0, 4, 8, and 11, on all the 16 sectors of JDC.

#### 4.7.1 Distortion type 1: Main body deflection

The distortion mechanism from Figure 43 is especially important for sectors that are not facing the MAG boom or radiator 1. In all the simulated pixels of sectors 9 to 14, the distortion is caused by the deflection of ions by the spacecraft surface. Also for the lowest elevations of sectors 0 and 1, the distortion is mainly the result of spacecraft deflection.

Main-body deflection is the most prevalent kind of distortion in the magnetosheath, affecting 11 out of the 16 sectors. However, it is not the most severe, as its impact becomes significant only at energies below 40 eV and the shift in flux direction is limited to at most one sector or two elevation levels. Furthermore, the interaction of ions with the main body do not substantially increase flux deflections from different directions since the area of flux is roughly the same across all ion energy ranges. This implies that the trajectories of received particles are altered, but the deflection by the spacecraft bus does not cause particles from a broader range of directions to reach the instrument. The deflection of ions by the main body is the most significant source of distortion for sectors 9 through 13. These sectors face the spacecraft surface and are not significantly influenced by other distorting surfaces like the MAG boom and the radiator, which induce stronger ion interactions. Additional pixels affected by main body deflection are located in sectors 0, 1, and 14.

The pixels on sectors 1, 13, 14, and 15 have almost no distortion for two reasons. First, these sectors face away from both the MAG boom and radiator 1. Second, the JDC instrument is mounted at a 45-degree angle with respect to both the back (-X side) and the nadir (-Z side) of the spacecraft. As a result, particles following trajectories that end in the field of view of the pixels on these sectors do not get close to the spacecraft surface, which is charged at +3.7 V. Consequently, they experience little to almost no deflection by the weakly charged spacecraft body.

#### 4.7.2 Distortion type 2: Radiator attraction

Another type of interaction between Juice and the ions in the magnetosheath that can distort the field of view of JDC is the deflection of ions by radiator 1. This radiator, positioned close to JDC, is charged to a negative potential of -67.8 V. Figure 44 shows numerous simulated trajectories of particles detected by the pixel on sector 4 elevation 0. As seen in the figure, most ions originate from directions of negative elevation ( $\varphi$ ), which are outside of the nominal field of view of this pixel. These ions are only detected by JDC after being deflected by the radiator. The deflection of the ion trajectories can be explained by the strong negative potential on the surface of radiator 1, which attracts nearby positively charged  $H^+$  ions. As a result of this attraction, the travelling directions of the ions are turned towards the radiator which increases their elevation angle.

#### 4.7.3 Distortion type 3: MAG boom repulsion

A third source of perturbations in JDC measurements originates from the repulsion of the  $H^+$  ions by the positively charged (+3.7 V) MAG boom. Due to its position on the spacecraft (see Figure 45), the MAG boom will obstruct and distort the field of view of nearby sectors. An example of how the MAG boom deflects the ion trajectories can be seen in Figure 45, which shows the trajectories for sector 3 elevation 11. It is visible

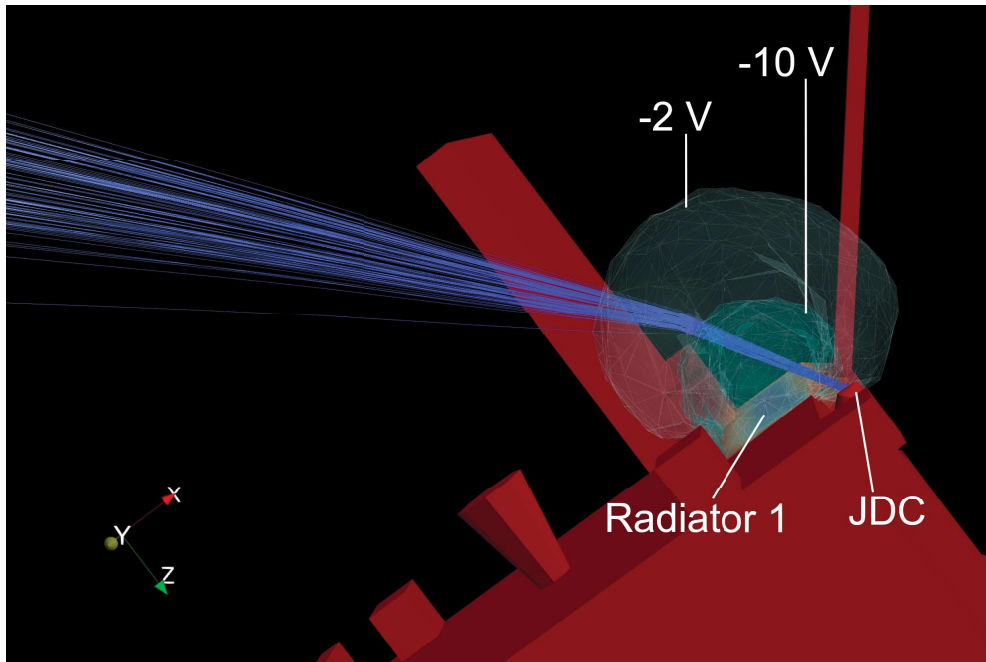


Figure 44 Ion trajectories for sector 4 elevation 0. The outer transparent blue equipotential surface corresponds to a potential of -2 V and the inner equipotential surface to a potential of -10 V. As a consequence of the attraction between the particles and radiator 1, the ion trajectories are deflected towards the radiator, causing particles originating from outside the nominal field of view of JDC to be detected by this pixel.

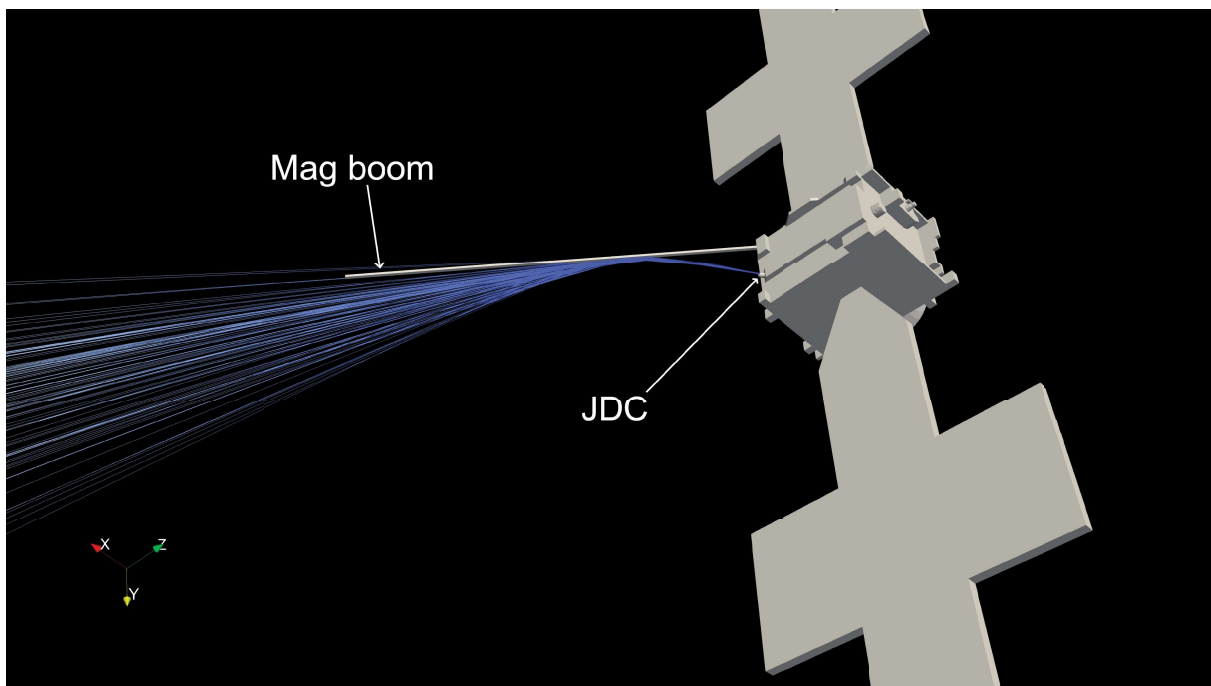


Figure 45 Ion trajectories for sector 3 elevation 11 which visualise the deflection caused by the MAG boom.



that ion trajectories from a large range of angles in azimuth and elevation angles close to the nominal field of view approach the MAG boom and are deflected by the potential towards the nominal viewing direction of the pixel.

Since the MAG boom is charged to +3.7 V, ions approaching it with high elevation angles are deflected in such a way that they are detected in sector 3 elevation 11. It may be more intuitive to consider the reverse: if ions were launched from the instrument in the viewing direction of this pixel, they would approach the MAG boom and be scattered by the positive potential into various directions. The repulsive interaction with the MAG boom distorts measurements at elevation 11 for all sectors from 2 through 7. The pixels at elevations 4 and 8 in sector 2, as well as elevation 8 in sector 3 are also affected. For most of the impacted pixels at the highest elevation level, the distortion becomes significant at energies below 80 eV. In contrast, the distortion is less severe for the affected pixels at a lower elevation angle.

#### 4.7.4 Distortion chart

The dominant distortion types affecting each simulated pixel are summarised in the distortion chart in Figure 46. Radiator attraction and main body repulsion influence the largest number of pixels, and some pixels are strongly distorted by 2 modes

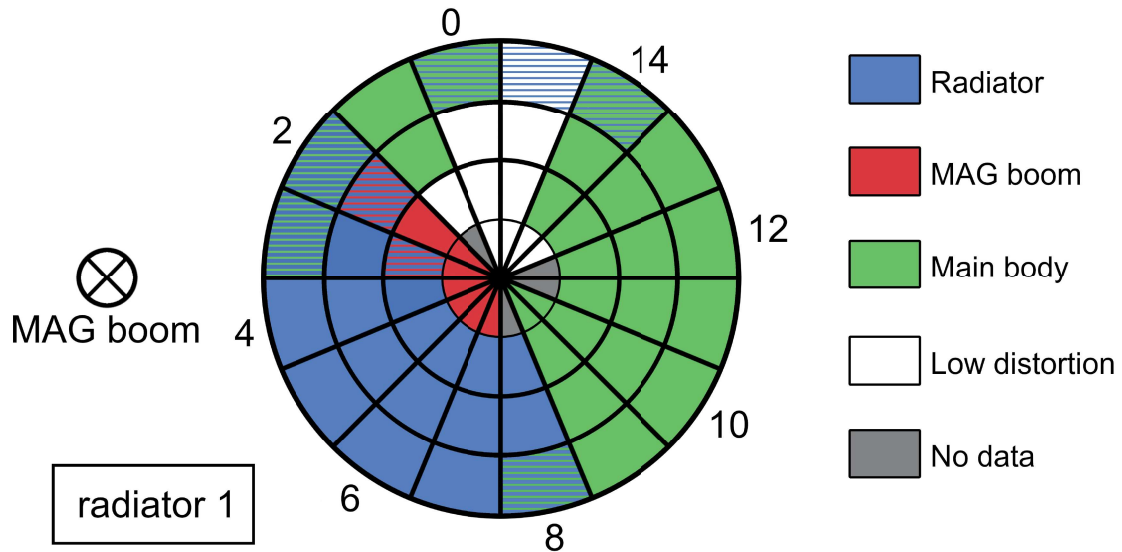


Figure 46 A chart showing the dominant distortion type for the pixels at elevation 0, 4, 8, and 11 in each sector. The approximate locations of the MAG boom and the radiator with respect to JDC are also shown. Radiator attraction is indicated by blue, MAG boom deflection by red, main body deflection by green, and very low distortion by white. The pixels marked in grey have no data because the particle tracking in SPIS could not be performed for those specific pixels.



simultaneously. From the distortion chart and maps, it can be concluded that pixels close to the MAG boom and radiator will have an altered field of view, whereas most of the remaining pixels on JDC are primarily affected by the surface potential of the main body. Distortions are most severe at the lowest and highest elevation levels, which have pixels with viewing directions that pass close by the main body, radiator and the MAG boom. The distortion maps also show that radiator attraction is the strongest distortion mechanism. This is demonstrated by the attraction affecting a large number of pixels in the high-energy range of 80-200 eV, as well as the only clear shift in the field of view of these pixels is towards the location of the radiator.

## 4.8 Discussion

In this chapter, we demonstrate how SPIS can be used to simulate the effects of spacecraft charging on particle measurements. Although the primary focus is on positive ion measurements, the method can be readily adapted to negative ion or electron measurements. The simulations also show how charging of different parts of the spacecraft surface affects both the energy and trajectory of the particles. Simulations like those presented here can therefore serve as a valuable tool for developing correction techniques for particle measurements.

We have shown that the surface potential of Juice will impact the cold plasma measurements of the Juice particle analysers, both by distorting particle trajectories and altering the energy of the surrounding particles. Consequently, cold plasma measurements must be corrected for these changes in energy and trajectory. Detailed SPIS simulations dedicated to each instrument and particle population are required to quantify the needed data corrections. Moreover, when analysing both Langmuir probe and particle analyser data, it is essential to correct for perturbations caused by particle populations originating from the spacecraft itself, i.e., the photoelectrons and secondary electrons. This study also demonstrates that the potential structure around the spacecraft can vary with more than one V for the same radial distance from the spacecraft, which needs to be considered when analysing electric field measurements. Additionally, the formation of an ion wake behind the spacecraft introduces further complexity. Ion depletions are observed at distances exceeding 65 m from the spacecraft. Typically the structure of the wake needs to be taken into consideration when analysing Langmuir probe measurements, so that the decrease in ion density is not mistaken for a plasma depletion in the ambient plasma. SPIS simulations can also be used to explain non-detections, such as the absence of solar wind data by the PEP/JDC instrument, which remains within the ion wake and, therefore, cannot observe solar wind ions unless the spacecraft attitude is adjusted.

These results further highlight that several factors must be considered to minimise the effect of surface charging on particle measurements. These include the design and material selection of both the spacecraft and the instrument, as well as the location of the instrument on the spacecraft. Additionally, simulations such as those presented in

this chapter can be used to identify the optimal location and orientation of a particle analyser on any given spacecraft and environment.

## **Chapter 5. Summary of conclusions**

In this report we present how to use SPIS as a tool to analyse and correct for the effects of spacecraft charging on spacecraft measurements. SPIS has traditionally mainly been used by ESA to assess the risk of electrostatic discharges on their missions. However, this study demonstrates that SPIS can also be used to study the impact of the interaction between the spacecraft and its environment on the spacecraft observations.

Chapter 2 provides an overview of how to use SPIS and Chapter 3 presents the simulation results for the Juice spacecraft in the solar wind at 1 AU. The results show that SPIS can be used to obtain a reliable estimate for the surface potentials of the various spacecraft surfaces. SPIS simulations also give a good understanding of the how the local particle environment is modified by the presence of the spacecraft.

Chapter 4 details how SPIS can be applied to simulate the perturbations in the Juice JDC measurements, which are caused by spacecraft charging. The presented methods are adaptable to any particle analyser, particle population, and environment. This study highlights the capability of SPIS as a powerful tool for studying particle measurement perturbations and developing correction methods. This will help maximise the scientific outcome of planetary missions where particle and field measurements play a crucial role.

## References

- Bagenal, F., Dougherty, L. P., Bodisch, K. M., Richardson, J. D., & Belcher, J. M. (2017), Survey of Voyager plasma science ions at Jupiter: 1. Analysis method, *Journal of Geophysical Research: Space Physics*, 122, 8241- 8256. <https://doi.org/10.1002/2016JA023797>
- Bergman, S., Stenberg Wieser, G., Wieser, M., Johansson, F. L., & Eriksson, A. (2020a). The influence of spacecraft charging on low-energy ion measurements made by RPC-ICA on Rosetta. *Journal of Geophysical Research: Space Physics*, 125(1), e2019JA027478. <https://doi.org/10.1029/2019JA027478>
- Bergman, S., Stenberg Wieser, G., Wieser, M., Johansson, F. L., & Eriksson, A. (2020b). The influence of varying spacecraft potentials and Debye lengths on in situ low-energy ion measurements. *Journal of Geophysical Research: Space Physics*, 125(4), e2020JA027870. <https://doi.org/10.1029/2020JA027870>
- Bochet, M., Bergman, S., Holmberg, M. K. G., Wieser, M., Stenberg Wieser, G., Wittmann, P., et al. (2023). Perturbations of JUICE/JDC ion measurements caused by spacecraft charging in the Jovian magnetosphere and the ionosphere of Ganymede. *Journal of Geophysical Research: Space Physics*, 128(9), e2023JA031377. <https://doi.org/10.1029/2023JA031377>
- Dimmock, A. P. & Nykyri, K. (2013), The statistical mapping of magnetosheath plasma properties based on Themis measurements in the magnetosheath interplanetary medium reference frame: Magnetosheath statistical mapping, *Journal of Geophysical Research: Space Physics* 118(8), 4963–4976. <https://doi.org/10.1002/jgra.50465>
- Futaana, Y., Wang, X.-D., Roussos, E., Krupp, N., Wahlund, J.-E., & Ågren, K., (2018), Corotation plasma environment model: An empirical probability model of the Jovian magnetosphere, *IEEE Transactions on Plasma Science*, 46 (6), 2126-2145. <https://doi.org/10.1109/TPS.2018.2831004>
- Gosling, J. (2014). Chapter 12 – The solar wind. In T. Spohn, D. Breuer, & T. V. Johnson (Eds.), *Encyclopedia of the solar system* (3rd ed., pp. 261–279). Elsevier. <https://doi.org/10.1016/B978-0-12-415845-0.00012-8>
- Grard, R. J. L. (1973). Properties of the satellite photoelectron sheath derived from photoemission laboratory measurements. *Journal of Geophysical Research* (1896–1977), 78(16), 2885–2906. <https://doi.org/10.1029/JA078i016p02885>

Holmberg, M. K. G., Wahlund, J.-E., Morooka, M. W., & Persoon, A. M. (2012). Ion densities and velocities in the inner plasma torus of Saturn. *Planetary and Space Science*, 73(1), 151–160. <https://doi.org/10.1016/j.pss.2012.09.016>

Holmberg, M. K. G., Shebanits, O., Wahlund, J.-E., Morooka, M. W., Vigren, E., André, N., et al. (2017). Density structures, dynamics, and seasonal and solar cycle modulations of Saturn's inner plasma disk. *Journal of Geophysical Research: Space Physics*, 122(12), 12258–12273. <https://doi.org/10.1002/2017JA024311>

Holmberg, M. K. G., Cipriani, F., Nilsson, T., Hess, S., Huybrighs, H. L. F., Hadid, L. Z., et al. (2021). Cassini-plasma interaction simulations revealing the Cassini ion wake characteristics: Implications for in-situ data analyses and ion temperature estimates. *Journal of Geophysical Research: Space Physics*, 126(8), e2020JA029026. <https://doi.org/10.1029/2020JA029026>

Holmberg, M. K. G., Jackman, C. M., Taylor, M. G. G. T., Witasse, O., Wahlund, J.-E., Barabash, S., et al. (2024). Surface charging of the Jupiter Icy Moons Explorer (JUICE) spacecraft in the solar wind at 1 AU. *Journal of Geophysical Research: Space Physics*, 129, e2023JA032137. <https://doi.org/10.1029/2023JA032137>

Johansson, F. L., Eriksson, A. I., Gilet, N., Henri, P., Wattieaux, G., Taylor, M. G. G. T., Taylor, Imhof, C. & Cipriani, F. (2020), A charging model for the Rosetta spacecraft, *Astronomy & Astrophysics*, 642, A43, <https://doi.org/10.1051/0004-6361/202038592>

Lavraud, B. & Larson, D. E. (2016), Correcting moments of in situ particle distribution functions for spacecraft electrostatic charging, *Journal of geophysical research: Space Physics*, 121(9), 8462–8474. <https://doi.org/10.1002/2016JA022591>

Lazar, M., Pierrard, V., Poedts, S., & Fichtner, H. (2020). Characteristics of solar wind suprathermal halo electrons. *Astronomy & Astrophysics*, 642, A130. <https://doi.org/10.1051/0004-6361/202038830>

Michotte de Welle, B., Aunai, N., Nguyen, G., Lavraud, B., Génot, V., Jeandet, A., & Smets, R. (2022). Global three-dimensional draping of magnetic field lines in Earth's magnetosheath from in-situ spacecraft measurements. *Journal of Geophysical Research: Space Physics*, 127(12), e2022JA030996. <https://doi.org/10.1029/2022JA030996>

Maksimovic, M., Zouganelis, I., Chaufray, J.-Y., Issautier, K., Scime, E. E., Littleton, J. E., et al. (2005). Radial evolution of the electron distribution functions in the fast solar wind between 0.3 and 1.5 AU. *Journal of Geophysical Research*, 110(A09104). <https://doi.org/10.1029/2005JA011119>

Pierrard, V., Lazar, M., & Štverák, S. (2020). Solar wind plasma particles organized by the flow speed. *Solar Physics*, 295(11), 151. <https://doi.org/10.1007/s11207-020-01730-z>

Sarrailh, P., Matéo-Vélez, J.-C., Hess, S. L. G., Roussel, J.-F., Thiébault, B., Forest, J., et al. (2015). SPIS 5: New modeling capabilities and methods for scientific missions. *IEEE Transactions on Plasma Science*, 43(9), 2789–2798. <https://doi.org/10.1109/TPS.2015.2445384>

Štverák, Š., Maksimovic, M., Trávníček, P. M., Marsch, E., Fazakerley, A. N., & Scime, E. E. (2009). Radial evolution of nonthermal electron populations in the low-latitude solar wind: Helios, Cluster, and Ulysses observations. *Journal of Geophysical Research*, 114(A5). <https://doi.org/10.1029/2008JA013883>

Venzmer, M. S., & Bothmer, V. (2018). Solar-wind predictions for the Parker Solar Probe orbit – Near-Sun extrapolations derived from an empirical solar-wind model based on Helios and OMNI observations. *Astronomy & Astrophysics*, 611, A36. <https://doi.org/10.1051/0004-6361/201731831>

Wahlund, J.-E., Bergman, J. E. S., Åhlén, L., Puccio, W., Cecconi, B., Kasaba, Y., et al. (2025). The Radio and Plasma Wave Investigation (RPWI) for the Jupiter Icy Moons Explorer (JUICE). *Space Science Reviews*, 221, 1. <https://doi.org/10.1007/s11214-024-01110-0>

Wang, C.-P., Gkioulidou, M., Lyons, L. R. & Angelopoulos, V. (2012), Spatial distributions of the ion to electron temperature ratio in the magnetosheath and plasma sheet, *Journal of Geophysical Research: Space Physics*, 117, A08215. <https://doi.org/10.1029/2012JA017658>

Wang, X., Hsu, H.-W., & Horanyi, M. (2015). Identification of when a Langmuir probe is in the sheath of a spacecraft: The effects of secondary electron emission from the probe. *Journal of Geophysical Research: Space Physics*, 120(4), 2428–2437. <https://doi.org/10.1002/2014JA020624>

Wilson, L. B. III, Stevens, M. L., Kasper, J. C., Klein, K. G., Maruca, B. A., Bale, S. D., et al. (2018). The statistical properties of solar wind temperature parameters near 1 AU. *The Astrophysical Journal – Supplement Series*, 236(2), 41. <https://doi.org/10.3847/1538-4365/aab71c>

van Winden, D. (2024), Juice/JDC ion measurement perturbations caused by spacecraft charging in the solar wind and Earth's magnetosheath, Master thesis, Uppsala University, Available at: <https://uu.diva-portal.org/smash/get/diva2:1836421/FULLTEXT02.pdf>

Wittmann, P. (2022), The Jovian Plasma Dynamics and Composition Analyzer (JDC) for ESA's JUICE Mission, PhD thesis, Umeå University, Department of Physics.



## Appendix

### Appendix A

The spacecraft geometry model used for the guide in Chapter 2.

```
// Simple spacecraft model
// Mika Holmberg
// 2024-07-31

// Lenghts

l = 0.1;      // Characteristic length for mesh generation
b = 2;        // Characteristic length for mesh generation on the boundary

// The spacecraft body

Point(100) = {-1, -1, -1, l};
Point(101) = {-1, -1, 1, l};
Point(102) = {-1, 1, 1, l};
Point(103) = {-1, 1, -1, l};
Point(104) = {1, -1, -1, l};
Point(105) = {1, -1, 1, l};
Point(106) = {1, 1, 1, l};
Point(107) = {1, 1, -1, l};

// The outer boundary

Point(108) = {0, 0, 0, b};
Point(109) = {30, 0, 0, b};
Point(110) = {0, 30, 0, b};
Point(111) = {-30, 0, 0, b};
Point(112) = {0, -30, 0, b};
Point(113) = {0, 0, 30, b};
Point(114) = {0, 0, -30, b};

// Lines for the spacecraft

Line(200) = {100, 101};
Line(201) = {101, 102};
Line(202) = {102, 103};
Line(203) = {103, 100};
Line(204) = {104, 105};
```

```
Line(205) = {105, 106};  
Line(206) = {106, 107};  
Line(207) = {107, 104};  
Line(208) = {105, 101};  
Line(209) = {102, 106};  
Line(210) = {103, 107};  
Line(211) = {104, 100};
```

```
// Lines for the outer boundary
```

```
Circle(212) = {109, 108, 110};  
Circle(213) = {110, 108, 111};  
Circle(214) = {111, 108, 112};  
Circle(215) = {112, 108, 109};  
Circle(216) = {109, 108, 113};  
Circle(217) = {113, 108, 111};  
Circle(218) = {111, 108, 114};  
Circle(219) = {114, 108, 109};  
Circle(220) = {112, 108, 113};  
Circle(221) = {113, 108, 110};  
Circle(222) = {110, 108, 114};  
Circle(223) = {114, 108, 112};
```

```
// Defining the surfaces on the satellite
```

```
Line Loop(300) = {200, 201, 202, 203};  
Plane Surface(301) = {300};  
Line Loop(302) = {204, 205, 206, 207};  
Plane Surface(303) = {302};  
Line Loop(304) = {204, 208, -200, -211};  
Plane Surface(305) = {304};  
Line Loop(306) = {202, 210, -206, -209};  
Plane Surface(307) = {306};  
Line Loop(308) = {205, -209, -201, -208};  
Plane Surface(309) = {308};  
Line Loop(310) = {211, -203, 210, 207};  
Plane Surface(311) = {310};
```

```
// Defining the surfaces of the outer boundary
```

```
Line Loop(312) = {212, -221, -216};  
Surface(313) = {312};  
Line Loop(314) = {213, -217, 221};  
Surface(315) = {314};
```

```
Line Loop(316) = {214, 220, 217};
Surface(317) = {316};
Line Loop(318) = {215, 216, -220};
Surface(319) = {318};
Line Loop(320) = {212, 222, 219};
Surface(321) = {320};
Line Loop(322) = {213, 218, -222};
Surface(323) = {322};
Line Loop(324) = {214, -223, -218};
Surface(325) = {324};
Line Loop(326) = {215, -219, 223};
Surface(327) = {326};
```

```
// Defining the computational volume
```

```
Surface Loop(400) = {301, 303, 305, 307, 309, 311}; // Spacecraft
Surface Loop(401) = {313, 315, 317, 319, 321, 323, 325, 327}; // Outer boundary
Volume(500) = {401, 400};
```

```
// Physical groups
```

```
Physical Surface(600) = {301, 303, 305, 307, 309, 311}; // Spacecraft
Physical Surface(601) = {313, 315, 317, 319, 321, 323, 325, 327}; // Outer boundary

Physical Volume(700) = {500};
```

## Appendix B

The table below lists the Z93C55 material properties and gives a description of the different material properties that have to be listed in the material library of a SPIS simulation.

Value	Name	Unit	Description
0.3	RDC	[-]	Relative dielectric constant
1e-13	BUC	[ohm <sup>-1</sup> .m <sup>-1</sup> ]	Bulk conductivity
5	ATN	[-]	Atomic number
2.2	MSEY	[-]	Maximum secondary electron emission (SEE) yield for electron impact
0.3	PEE	[keV]	Primary electron energy that produces maximum SEE yield
0.5	RPN1	[Angstroms]	Range parameter $r_1$ in the range expression $r_1 (E/E_0)^{n_1} + r_2 (E/E_0)^{n_2}$ , with $E_0 = 1$ keV (or equivalently with no $E_0$ coefficient and $E$ in keV)
50	RPR1	[-]	Range parameter $n_1$
1.55	RPN2	[Angstroms]	Range parameter $r_2$
100	RPR2	[-]	Range parameter $n_2$
0.244	SEY	[-]	Secondary electron yield due to impact of 1 keV protons
230	IPE	[keV]	Incident proton energy that produces maximum secondary electron yield
2e-05	PEY	[A/m <sup>2</sup> at 1 AU]	Photoelectron current for normally incident sunlight
1.3e21	SRE	[ohms]	Surface resistivity
10000	MAP	[V]	Maximum (absolute) potential attainable before a discharge occurs
2000	MPD	[V]	Maximum potential difference between surface and underlying conductor before a discharge occurs
1.4e-13	RCC	[ohm <sup>-1</sup> .m <sup>-1</sup> ]	Radiation induced conductivity coefficient K in the law $K(rate/rate_0)^D$ , with $rate_0 = 1$ rad/s